Study of Diffraction with the ATLAS detector at the LHC

Rafal Staszewski

Thèse de doctorat
de l'Université Paris 11
et
de l'Institut de Physique Nucléaire de l'Académie Polonaise des Sciences

spécialité
Champs, Particules, Matière

présentée par

Rafał STASZEWSKI

pour obtenir les grades de docteur
de l'Université Paris 11
et
de l'Institut de Physique Nucléaire de l'Académie Polonaise des Sciences

Study of Diffraction with the ATLAS detector at the LHC

Thèse soutenu le 24 Septembre 2012 devant le jury composé de:

Etienne AUGÉ (**président**)
Marco BRUSCHI (**rapporteur**)
Janusz CHWASTOWSKI (**directeur de thèse**)
Alan MARTIN (**rapporteur**)
Christophe ROYON (**directeur de thèse**)
Robi PESCHANSKI
Antoni SZCZUREK

Thèse préparée
au Service de Physique des Particules du CEA de Saclay
et
à l'Institut de Physique Nucléaire de l'Académie Polonaise des Sciences de Cracovie

The thesis is devoted to the study of diffractive physics with the ATLAS detector at the LHC. After a short introduction to diffractive physics including soft and hard diffraction, we discuss diffractive exclusive production at the LHC which is particularly interesting for Higgs and jet production. The QCD mechanism described by the Khoze Martin Ryskin and the CHIDe models are elucidated in detail. The uncertainties on these models are still large and a new possible exclusive jet measurement at the LHC will allow to reduce the uncertainty on diffarctive Higgs boson production to a factor 2 to 3. An additional measurement of exclusive pion production $pp \to p\pi^+\pi^- p$ allows to constrain further exclusive model relying on the use of the ALFA stations, which are used in the ATLAS Experiment for detection of protons scattered in elastic and diffractive interactions.

In the last part of the thesis, the AFP detectors, aiming at measuring the protons scattered in diffractive interactions, are presented. They allow to extend substantially the ATLAS physics programme. In particular, the study of the central diffractive W boson production process makes possible a better determination of the nature of diffractive exchanges.

La thèse est consacrée à l'étude de la diffraction en utilisant le détecteur ATLAS auprès du LHC. Après Une courte introduction à la physique diffractive incluant la diffraction 'dure" et "molle", nous presentons la production diffractive exclusive qui est particulierement interessante pour produire des jets et ke boson de Higgs. Le mécanisme décrit par le formalisme de Khoze Martin et Ryskin et celui de CHIDe sont décrits en détail. Les sources d'incertitudes dans la description théorique sont encore importantes et une nouvelle mesure de la section efficace de production exclusive de jets au LHC permettra de reduire l'incertitude de la production diffractive de boson de Higgs à un facteur 2 à trois. La mesure de la production exclusive de pions $pp \to p\pi^+\pi^- p$ permet de contraindre les modèles de manière plus précise en utilisant les detecteurs ALFA, qui sont utilisés dans l'expérience ATLAS pour la détection de protons diffusés dans les interactions élastiques et diffractives.

Les détecteurs AFP décrits dans la dernière partie de la thèse, mesurant les protons dispersés après interaction diffractive sont présentés. Ils permettent d'étendre le programme de physique d'ATLAS, avec en particulier, la production centrale diffractive de boson W, ce qui rend possible une meilleure comprehension de la nature des échanges diffractifs.

The Henryk Niewodniczański
Institute of Nuclear Physics
Polish Academy of Sciences

University of Paris-Sud 11

Study of Diffraction with the ATLAS Detector at the LHC

Rafał Staszewski

Supervisors:
dr hab. Janusz Chwastowski, prof. IFJ
dr hab. Christophe Royon, directeur de recherche

Contents

Introduction

DIFFRACTION has always been an important part of the studies performed in experiments involving hadron interactions. This is true also for the LHC, where a large community works on both theoretical and experimental aspects of possible diffractive measurements. At the LHC, contrary to previous studies at HERA and Tevatron, diffraction have a chance to contribute into studies of *new physics*, both in the Higgs and Beyond Standard Model (BSM) sector.

This work presents the author's contribution into the development of the diffractive programme in the ATLAS experiment at the LHC. The obtained results are important both for the general, motivational aspects concerning the possible measurement and their significance, as well as for more technical details crucial for the experimental set-up, its performance and data quality.

Chapter 1 of the thesis contains an introduction into the field of diffractive physics. It begins with presenting soft diffraction, contributing to minimum bias interactions, present in pile-up events and thus important to all measurements performed at the LHC at high luminosity. Next, hard diffraction and its types are discussed, which are most interesting from the Quantum Chromodynamics (QCD) point of view and the mechanism governing the Pomeron exchange. Finally, exclusive production is introduced and its different types are discussed.

Chapter 2 discusses the models of exclusive production of jets and the Higgs boson and their theoretical uncertainties. Different sources of uncertainty are presented and their impact on the uncertainty of the cross sections is studied. An attempt is made to estimate the overall uncertainty of exclusive processes at the LHC based on measurements from the Tevatron. Finally, the possibility of constraining the uncertainty on Higgs production with early jet measurements is investigated.

Chapter 3 briefly introduces the Large Hadron Collider, presenting the main points of its programme, the key aspects of its design and properties and the LHC

experiments. Next, a more detailed description of the ATLAS experiment is given, including sub-detectors, trigger and data processing.

The present ATLAS detector allows investigation of diffraction by direct tagging of the forward protons in a very limited way. This can by done with the ALFA detectors, whose primary purpose is to measure elastic scattering, but they allow also studies of single diffractive dissociation processes. Chapter 4 shows that one more process can be measured with ALFA detectors, *i.e.* the exclusive $\pi^+\pi^-$ production.

In order to enhance the ATLAS abilities beyond the ones provided by ALFA, additional dedicated detectors are needed. Chapter 5 presents the project of ATLAS Forward Proton (AFP) detectors that would allow detection of the diffractively scattered protons. First, the most interesting measurements possible with the AFP detectors are presented, second the detector design is discussed. Then, the properties of the detectors due to the LHC magnetic lattice are shown, in particular the geometrical acceptance of the detectors and the resolutions of the energy reconstruction.

In the last chapter, the possibility of the central diffractive W production measurement is studied. In particular, the measurement of W charge asymmetry and its role in determining the diffraction mechanism are discussed. The analysis is based on full simulation of the ATLAS detector, including pile-up interactions, and contains the detailed study of signal and backgrounds.

The presented results are based on the work performed during the four years of PhD studies. The majority of them have been published or presented during conferences and workshops.

Personal Contributions

Published Articles

- M. Trzebiski, R. Staszewski i J. Chwastowski, *LHC High-β^* Runs: Transport and Unfolding Methods*, ISRN High Energy Physics, vol. 2012, Article ID 491460.
- R. Staszewski, M. Trzebiski i J. Chwastowski, *Dynamic Alignment of the Forward-Proton Detectors at the LHC*, Advances in High Energy Physics, vol. 2012, Article ID 428305.
- K. Golec-Biernat, C. Royon, L. Schoeffel, R. Staszewski, *Electroweak vector boson production at the LHC as a probe of mechanisms of diffraction.* Published in Phys. Rev. D84 (2011) 114006.
- R. Staszewski, P. Lebiedowicz, M. Trzebiński, J. Chwastowski, A. Szczurek, *Exclusive $\pi^+\pi^-$ Production at the LHC with Forward Proton Tagging.* Published in Acta Phys. Polon. B42 (2011) 1861-1870.

- The ATLAS Collaboration (R. Staszewski for the Collaboration), *The AFP Project.* Published in Acta Phys. Polon. B42 (2011) 1615-1624, presented at Cracow Epiphany Conference 2011 *The First Year of the LHC.*
- A. Dechambre, O. Kepka, C. Royon, R. Staszewski, *Uncertainties on exclusive diffractive Higgs and jets production at the LHC.* Published in Phys. Rev. D83 (2011) 054013.
- R. Staszewski, J. Chwastowski, *Transport Simulation and Diffractive Event Reconstruction at the LHC.* Published in Nucl. Instrum. Meth. A609 (2009) 136-141.

Preprints and Notes

- M. Boonekamp, A. Dechambre, V. Juranek, O. Kepka, M. Rangel, C. Royon, R. Staszewski, *FPMC: A Generator for forward physics.* arXiv:1102.2531 [hep-ph].
- R. Staszewski, J. Chwastowski, *Analysis of Proton Transport for Diffractive Physics with ATLAS.* ATL-LUM-INT-2009-003 (reviewed internal ATLAS note).
- O. Kepka, C. Royon, L. Schoeffel, R. Staszewski, M. Trzebiński, R. Žlebčik, *Physics Cases within the AFP project.* ATL-COM-PHYS-2012-775 (ATLAS internal note, under review).

Chapter 1

Diffractive Physics

The majority of interactions involving hadrons is ruled by strong interactions. In Quantum Chromodynamics, the theory of strong interactions, they are described by a colour field and their quanta – gluons. Unlike the electromagnetic field, where the photons do not carry the electric charge, gluons have colour charges. This has a lot of consequences. One is the existence of interactions between gluons as three- and four-gluon vertices. Another one is that strong hadron interactions are usually accompanied by colour charge exchange between the interacting particles.

Strong interactions are endowed with a very interesting feature called *confinement*, which also does not exist for electromagnetic interactions. It causes that all physically observable particles carry no net colour charge. This is because the strength of interaction between two colour charges grows with increasing distance between them. This is usually illustrated by a simple picture of two colour charges (*e.g.* $q\bar{q}$ pair) being separated. The energy of the colour field increases, similarly to a situation of a stretched spring. At some point the energy is greater then the rest mass of the $q\bar{q}$ pair. This allows another such a pair to be created, causing partial local neutralisation of the existing colour charges, see Figure 1.1. In other words, the colour exchange leads to radiation (creation of additional particles) between the interacting particles. Such a process usually leads to destruction of the interacting particles.

Processes in which no quantum numbers are exchanged between the interacting particles are called diffractive ones. In QCD this can be obtained by an exchange of two gluons in the overall colour singlet state. However, this simple description is not applicable for all cases. Instead, one often speaks about the exchange of a Pomeron. The Pomeron is an object defined within the Regge theory [1]. It is responsible for the growth of the total cross section with energy and its exchange leads to soft

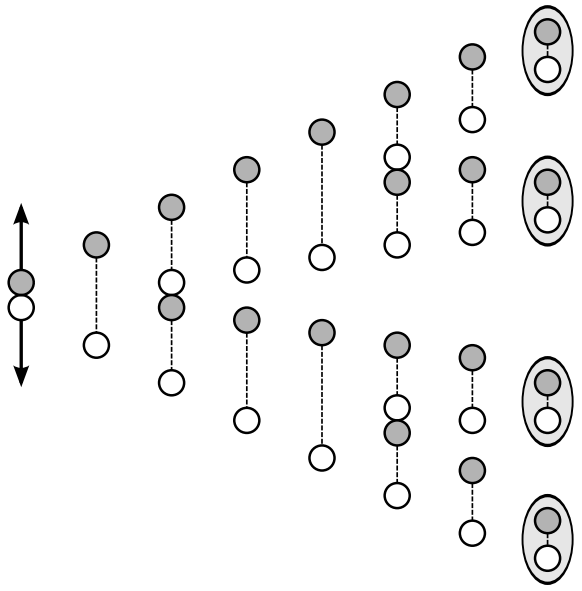

Figure 1.1: Illustration of the hadronisation process. Two quarks with opposite colour charges (white and grey circles) receive some kinetic energy (black arrows). While their distance increases the energy of the colour field (dashed line) increases until a new $q\bar{q}$ pair can be created. The process continues until quarks and anti-quarks combine into clueless particles. Only the production of mesons is shown, but in reality baryons are also produced.

diffractive interactions, see Section 1.1. In addition, colour singlet exchange can lead also to hard interactions, see Section 1.2. This description is often called the t-channel approach, since the Pomeron is exchanged in the t-channel.

An alternative description of diffractive interactions is offered in the s-channel Good-Walker approach [2]. Here, one treats the proton as a superposition of quantum states that diagonalise the transition matrix of diffractive interactions (which is assumed to be dominated by its imaginary part). The diffractive interaction is then understood as an absorption of these states and the absorption factors can be different for different states. In QCD the Good-Walker states can be described in terms of $q\bar{q}$ dipoles of different radii.

Diffractive interactions can be experimentally recognised by two features:

large rapidity gaps – there is no colour exchange in the diffractive interactions, therefore radiation between the interacting particles is suppressed,

intact protons – when only vacuum quantum numbers are exchanged it is possible that the interacting hadron (proton, at the LHC) is not destroyed, but remains intact.

Unfortunately, none of the above allows recognition of diffractive interactions on the event-by-event basis. First, large rapidity gaps can occur also in non-diffractive interactions as statistical fluctuations of the distance between neighbouring particles.

Second, the detectors used in collider experiments can never cover the full solid angle around the interaction point. In particular, the uncovered region is the accelerator beam pipe, where the interacting particles come from. Unfortunately, this is the region where the diffractively scattered, intact protons usually go into. As will be described later on, it is possible to install dedicated detectors that would be able to register such protons. However, any other particles scattered into the beam pipe would not be detected by them. Therefore, one cannot be sure whether an observed proton is really intact, *i.e.* not accompanied by additional particles.

In addition, one cannot be sure that an observed event is a non-difractive one. Rapidity gap sizes depend on the kinematics. When protons lose a large part of their energy, the gaps are quite small and can be completely confined to the beam pipe region not covered by detectors. Also, the lack of forward protons is not really significant – the dedicated detectors have limited acceptance. Moreover, it is possible that in a diffractive interaction the proton dissociates into a higher mass state. The proton dissociation was studied by the HERA experiments and was found to be present in about 25% of the soft diffractive events [3]. On the other hand, requesting a large rapidity gap or a detection of a proton scattered into the beam pipe makes it very likely that such an event is really of diffractive nature.

This chapter aims at introducing the reader to the most important topics in the diffractive physics. First, the soft diffraction is presented and its kinematics is introduced. Later, hard diffraction and its description in terms of Pomeron with a parton structure are discussed. Finally, exclusive production is introduced and its different mechanisms are presented.

1.1 Soft Diffraction

The QCD theory heavily uses the methods of perturbative expansion to obtain quantitative results. Such methods are justified only when the expansion parameter, in QCD the strong coupling constant α_S, is small enough to ensure that neglecting higher terms of the expansion makes sense.

The coupling value is actually not constant, but depends on the distance between the interacting particles (impact parameter of the interaction). This effect is called the *running coupling constant* [4]. In QCD the coupling increases with increasing distance. At large distances the coupling is large, which leads to the confinement effect and is the reason why strong interactions are called *strong*. Only when the distance is very small, the coupling is small enough so that perturbative calculations are possible. Such a case is called a *hard* interaction. Otherwise, the interaction is non-perturbative and is called *soft*.

The impact parameter of the interaction is very closely related to the momentum exchanged – the smaller the distance, the greater the exchanged momentum. Actually, it would be impossible to measure the distance directly, since it is way

too small. In hadron collisions it is impossible also due to another reason – the interactions can occur not only between the whole particles, but also between their constituents. Therefore, instead of the interaction distance, the exchanged momentum is commonly used and called the *scale* of the interaction. It can be measured experimentally, by looking at the properties of objects produced in the collision (their invariant mass or transverse momentum). The interaction is considered hard if such a scale of value greater than about 1 GeV can be found.

A great majority of hadron collisions is soft. In fact, only a very tiny fraction of events is hard, and this fraction decreases with increasing momentum scale. Therefore, when considering the total cross section for hadron interactions only soft processes have a significant contribution.

There are five types of soft processes: elastic scattering, non-diffractive interactions, single diffractive dissociation, double diffractive dissociation and central diffraction. Figure 1.2 presents their classification.

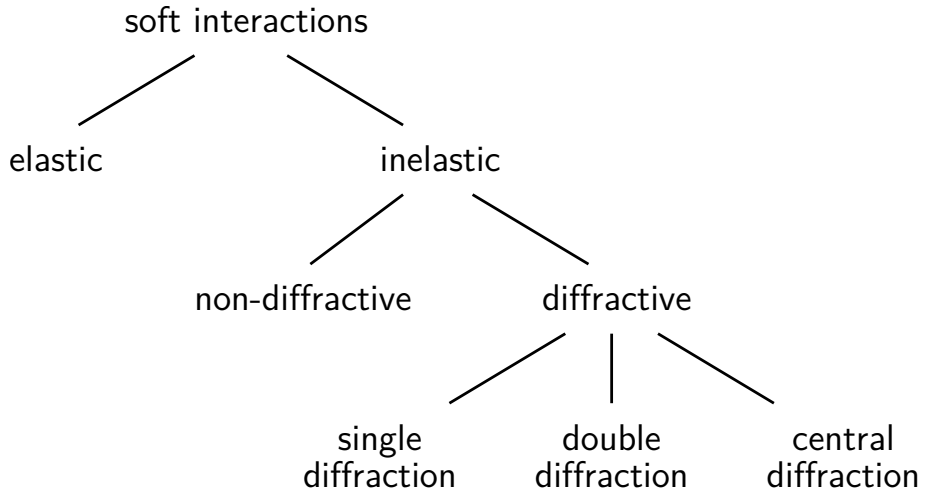

Figure 1.2: Diagram illustrating the classification of soft processes in hadron collisions.

Elastic scattering

Elastic scattering is the simplest process of particle interactions where the final state particles are the same as in the initial state:

$$a + b \to a + b.$$

The diagram representing this process is shown in Figure 1.3 (left). The kinematics of this process is very simple and for unpolarised case described by two variables. In the target reference frame these are the initial energy of the projectile and the scattering angle. However, usually the Mandelstam s and t variables are used, due

to their Lorentz invariance. They are defined as:

$$s = (P_1 + P_2)^2, \qquad t = (P_1 - P_1')^2 = (P_2 - P_2')^2,$$

where P_1 and P_2 are the four-momenta of the initial state particles, while P_1' and P_2' describe the final state particles.

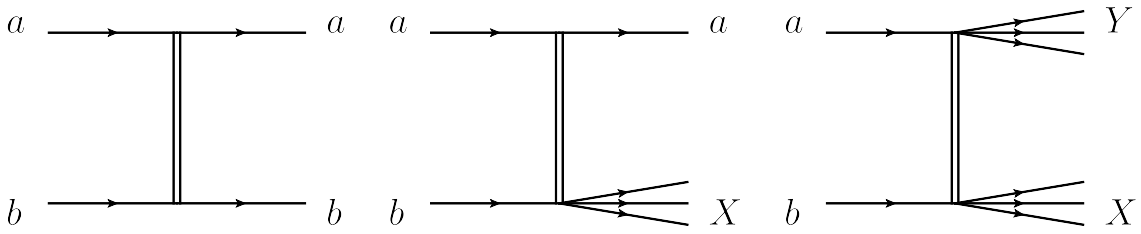

Figure 1.3: Diagrams of soft diffractive scattering processes: elastic scattering (left), single diffraction (centre) and double diffraction (right). The double line represents the Pomeron exchange (for elastic scattering also the photon exchange).

A closer look at this process explains the origin of the name *diffraction* used in particle physics in analogy to optics. Figure 1.4 presents the t distribution of elastic scattering measured at the LHC by the TOTEM experiment [5], where the diffractive structure of maxima and minima can be seen.

Even though elastic scattering is the simplest process one can imagine, it is very difficult to describe and to predict its characteristics, due to its non-perturbative properties. Moreover, strong interactions are not the only ones that contribute to this process, electromagnetic exchanges need also to be taken into account. This is especially true at small values of t, where they dominate over strong interactions.

Single Diffractive Dissociation

Single diffractive dissociation (SDD, or single diffraction – SD) is the following process:

$$a + b \to a + X,$$

where a and b denote hadrons, whereas X is a multi-particle state of the same quantum numbers as particle b. One can say that b dissociates into X. A schematic diagram of the process can be found in Figure 1.3 (centre). In order to describe this process, and also other processes in which at least one of the particles stays intact, the reduced energy loss ξ is introduced and defined as:

$$\xi = \frac{\Delta E}{E_0} = \frac{E_0 - E}{E_0},$$

where E_0 and E are respectively the initial and the final energies of the particle a, while ΔE is its energy loss in the process.

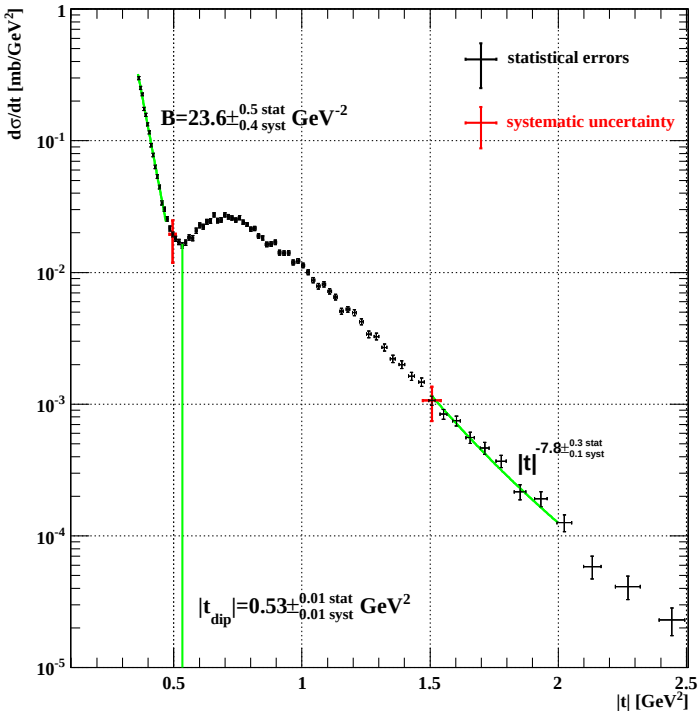

Figure 1.4: Differential cross section as a function of four-momentum transfer, t, for elastic scattering at $\sqrt{s} = 7$ TeV, as measured by the TOTEM experiment [5]

Double Diffractive Dissociation

Double diffractive dissociation (DDD, or double diffraction – DD) is similar to single diffraction, but here both particles dissociate:

$$a + b \to Y + X,$$

where a and b are the initial state particles, while Y and X are multi-particle states of the same quantum numbers as particles a and b, respectively. Figure 1.3 (right) shows a schematic diagram.

Central Diffraction

Central diffraction, also called *double Pomeron exchange (DPE)* is a process, where both incoming particles radiate a Pomeron and, in addition, a central state is produced. The simplest case has the following structure:

$$a + b \to a + Z + b,$$

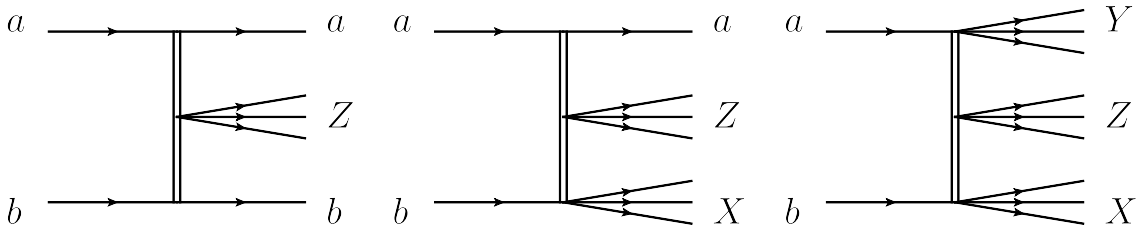

Figure 1.5: Feynman diagrams of central diffraction processes. Different possibilities of proton states are presented: left – both protons stay intact, centre – one proton stays intact and the other one gets dissociated, right – both protons dissociate.

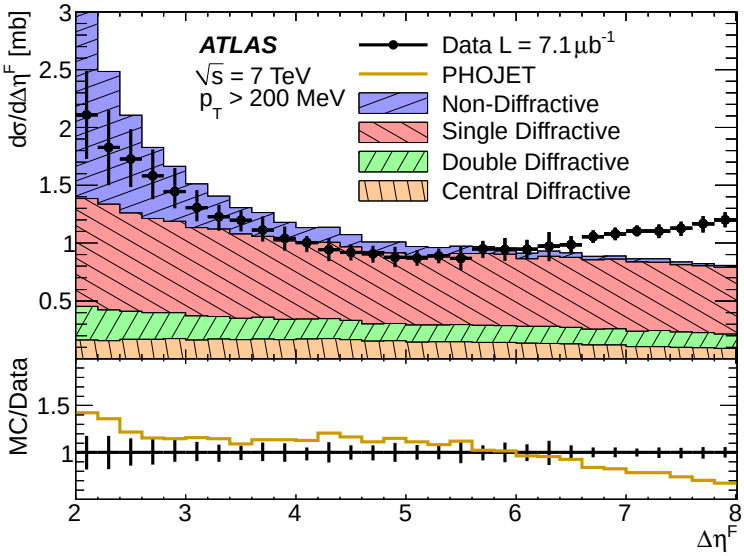

Figure 1.6: Minimum bias cross section differential in the forward (measured from the edge of the calorimeter $\eta = \pm 4.9$) rapidity gap size $\Delta\eta^F$ as measured by the ATLAS Experiment at $\sqrt{s} = 7$ TeV. Predictions of the Phojet generator for the non-diffractive, single diffractive, double diffractive and central diffractive contributions are compared to the data. [6]

where a and b are the particles and Z is some state (one or more particles) with quantum numbers of the vacuum. It is also possible that one or both of the incoming particles dissociates into a higher mass state, like in the case of single and double diffraction. This is illustrated in Figure 1.5. It should be mentioned that central diffractive events where the central mass is high, leading to small rapidity gaps, and both protons dissociate is experimentally indistinguishable from a non-diffractive process.

All processes, excluding elastic scattering, contribute to *inelastic* interactions. They are very important from the experimental point of view, since they are the majority of the processes that are usually detected by the central detectors. They are often called the *minimum bias* interactions. Out of these interactions, the interesting processes have to be filtered out.

The minimum bias events are especially important at the LHC for one more reason. Due to very large luminosity of the machine, many interactions may happen within a single bunch crossing (*pile-up*). Even if one of them is of hard nature, the rest belongs to minimum bias collisions. Naturally, the detectors register the particles produced in all interactions, and the soft processes influence the measurement of the hard ones.

Figure 1.6 presents the distribution of the rapidity gap size for the minimum bias events as measured by the ATLAS Collaboration [6]. This study was performed with the data collected during the second year of the LHC running, when the luminosity was relatively small and hence the pile-up was negligible. In addition, the Phojet generator predictions are shown. One can see not only the contributions from the diffractive processes, but also those of the non-diffractive ones. For the latter case, the distribution extends up to 7 units of pseudorapidity. In non-diffractive events, such large rapidity gap sizes may be due to random fluctuations or the limited detector sensitivity to low energy particles.

1.2 Hard Diffraction

Hard processes are the main reason for building large particle physics accelerators, like the LHC. This can be understood in two equivalent ways. By going to higher energy scales of collisions, smaller distances can be reached and the properties of matter probed there. The accelerator can be treated as a complicated microscope. Higher resolution is obtained with smaller wave length, *i.e.*, according to the de Broglie principle, with higher energy of the particles. In an alternative approach, only very high momentum transfers enable creation of new, unobserved yet, particles or observation of some deviations from the Standard Model predictions as a manifestation of *new physics*.

Hard interactions are interpreted as the scattering of the hadron constituents – partons (*i.e.* quarks and gluons). The distribution of partons within the proton [7, 8, 9] is known from various experiments, which measure observables that are sensitive to the proton structure. Important contribution comes from the DIS (*deep inelastic scattering* – scattering of leptons off nucleons) experiments. However, one should note that data coming from the Tevatron and the LHC are also used in the PDFs determination.

The cross section for a hard process can be calculated as a convolution of these distributions with the cross section for parton-parton interaction:

$$\mathrm{d}\sigma = f_p(x_1, \mu^2) \cdot f_p(x_2, \mu^2) \cdot \mathrm{d}\sigma_{\mathrm{hard}}(x_1, x_2, \mu^2), \tag{1.1}$$

where x_1 and x_2 are the proton momentum fractions carried by the interacting partons, μ is the scale of the process and $f_p(x, \mu^2)$ is the parton distribution function.

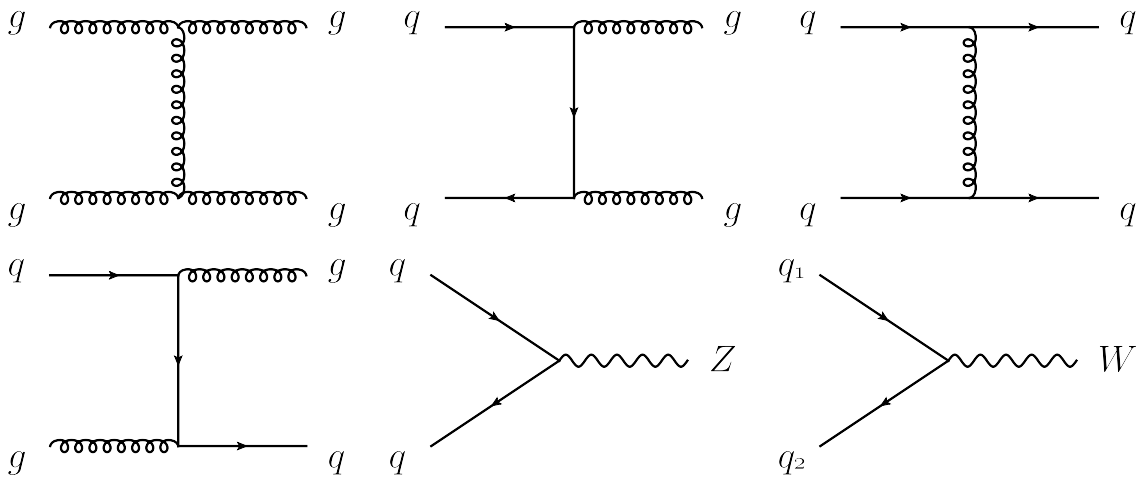

Figure 1.7: Feynman diagrams of hard parton-parton interactions. First four diagrams lead to jets production, the 5^{th} one shows the Z, while the 6^{th} one the W boson production. In the last diagram, the flavour of the quark is different from the flavour of the anti-quark.

The parton distributions are universal, which means that they are the same for all processes. However, so far it is not possible to calculate them from first principles, mainly because the perturbative methods are not applicable here and the non-perturbative ones are not yet advanced enough. However, the QCD equations predict accurately how the PDFs values change with the scale. Therefore, the PDFs are measured and parametrised at a given scale, then the QCD evolution can be performed to calculate their values at the scale appropriate for the process of interest.

On the other hand, the hard parton-parton interactions can be calculated perturbatively. A few examples of such interactions are presented in Figure 1.7. The first four diagrams show different processes contributing to the jet production[1]. The last two diagrams show the processes of Z or W electroweak bosons production as an annihilation of two quarks (a quark and an anti-quark). The Z boson originates (mainly) from two quarks of the same flavour, whereas for the W boson the flavours must be different due to the electric charge conservation.

Figure 1.8 shows the Feynman diagrams of jet (left) and W/Z (right) production. The thick solid lines denote the incoming protons, the blobs, their partonic structure. One parton from each proton takes part in the hard interaction, while the rest forms the proton remnant. The jet diagram does not include the hadronisation of the gluons emerging from the hard interaction into jets.

Hard interactions can also involve the exchange of vacuum quantum numbers, they are then called *hard diffraction*. Such interactions were proposed for the first time in [10], where the authors suggested the existence $p+\bar{p} \to p+X$ process, where

[1] A single parton cannot be observed due to confinement, instead a jet, *i.e.* a stream of particles originating from the initial parton, is produced.

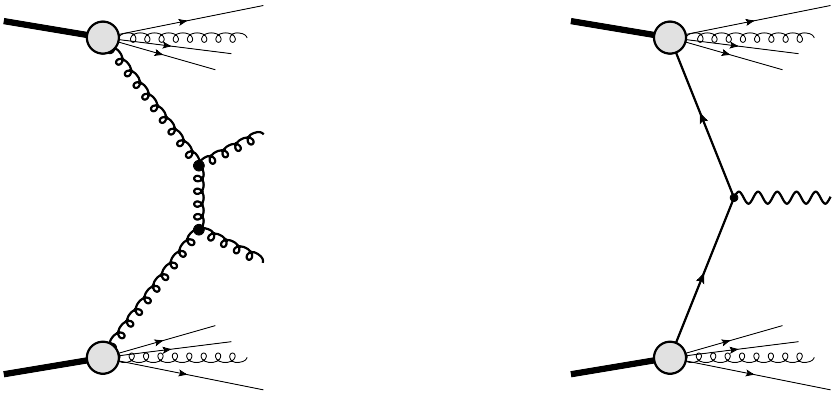

Figure 1.8: Feynman diagrams of non-diffractive production of jets (left) and W/Z boson (right).

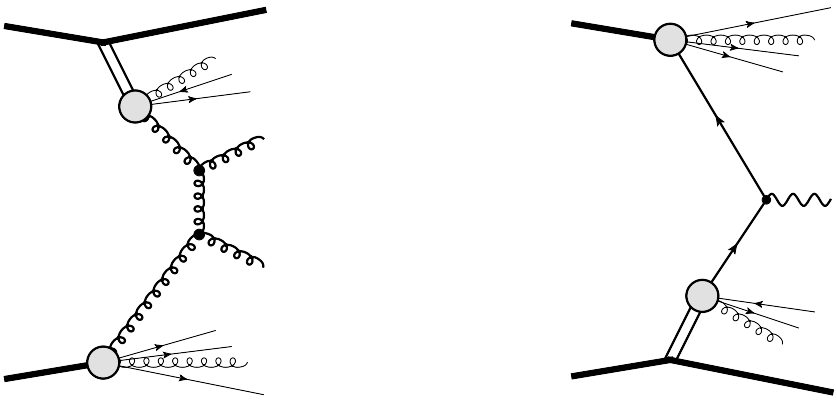

Figure 1.9: Feynman diagrams of single diffractive production of jets (left) and W/Z boson (right).

X system contains two high-p_T jets. This process was experimentally observed [11] and measured [12] by the UA8 experiment at the S$p\bar{p}$S collider. Such events can be described assuming that in a hard diffractive interaction a Pomeron is exchanged and that it reveals its partonic structure. This is depicted in Figure 1.9, where the diagrams of diffractive jets (left) and W/Z (right) production are presented. The double solid line represents the Pomeron exchange and the blobs denote the partonic structure of the Pomeron and that of the proton. In the final state one can notice: the jets or the heavy boson (W or Z), the Pomeron remnants, the proton remnants and the second proton leaving the interaction intact. These processes are described in terms of the proton *diffractive parton distribution functions* (DPDFs).

The DPDFs are similar to the PDFs and they have also been obtained from DIS experiments [13, 14]. However, they contain a dependence on additional variables describing the proton kinematics. In non-diffractive collisions the proton remnants are not detected and the measured cross sections are integrated over all possible states. Thus, the extracted PDFs do not have any dependence on the remnants kinematics. In the diffractive case, the proton is detected[2], therefore the additional dependencies on relative energy loss[3] and four-momentum transfer can be introduced:

$$f(x, \mu^2, \xi, t), \tag{1.2}$$

where f denotes either the quark or the gluon distributions. It turns out that the dependence on proton kinematics factorises out from the hard interaction variables [3]:

$$f(x, \mu^2, \xi) = \Phi_{\mathbb{P}}(\xi, t) \cdot f_{\mathbb{P}}(\beta, \mu^2), \tag{1.3}$$

where $\beta = x/\xi$. This allows the interpretation given at the beginning of this section – it is the parton from the Pomeron that is involved in the interaction and β is the fraction of the Pomeron momentum carried by the interacting parton. Then, $\Phi_{\mathbb{P}}(\xi, t)$ can be understood as a Pomeron flux and $f_{\mathbb{P}}(x, \mu^2)$ describes the partonic structure of the Pomeron. Figure 1.10 presents examples of quark and gluon DPDFs for $\mu = 25$ GeV^2 and $\mu = 90$ GeV^2 as a function of z, the fractional momentum of the Pomeron carried by the parton (in the lowest order $z = \beta$). One can see that for z values close to 1, both quark and gluon densities decrease to zero. Also, for z values smaller than about 0.5 the gluon contribution is greater than the quark one. Therefore, the Pomeron nature is predominantly gluonic and in most of the cases the majority of the Pomeron energy does not contribute to the produced hard state, but is carried by the Pomeron remnants.

[2]The structure functions were also obtained from the measurements based on large rapidity gap observation. This is complementary to the method based on tagging the proton, since it takes into account also the interactions that contain proton dissociation. On the other hand, only the ξ value is accessible in such measurements, while t remains unavailable.

[3]At HERA it is usually denoted as $x_{\mathbb{P}}$ (Feynman-x of the Pomeron), while at the Tevatron and LHC ξ is used.

As was mentioned before, the diffractive exchange becomes dominant at large energies. In order to describe the DIS diffractive data at low values of β and high values of ξ, one needs to consider non-diffractive exchanges, by adding the Reggeon contribution [13]. It is usually assumed that Reggeon also follows a similar factorisation as Pomeron. This leads to the following formula:

$$f(x, \mu^2, \xi) = \Phi_{\mathbb{P}}(\xi, t) \cdot f_{\mathbb{P}}(\beta, \mu^2) + \Phi_{\mathbb{R}}(\xi, t) \cdot f_{\mathbb{R}}(\beta, \mu^2). \tag{1.4}$$

The DPDFs obtained in *ep* scattering experiments can be used to describe hard interactions in proton-(anti)proton collisions. By a convolution of the diffractive PDF with a non-diffractive PDF and the cross section for the hard parton-parton cross section one obtains the cross section for *hard single diffractive* production:

$$\mathrm{d}\sigma = S^2 \cdot \Phi_{\mathbb{P}}(\xi, t) \cdot f_{\mathbb{P}}(x_1/\xi, \mu^2) \cdot f_p(x_2, \mu^2) \cdot \mathrm{d}\sigma_{\mathrm{hard}}(x_1, x_2, \mu^2), \tag{1.5}$$

where $f_p(\beta, \mu^2)$ denotes the non-diffractive proton PDF. The additional factor S^2 denotes the *rapidity gap survival probability*. It takes into account a possibility of additional soft interactions between the initial or final state particles that would destroy the rapidity gap and the proton. In fact, the necessity of including the gap survival probability was discovered at the Tevatron collider, where the number of hard diffractive events was found smaller by a factor of about 10 than the extrapolations of the HERA measurements. Taking into account this additional factor, an agreement between the data and the extrapolation was obtained.

An example of diffractive process measured at the Tevatron is diffractive W production. The additional constraint on the kinematics, due to the forward proton tagging, allowed the CDF Collaboration to constrain the longitudinal momentum of the neutrino produced in the leptonic decay of the W boson. This allowed reconstruction of the W mass for each event, see Figure 1.11. Although the resolution of the reconstruction is quite bad, the measurement itself is quite interesting, since in non-diffractive production it is not possible to reconstruct the mass on the event-by-event basis.

In addition to hard single diffractive production, one can also observe the hard central diffractive process, in which two Pomerons are exchanged and two intact protons are present in the final state. A similar process, where one or both protons dissociate into low mass states, is also possible. The diagrams depicting the central diffractive production of jets and W/Z boson processes are shown in Figure 1.12 left and right, respectively. Both blobs represent the Pomeron structure and two Pomeron remnants are present in the final state. The cross section for this process can also be described in terms of DPDFs as

$$\mathrm{d}\sigma = S^2 \cdot \Phi_{\mathbb{P}}(\xi_1, t_1) \cdot \Phi_{\mathbb{P}}(\xi_2, t_2) \cdot f_{\mathbb{P}}(x_1/\xi_1, \mu^2) \cdot f_p(x_2/\xi_2, \mu^2) \cdot \mathrm{d}\sigma_{\mathrm{hard}}(x_1, x_2, \mu^2). \tag{1.6}$$

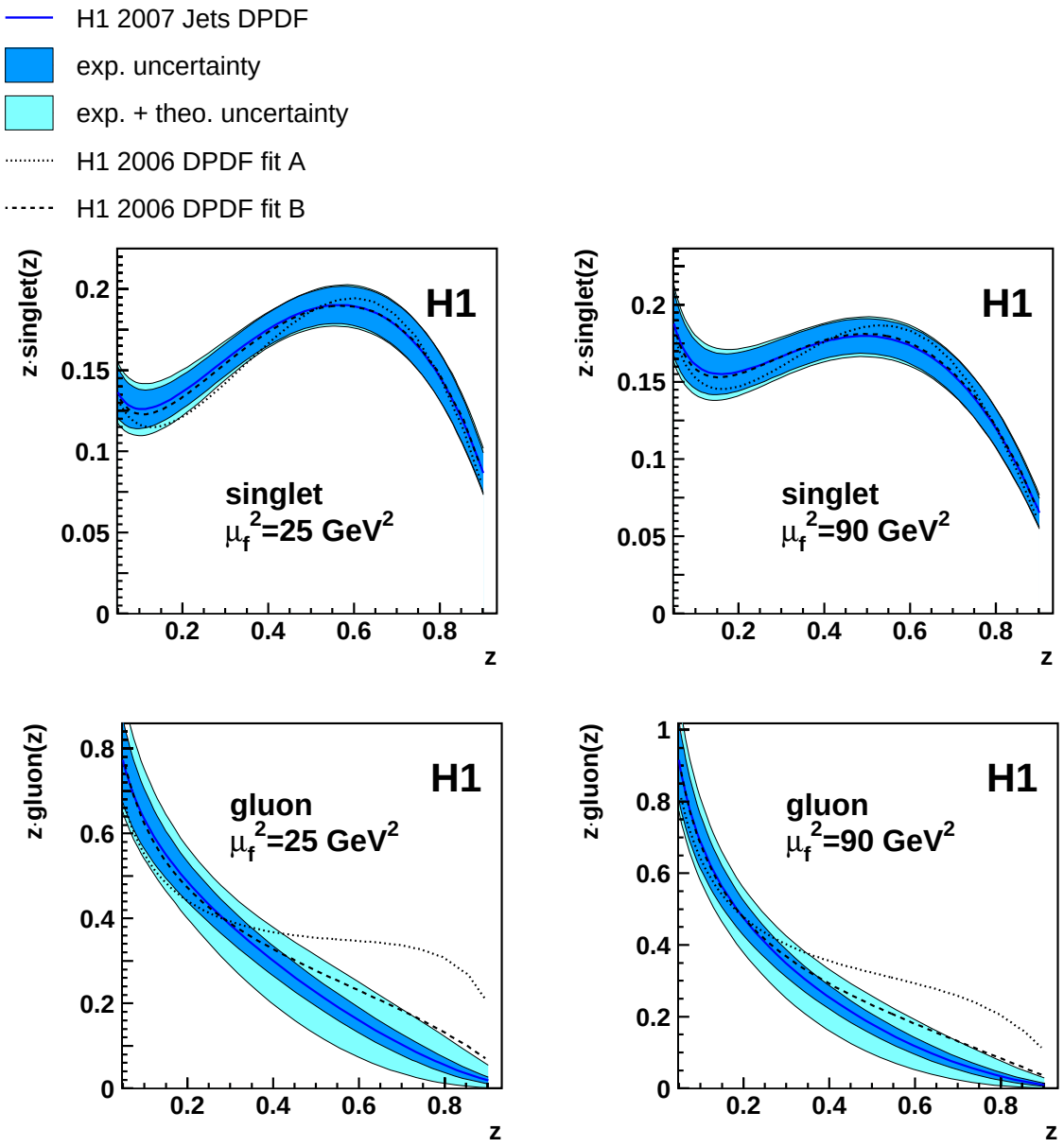

Figure 1.10: Diffractive quark (top) and diffractive gluon (bottom) densities for two values of the squared factorisation scale μ_f^2: 25 GeV^2 (left) and 90 GeV^2 (right). The solid line indicates the H1 2007 Jets DPDF, surrounded by the experimental uncertainty (dark shaded band) and the experimental and theoretical uncertainties added in quadrature (light shaded band). The dotted and dashed lines show the parton densities corresponding to the H1 2006 fit A and fit B from [13], respectively. [14]

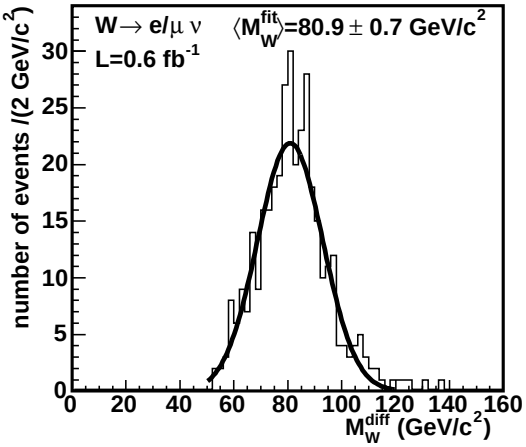

Figure 1.11: W boson mass distribution produced in a single diffractive process, as measured by the CDF Collaboration [15].

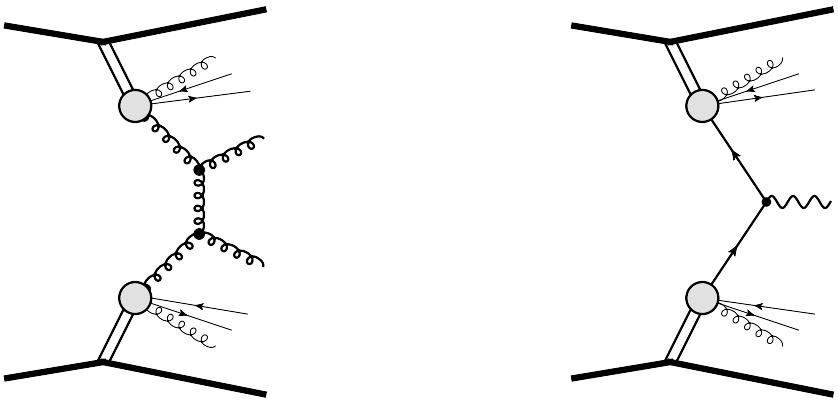

Figure 1.12: Feynman diagrams of the central diffractive production of jets (left) and W/Z boson (right).

1.3 Exclusive Production

A very interesting type of diffractive process is the *exclusive production*. Its name comes from a unique property – in this process it is possible to measure all final state particles. For usual interactions, both diffractive and non-diffractive, some of the produced particles (remnants of protons or Pomerons) go into the accelerator beam pipe and escape detection. For exclusive diffractive production, the only particles scattered into the beam pipe are the intact protons (p and $\bar{p}$ at the Tevatron). They can be register using dedicated detectors. All other particles are produced into the central rapidity region, this is why the process is sometimes called *central exclusive production*.

The most famous example is the exclusive production of the Higgs boson:

$$p + p \to p + H + p.$$

Such a process would have a great advantage over the standard, non-diffractive production for two reasons. First, it is the only possibility to study the $H \to b\bar{b}$ decay channel at the LHC. This is because, contrary to the non-diffractive case, the exclusive $b\bar{b}$ jet production is suppressed [16]. Second, the mass of the Higgs boson could be measured not only from its decay products, but also from the reconstructed kinematics of the intact protons. This would allow very precise measurements (accuracy of the order of 2%), since the energy loss of the protons can be reconstructed quite accurately, see Chapter 5. The main drawback of this process is a pretty small cross section, about 3 fb for a Higgs mass of 120 GeV [32], which is predicted at the edge of being observable at the LHC [17].

The mechanism of exclusive production is very interesting. It assumes that the Higgs is created in a gluon fusion via the t quark loop, like in the non-diffractive case. However, an exchange of a second gluon between the protons is also present and it ensures that the overall exchange is colour singlet and the protons stay intact. A diagram showing this mechanism is presented in Figure 1.13 (left). In a similar way jet and photon pairs can also be produced. The diagram presenting the mechanism of exclusive jets production is shown in Figure 1.13 (centre), the photon pair production requires a quark loop (Figure 1.13, right).

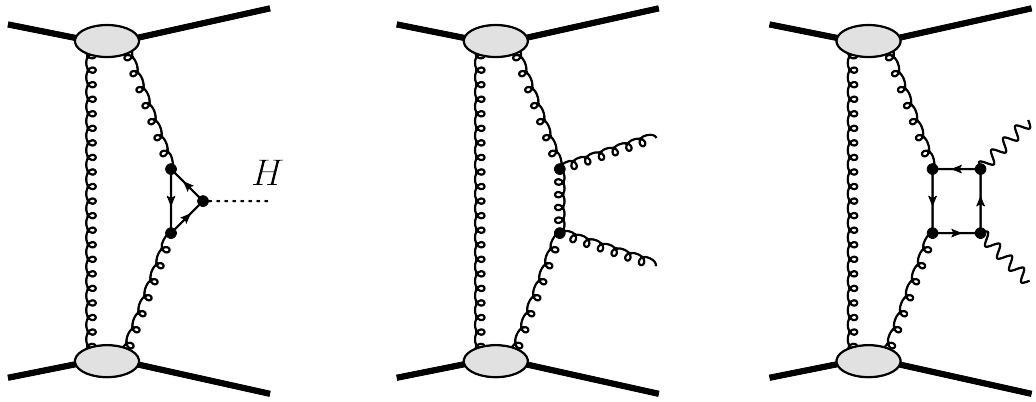

Figure 1.13: Feynman diagrams of the central exclusive production of the Higgs boson (left), jets (centre) and photon pairs (right).

The exclusive production has been already observed and measured at the Tevatron. Most of the measurements were done for the exclusive jets process. For example, Figure 1.14 presents the jet transverse energy dependence of the cross section as measured by the CDF Experiment [18]. Figure 1.15 shows the dijet mass distribution and an event display for an exclusive event candidate as obtained by the D0 Experiment [19].

It should be mentioned that the calculations based on the diagrams shown in Figure 1.13 are of perturbative nature and thus require a hard scale being present in the process. Processes of exclusive production, for which such a description is not

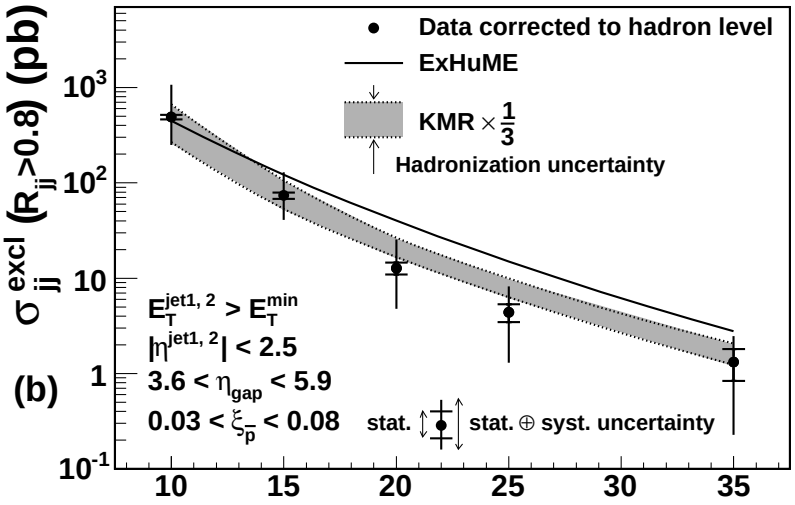

Figure 1.14: Cross section for central exclusive production of jets as a function of minimal jet transverse momentum, as measured by the CDF Collaboration. Predictions of the Monte Carlo generator (ExHuME), as well as of the theoretical calculation (KMR) are also presented. From [18].

adequate, also exist. For example in the pion pair production process [20]:

$$p + p \to p + \pi^+ + \pi^- + p,$$

the transverse momenta of the produced pions are quite small, of the order of 1 GeV. The diagram of this process is shown in Figure 1.16. The mechanism is based on the exchange of Pomerons between the protons and a virtual pion. This is a completely different approach. It does not take into account the proton constituents and the elementary interaction between them, but rather uses an effective description of the interactions. Chapter 4 contains a more detailed discussion on this process and the possibility of its measurement at the LHC.

When electromagnetic interactions are taken into account, two other mechanisms of exclusive production are possible. The first one, the $\gamma\gamma$ *interaction*, is not strictly speaking a diffractive interaction, because strong interactions are not involved and the exchanged object does not have vacuum quantum numbers. Nevertheless, it is very much connected to other kinds of exclusive production and, experimentally, can be measured in the same way. One of the most commonly considered two-photon processes is the production of lepton pairs. Its diagram is presented in Figure 1.17 (left). In a similar way pairs of W bosons can be produced. However, in addition to the diagram containing two triple γWW couplings, see Figure 1.17 (centre), the Standard Model predicts an additional one with a direct quartic $\gamma\gamma WW$ coupling. Such a process is very interesting, not only because it can give an insight into the electroweak sector by testing the existence of the quartic coupling, but also because it can be sensitive to various Beyond Standard Model (BSM) effects, as will be

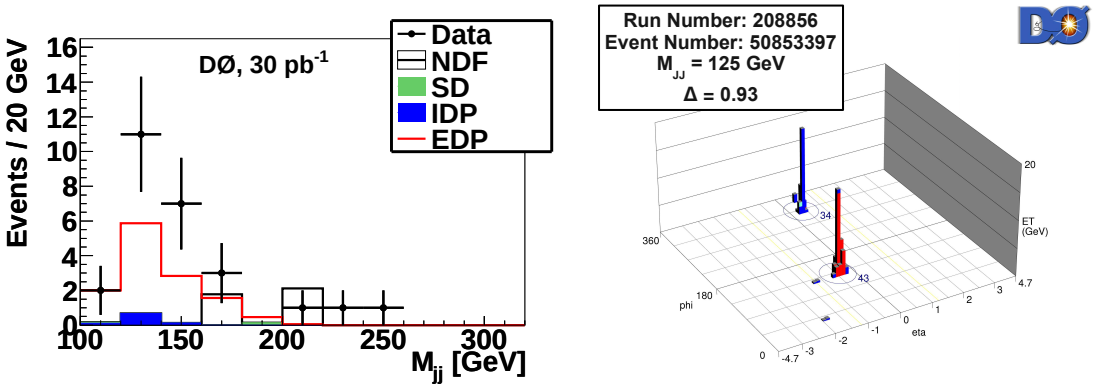

Figure 1.15: D0 results on exclusive jets production [19]. Left: Dijet mass distribution, right: a candidate for such a process. NDF, SD, IDP and EDP are the Monte Carlo predictions for the non-diffractive, single diffractive, central diffractive and exclusive jet production, respectively.

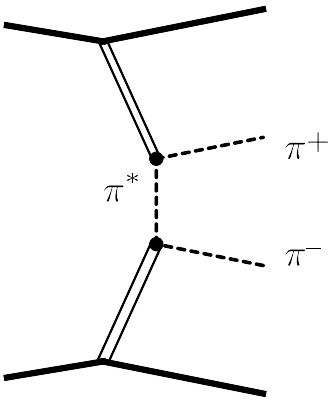

Figure 1.16: Feynman diagram of the charged pion pair central exclusive production.

discussed in Chapter 5.

The second type of exclusive production involving the electromagnetic interactions is the process of exclusive diffractive photoproduction. In this process one of the protons exchanges a photon, whereas the other a colour singlet, two-gluon system. As a result, a vector meson or a pair of jets can be produced. A very important feature of this process is that exactly the same one was studied at the HERA electron-proton collider [21]. The only differences are that at a hadron-hadron collider the photon is emitted from a hadron instead of an electron. At the LHC the available energy is much larger than at HERA. This will allow to verify the understanding of the production mechanism in a different regime. Also, heavier particles can be produced, for example the Z boson [22].

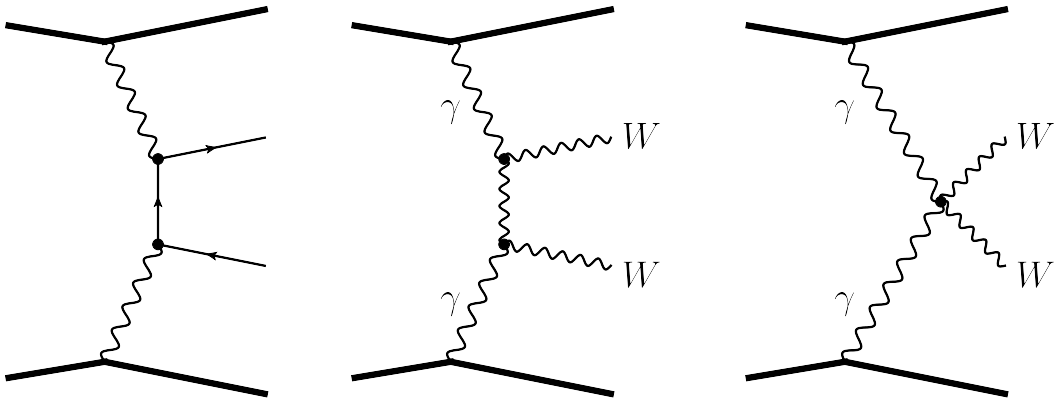

Figure 1.17: Feynman diagrams of the two-proton exchange processes. Left: lepton pair production, centre and right: diagrams contributing to production of W boson pairs.

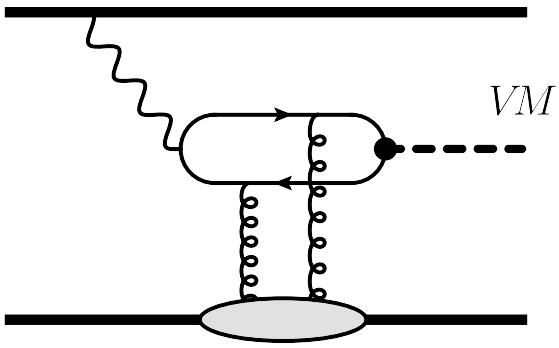

Figure 1.18: Feynman diagram of the vector meson photoproduction process.

Chapter 2

Uncertainties of Exclusive Production Models

Central exclusive production (CEP) is considered by many physicists one of the most interesting and exciting subject in the field of diffractive physics at the LHC. This is because it offers a possibility to study in detail both the production of the Higgs boson, as well as various phenomena of *new physics*. A great advantage of CEP is that measurements of the forward protons constrain the kinematics of the centrally produced state. This can lead, for example, to precise measurement of the Higgs boson mass. In addition, observation of Higgs produced exclusively will constrain its quantum numbers, since exclusive production of objects with quantum numbers different than 0^{++} is strongly suppressed.

The aim of this chapter is to discuss the uncertainties of the exclusive production models and to show that it is possible to constrain the uncertainties for Higgs production with the jets measurement. Such constraint could be very valuable for the feasibility study of the exclusive Higgs measurement at the LHC. In the following, the study published in [23] is presented. Since then, other measurements of CEP have been performed at the Tevatron [24]. Their results enable constraining the Higgs production further, without waiting for LHC data.

The work presented in this chapter was partially published in Phys. Rev. D83 (2011) 054013 and arXiv:1102.2531 [hep-ph].

2.1 The FPMC Generator

The Monte Carlo (MC) generators have become an irreplaceable tool for the measurements in particle physics, especially for collider physics. The reason is a great dependence of the measured observables on the detector resolution effects. First of

all, the detectors are very complicated – there is a great variety of sub-detectors of different types and an enormous number of read-out channels. The design of such detectors as well as their commissioning heavily relies on the MC methods and earlier measurements. At the LHC, not only the centre-of-mass energy is large and allows creation of a large number of particles, but also there can be dozens of simultaneous pp collisions within a single bunch crossing. This leads to an enormous amount of data that are read out for a single event. In order to reconstruct physical observables, very complex algorithms are needed. It is hard to imagine successful creation of such software without the use of Monte Carlo simulations.

The generators incorporate up-to-date knowledge about various physics processes. This includes both theoretical calculations performed at various orders of perturbative series as well as experimental input. The latter often comes in form of parametrisations derived from phenomenological analyses of various measurements. A typical example is the treatment of parton fragmentation and hadronisation into a final state jet of particles.

The MC generators deliver simulated events of a particular type. An event contains the kinematics of the selected process and information about all created particles, including their four-momenta. The final state particles are then processed through the detailed simulation of the detector, *i.e.* the simulation of the transport of these particles through the detector material. It also includes the simulation of the detector response, *i.e.* signals of the electronic channels. Such events can be treated in exactly the same way as real data – processed through the reconstruction algorithms.

The generated MC events are also crucial for the studies of physical processes. Their analysis gives a possibility to determine the ways to discriminate the background from the signal. This is because the differences between them can be small and it would be impossible to understand them without a Monte Carlo and detector simulation.

There are many MC generators on the market. Some of them, [25, 26], are the so-called general purpose generators, which include a large part of Standard Model processes. Other generators were designed for a specific type of processes. The FPMC (Forward Physics Monte Carlo) generator [27] is an example of the second kind and its purpose is forward physics, *i.e.* the physics with intact forward protons.

2.2 KMR and CHIDe Models

A short description of the exclusive production was given in Chapter 1, below a more detailed one is presented. The lowest order QCD description of exclusive production involves a two-gluon exchange between quarks. One gluon takes part in the hard interaction, while the second one makes the overall exchange a colour singlet (colour screening). The Feynman diagram of this process is shown in Figure

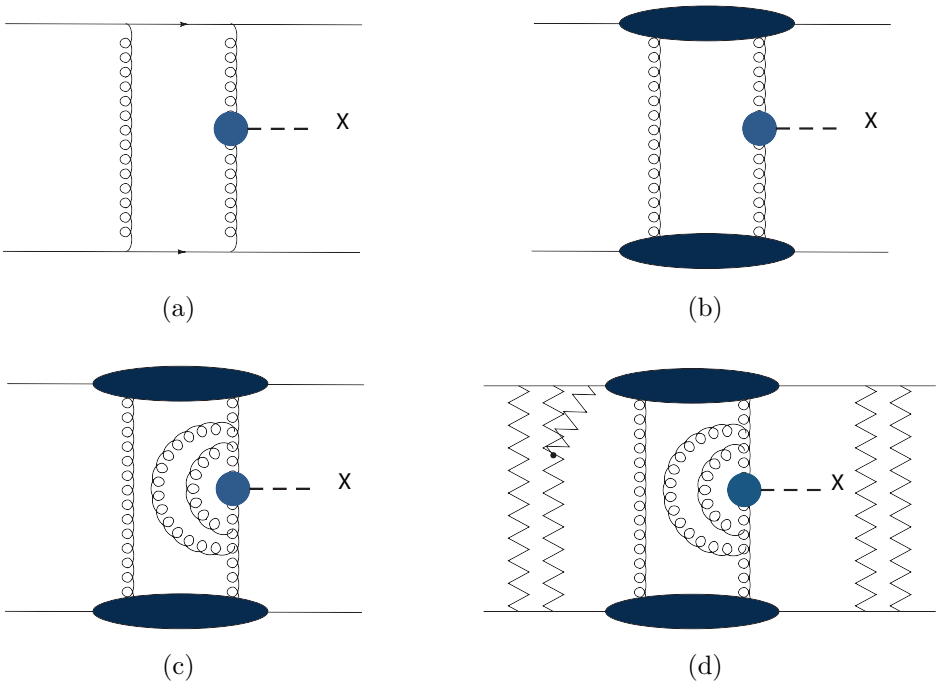

Figure 2.1: Schematic representation of the standard scheme of the exclusive cross section calculation with its various steps. (a) Parton level calculation, (b) impact factor, (c) Sudakov form factor and (d) rescattering corrections.

2.1(a), where X denotes the exclusively produced object – it can be a pair of jets, photons, the Higgs boson or other 0^{++} or 2^{++} particle or a system of particles that couples (directly or indirectly) to gluons. The calculation of this process is well understood and different approaches give compatible results [16, 28, 29, 30, 31].

In order to account for the fact that the interacting particles are the protons, not the quarks, and that they stay intact after the interaction, it is necessary to introduce the impact factor of the proton [33, 34, 35]. It is based on the skewed unintegrated gluon density [33] and its role is to describe the structure of the proton, see Figure 2.1(b).

One needs to take into account the possibility of additional gluon emissions in the process, see Figure 2.1(c)). In order to obtain an exclusive event, such emissions need to be suppressed. To account for this, the Sudakov form factor [36, 37, 38], also called the virtual vertex correction, is used. It has one of the greatest impacts on the final results. It suppresses the process cross section by 2 – 3 orders of magnitude. The Sudakov form factor depends on two scales, which define the momenta of the additionally emitted gluons. The hard (upper) scale is connected to the hard interaction ($gg \to X$). The soft (lower) scale is related to the transverse momentum of the gluons participating in the hard interaction.

Last but not least, additional soft exchanges can take place between the initial or final state protons, see Figure 2.1(d). Such interactions lead to dissociation of the

proton and to the destruction of the rapidity gaps. The event cannot be any longer recognised as exclusive. To take this into account, the cross section is multiplied by the rapidity gap survival probability.

The process of exclusive Higgs production has been proposed in [28]. The first complete calculation was done by the Durham Group [16, 37] – the Durham or KMR model. This model includes the production of the Higgs boson, jets, χ_c, photon pairs and also supersymmetric particles [39]. In this section, only the jet and Higgs production is considered.

The kinematics of the exclusive production process is introduced in Figure 2.2(a). Fractional momenta of the gluons are denoted by x, x_1 and x_2, $\mathbf{k}$ is their transverse momentum and μ is the scale of the process, related to the mass of the produced object. In the KMR model the cross section for the exclusive process factorises into the effective luminosity $\mathcal{L}$ and the cross section of the hard sub-process $\hat{\sigma}$ [16, 37]:

$$\sigma = \mathcal{L} \times \hat{\sigma}(gg \to X), \tag{2.1}$$

where X is the centrally produced system – either a pair of gluons in the jet production case or the Higgs boson. In the effective luminosity formula, the dependence on the proton four-momentum transfers is exponential and the protons azimuthal angles are distributed uniformly:

$$\frac{\partial\sigma}{\partial\hat{s}\partial\hat{y}\partial t_1\partial t_2} = e^{B(t_1+t_2)}\frac{\partial\mathcal{L}}{\partial\hat{s}\partial\hat{y}}\mathrm{d}\hat{\sigma}\left(gg \to H\right), \tag{2.2}$$

the t-slope of the cross section $B = 4$ GeV^2 taken from the fit to the soft hadronic data [16] is assumed. The remaining dependence on the energy of the intact protons appears via the dependence on the centre-of-mass energy of the central state, $\hat{s}$, and its boost, $\hat{y}$:

$$\hat{s} = s\xi_1\xi_2, \qquad \hat{y} = \frac{1}{2}\ln\frac{\xi_1}{\xi_2}, \qquad \mathrm{d}\hat{s}\mathrm{d}\hat{y} = s\mathrm{d}\xi_1\mathrm{d}\xi_1,$$

The sub-process cross section for Higgs production, $\hat{\sigma}(gg \to H)$, includes an additional scale factor equal to 1.5, which takes into account next-to-leading-order corrections [32]. The effective luminosity is given by

$$\frac{\partial\mathcal{L}}{\partial s\partial y} = \left(\frac{\pi}{(N_c^2-1)}\int\frac{\mathrm{d}\mathbf{k}^2}{\mathbf{k}^4}f_g\left(x,x_1,\mathbf{k}^2,\mu^2\right)f_g\left(x,x_2,\mathbf{k}^2,\mu^2\right)\right)^2, \tag{2.3}$$

where f_g is the unintegrated skewed gluon density given by [33]:

$$f_g\left(x,x_1\ll x,\mathbf{k}^2,\mu^2\right) = R_g\frac{\partial}{\partial\log\mathbf{k}^2}\left[\sqrt{T(\mathbf{k},\mu)}\,xg(x,\mathbf{k}^2)\right]. \tag{2.4}$$

The $g(x,\mathbf{k}^2)$ function is the standard integrated gluon density, R_g takes into account

the skewness of the distribution (the fact that $x \neq x_1$) and is close to 1.2 at $\sqrt{s} =$ 14 TeV. The Sudakov form factor $T(\mathbf{k}, \mu)$, where $\mathbf{q}$ and z are the transverse and longitudinal components of the additional partons momenta, is given by:

$$T(\mathbf{k}, \mu) = \exp\left[- \int_{\mathbf{k}^2}^{\mu^2} \frac{\mathrm{d}\mathbf{q}^2}{\mathbf{q}^2} \frac{\alpha_s\left(\mathbf{q}^2\right)}{2\pi} \int_0^{1-\Delta} \left(z P_{gg}(z) + \sum_q P_{qg}(z) \right) \mathrm{d}z \right], \tag{2.5}$$

and P_{gg} and P_{qg} are the quark and gluon splitting functions. The integration limits are Δ, μ_{jj} for the jets case and μ_H for the Higgs [16, 38]:

$$\Delta = \frac{|\mathbf{q}|}{|\mathbf{q}| + \mu}, \qquad \mu_{jj} = 0.62\sqrt{\hat{s}}, \qquad \mu_H = m_H. \tag{2.6}$$

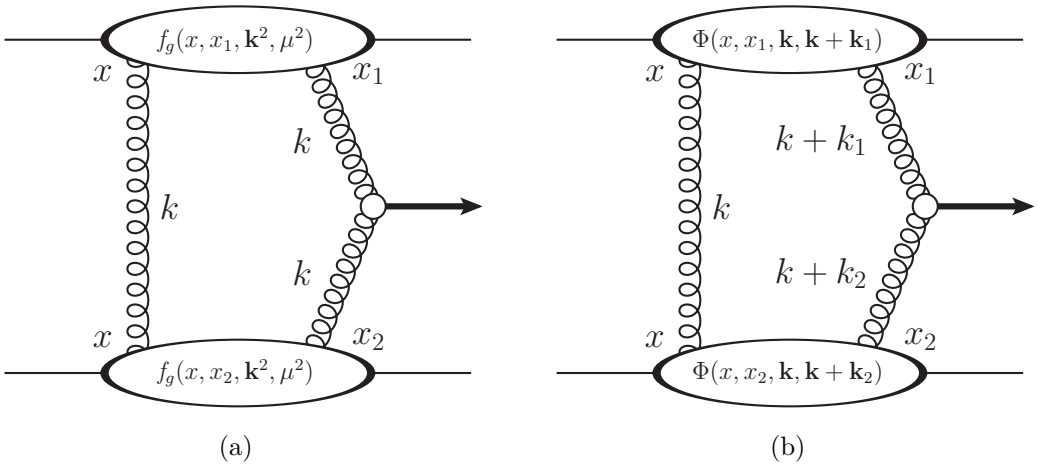

Figure 2.2: Schematic representation of the exclusive diffractive production amplitude in the CHIDe model, x, x_1 and x_2 are the fractional momenta of the exchanged gluons, $\mathbf{k}$, $\mathbf{k} + \mathbf{k}_1$ and $\mathbf{k} + \mathbf{k}_2$ are their transverse momenta, Φ is the proton impact factor.

Several other groups have performed similar calculations as the Durham Group, which were based on similar principles as the KMR model. In the following the CHIDe model [40, 41, 42] for jets and Higgs boson production developed by the Liège Group is presented. This model is based on similar principles as the KMR one but differs in details of the calculations, as explained in the following. The kinematic variables are defined in Figure 2.2(b) and the cross section is obtained as:

$$\sigma \simeq S^2 \left[\int \frac{\mathrm{d}^2\mathbf{k}\, \mathrm{d}^2\mathbf{k}_1\, \mathrm{d}^2\mathbf{k}_2}{\mathbf{k}^2 (\mathbf{k}+\mathbf{k}_1)^2 (\mathbf{k}+\mathbf{k}_2)^2} \Phi(x, x_1, \mathbf{k}, \mathbf{k}+\mathbf{k}_1) \times \right.$$
$$\left. \Phi(x, x_2, \mathbf{k}, \mathbf{k}+\mathbf{k}_2) \sqrt{T(\ell_1, \mu)}\, \mathcal{M}(gg \to X) \sqrt{T(\ell_2, \mu)} \right]^2, \tag{2.7}$$

where Φ is the impact factor, $T(\ell_i, \mu)$ is the Sudakov form factor, $\mathcal{M}(gg \to X)$

is the hard sub-process amplitude. The proton impact factor includes the skewed unintegrated gluon density and a phenomenological, low energy, model of the proton. Similarly to the KMR model, the four-momentum transfer from the proton is assumed to be exponential. The unintegrated gluon density consists of the hard and soft components. The hard part is obtained from the differentiation of the standard, integrated gluon densities (GRV [43], MRS [44] and CTEQ [45]). The soft component models the Pomeron exchange in the non-perturbative regime. Four variants of the soft component are available [46, 47]. They reflect the present uncertainty on the unintegrated gluon distributions, which leads to uncertainties on the predictions.

The Sudakov form factor is identical to that in the KMR model:

$$T(\mathbf{k},\mu) = \exp\left[-\int_{\mathbf{k}^2}^{\mu^2} \frac{\mathrm{d}\mathbf{q}^2}{\mathbf{q}^2} \frac{\alpha_s\left(\mathbf{q}^2\right)}{2\pi} \int_0^{1-\Delta} \left(zP_{gg}(z) + \sum_q P_{qg}(z)\right) \mathrm{d}z\right]. \tag{2.8}$$

The upper integration limit in the Higgs production case is set to the Higgs mass [38]. For dijet production it is fixed to the transverse momentum exchanged in the hard vertex. This is one of the main differences with respect to the KMR model, where the invariant mass of the produced gluon system is taken for the upper integration limit. Although it could seem that this difference is relevant only for the jet production, since for the Higgs production both models use the same upper limit, this is not the case. In fact, the parameters of the CHIDe model have been obtained from the fit to the CDF jet data. These parameters are then used to obtain the predictions for Higgs production, which in consequence depend on the upper limit used for jets.

In the CHIDe model an additional K factor introducing the NLO correction is also included the Higgs case.

2.3 Implementation of Exclusive Production

The KMR and CHIDe models have been implemented in FPMC. This allows a direct comparison of both models using the same framework. Figure 2.3 presents the cross section (without any additional cuts) for exclusive Higgs boson production at $\sqrt{s} = 14$ TeV as a function of the Higgs boson mass m_H for the CHIDe model and several implementations of the KMR model. The KMR implementations include the ExHuME generator [48] and two FPMC KMR versions. The first FPMC implementation, *FPMC KMR*, takes the original value of the upper Sudakov scale of $0.62 \cdot m_H$, while *FPMC KMR corrected* sets it to m_H [38]. The cross section decreases with increasing Higgs mass. For a Higgs mass of 120 GeV the cross section ranges between 0.7 and 3 fb. In addition, the results of the original KMR calculation [32] is presented – *KMR (2002)*.

The ExHuME generator predicts the cross section values very close to the original calculations. Other implementations of the KMR model and the CHIDe model

predict smaller values. There are two effects that cause the difference between the FPMC and the ExHuME implementations of the KMR model. First, the treatment of the gluon distribution in eq. (2.3) is different. In ExHuME the value of the gluon distribution is set to be a constant for $\mathbf{k}^2$ smaller than about 1 GeV. In FPMC the implementation is different: the integration in eq. (2.3) begins from a cut-off value $\mathbf{k}^2 = 2$ GeV^2. The value of the cut-off is chosen such that the Tevatron data are well described, see in the following. A different approach is proposed in the CHIDe model, which uses a parametrisation of the soft region. The other reason of the disagreement is a different implementation of the hard sub-process. In FPMC the Higgs is created and then its decay is performed, whereas the ExHuME implementation involves the calculation of the Higgs propagator.

In addition, a difference between the Higgs production cross sections predicted by the KMR and CHIDe models can be observed. The CHIDe model predicts smaller cross sections, which show slightly steeper dependence on the Higgs boson mass.

The predictions for the exclusive jet production cross section at $\sqrt{s} = 14$ TeV as a function of the jet minimal transverse energy is presented in Figure 2.4. The KMR model predicts a higher value of the cross section and a steeper dependence than the CHIDe model.

In theoretical calculations it is difficult to account for effects like jet fragmentation, which may lead to three jets in the final state. In addition, the jet finding algorithm used in experimental analyses can affect the energy of reconstructed jets. All these effects can be taken into account using Monte Carlo generated data, which allows a correct comparison of the model predictions and the experimental results. Naturally, the Monte Carlo implementation of exclusive processes is not only modifying the output cross section in the generator, but it needs to take into account the characteristic structure of the event, namely the intact protons, lack of the underlying events and correct colour flow.

In the following, the KMR and CHIDe models are tested against the measurements performed at the Tevatron collider by the CDF Collaboration [18]. The $p\bar{p}$ collisions were studied at $\sqrt{s} = 1.96$ TeV. The CDF detector was equipped with a *Roman Pot Spectrometer* (RPS), foreseen to tag the intact anti-protons scattered in diffractive processes. The events were required to have two reconstructed jets, a tagged anti-proton and a rapidity gap on the proton side. Such requirements lead to the selection of the central diffractive (DPE) jet processes. The dijet mass fraction, R_{jj}, is defined as the ratio of the dijet invariant mass to the total mass of the event computed using the calorimeter. This distribution is plotted in Figure 2.5. In case of a DPE process, the energy of the Pomeron remnants present in the event leads to R_{jj} values smaller than one. In exclusive events, where there are no remnants, the value of the ratio is expected to be close to unity. This is indeed observed in Figure 2.5, where the excess above the DPE prediction for high values of R_{jj} is clearly seen. This allowed to separate the exclusive and inclusive (DPE) diffractive contributions

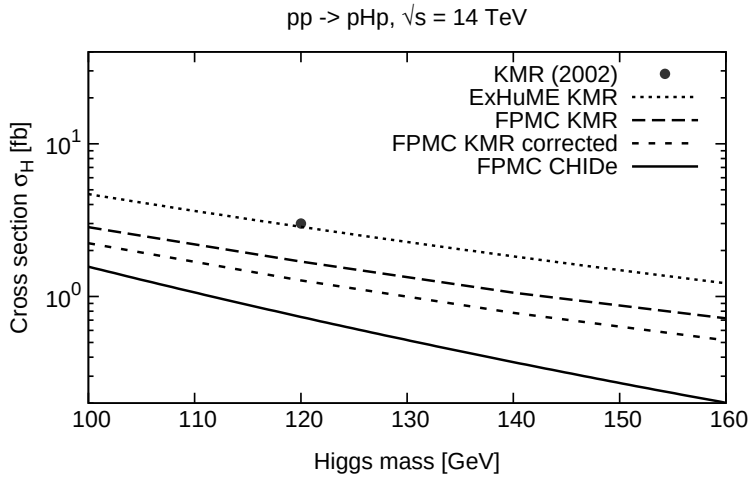

Figure 2.3: Cross section for exclusive Higgs boson production at the LHC as a function of the Higgs boson mass. Predictions of the CHIDe and KMR models implemented in FPMC are presented. For comparison the implementations of the original KMR model [32] (black point) and the ExHuME generator are given. In addition the effect of changing the upper Sudakov scale from $0.62m_H$ to m_H in the KMR model is presented (FPMC KMR corrected).

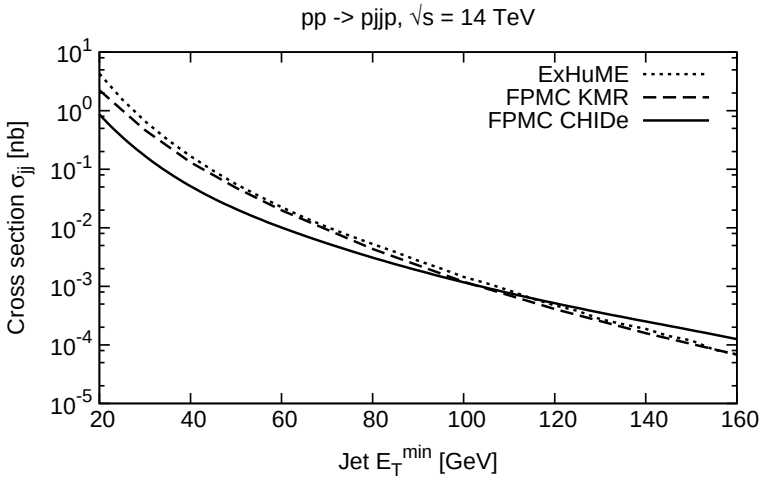

Figure 2.4: Cross section for exclusive jet production at the LHC as a function of the minimum jet E_T. Predictions of CHIDe and KMR are presented. For comparison the results of the ExHuME generator are given.

and to measure the exclusive diffractive dijet cross section as a function of the minimum jet E_T shown in Figure 2.6, see also [49]. These data are the basis for the following analysis.

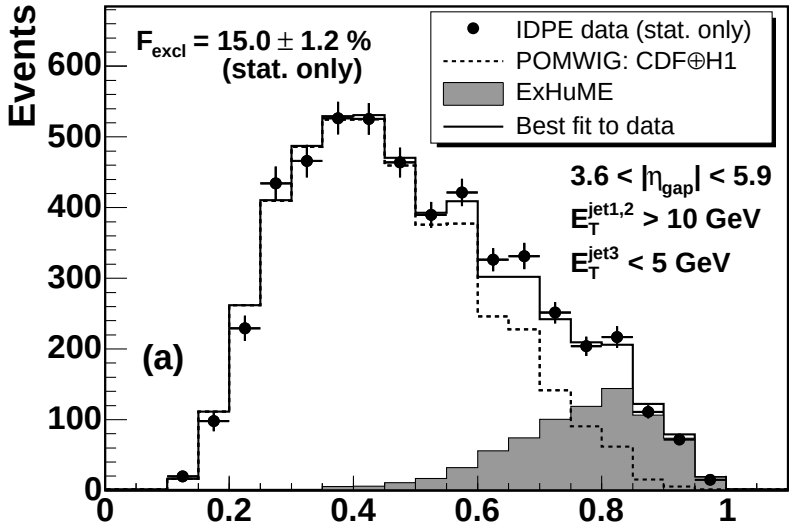

Figure 2.5: Dijet mass fraction for the DPE events as measured by CDF [18].

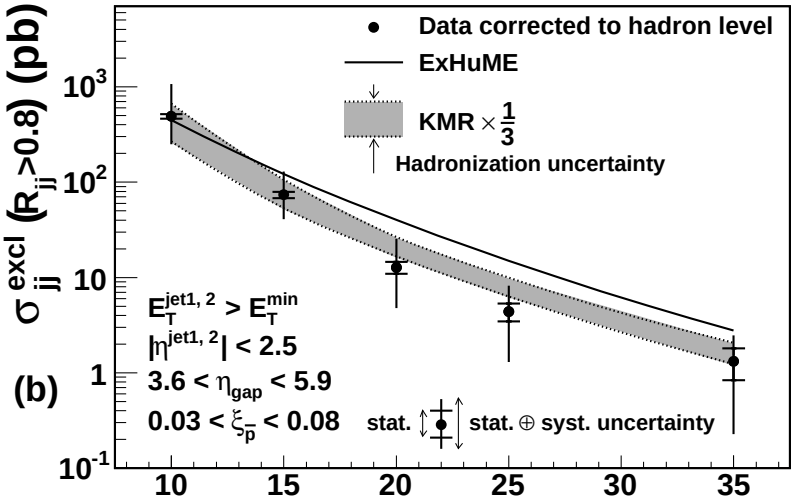

Figure 2.6: Cross section for exclusive jet production at $\sqrt{s} = 1.96$ TeV as a function of minimum jet transverse energy, as measured by CDF [18].

The predictions of the KMR and CHIDe models, obtained using their FPMC implementation and the 0.7 cone jet algorithm applied at particle level, are compared to the CDF measurement of exclusive jets, see Figure 2.7. The selection of the generated events followed the one used in the CDF measurement, in particular including a veto on the third jet with transverse energy greater then 5 GeV. The CDF data have been corrected to the hadron level. Such procedure takes into account various experimental effects like detector acceptance, jet energy scale and jet energy resolution. The corrected data allow for a critical comparison with hadron level Monte

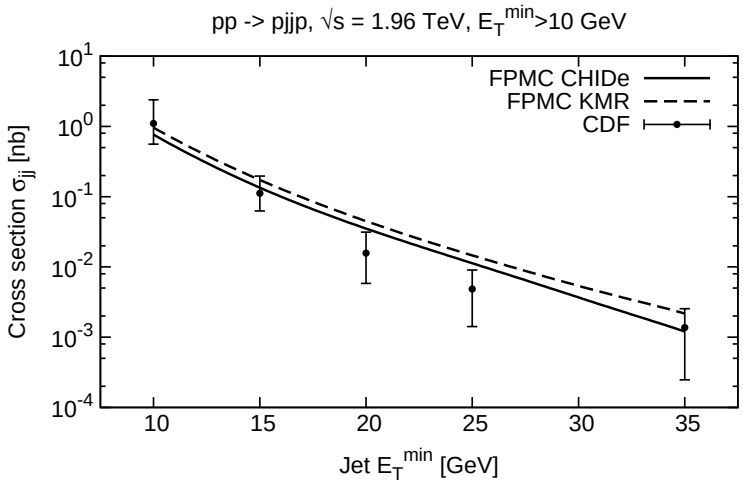

Figure 2.7: Exclusive jet production cross section at the Tevatron as a function of the minimum jet E_T. The CDF measurements are compared to the CHIDe and KMR models displayed after applying the CDF jet algorithm.

Carlo predictions, which correctly accounts for the most important effects like the parton showers, hadronisation and jet finding algorithm. Both KMR and CHIDe models describe the data equally well and the differences between their predictions are small compared to the experimental uncertainties. A slightly different dependence on the minimal transverse energy of the jet can be noticed. However, the uncertainty of the measurement is large, which does not allow any firm conclusion.

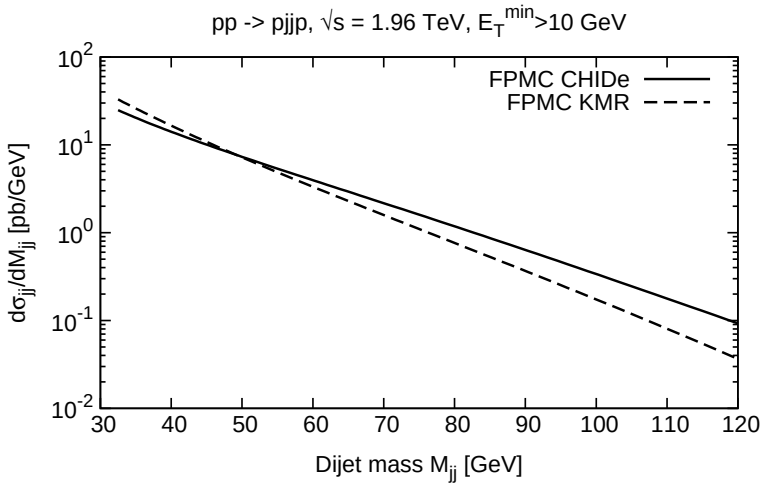

Figure 2.8: Dijet mass cross section for exclusive jet production at the Tevatron for the CHIDe and KMR models.

Figure 2.8 displays the dijet mass M_{jj} distribution predicted by the KMR and CHIDe models. For both models the predicted trend is similar, however KMR leads to a slightly steeper dependence. The CDF Collaboration published also the exclusive jet cross section as a function of the dijet mass, see Figure 2.9. It is worth to point out that this is actually not a direct measurement, but an extraction based

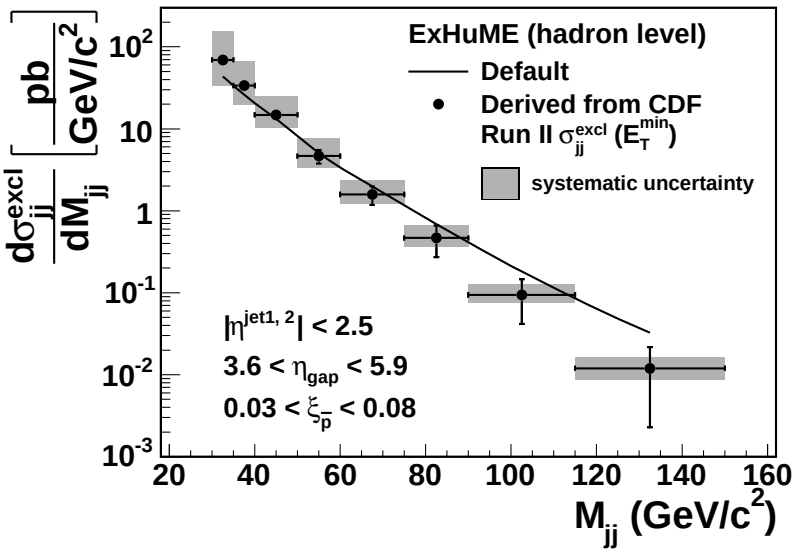

Figure 2.9: Distribution of the dijet mass in the exclusive jet production events at $\sqrt{s} = 1.96$ TeV, as obtained by CDF [18].

on the $E_T^{\min}$ measurement and MC predictions. In the following it will be referred to as the *pseudo-data*. The method to obtain the results was to compare the ExHuME predictions to the measured jet E_T threshold cross section. The MC events were re-weighted to match the measured E_T^{min} spectrum and the M_{jj} distribution was plotted. Obviously, this method may depend on the Monte Carlo generator used, since the jet E_T and dijet mass are not directly related.

In order to test the models implemented into FPMC, this procedure was repeated for each of them. The obtained pseudo-data are compared to the default KMR and CHIDe model predictions in Figures 2.10 and 2.11, respectively. The obtained pseudo-data distributions on both plots differ slightly from each other as well as from the one published by CDF. This confirms the dependence on the generator used in the procedure mentioned before. On the other hand, one can see that in both plots the pseudo-data and the generator predictions (grey histogram) are compatible. This shows that the FPMC implementations reproduce well the CDF measurement discussed above.

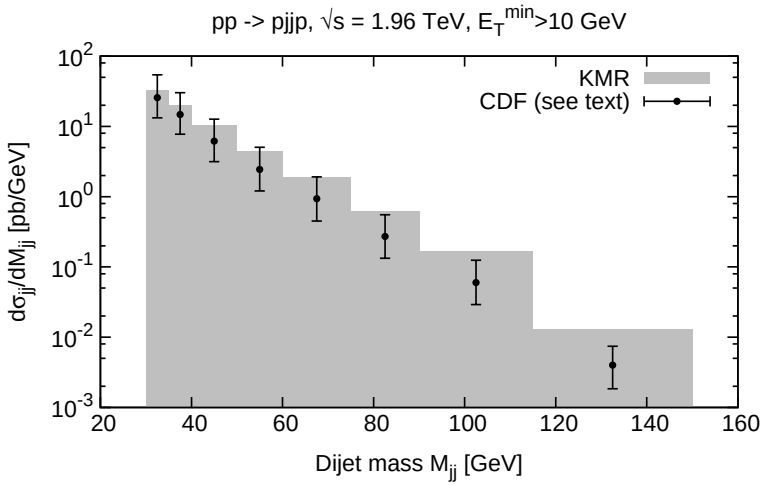

Figure 2.10: Dijet mass distribution extracted from the CDF measurement of exclusive jet production compared to the KMR model.

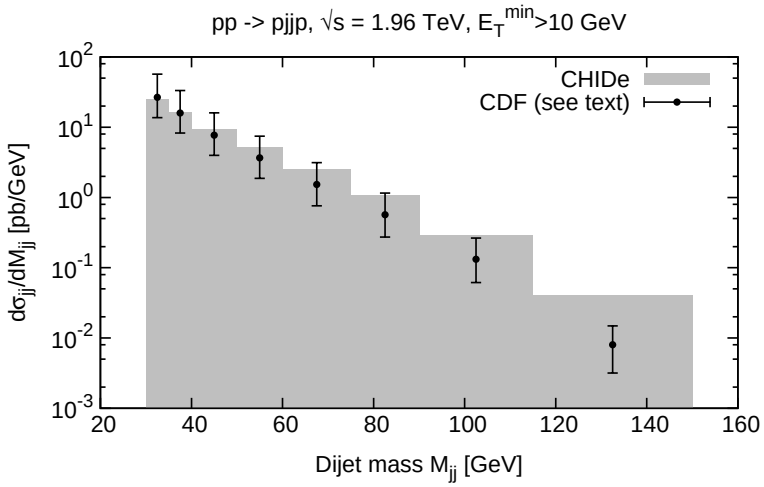

Figure 2.11: Dijet mass distribution extracted from the CDF measurement of exclusive jet production compared to the CHIDe model.

2.4 Sources of Uncertainty

The models of exclusive production have been explained in detail before. The aspects of the calculations that lead to uncertainties on the predictions are discussed in this section. The study is performed with the CHIDe model implemented within the FPMC generator. However, the discussion is quite general, since all models are based on similar principles.

In exclusive models, only the calculation of the Feynman diagram is precise and does not carry any uncertainties. The rest of the calculation ingredients come from less precise considerations and are given only approximately. The first considered element is the gap survival probability. Historically, it has been introduced to explain the Tevatron results that showed smaller amount of hard diffractive production than

it was expected from extrapolations of the measurements performed at HERA. To describe the data, a factor of 0.1 was introduced and interpreted as the probability that there was no additional soft, long-range interaction that would destroy the rapidity gaps, apart from the hard interaction. The value of this factor at the LHC is predicted to be 0.03 at $\sqrt{s} = 14$ TeV [50]. In the following analysis the uncertainty on this factor is neglected, because it is common for many processes and it should be quite easy to constrain it as soon as any diffractive LHC data (not only the exclusive, but also SD and DPE) are available.

The next source of model uncertainty is the uncertainty on the unintegrated gluon distribution in the proton. In the CHIDe model, its main part comes from the soft contribution, which is known very poorly, contrary to the hard part. This uncertainty is accounted for by providing four versions of gluon distributions, differing in the soft contribution [35]. Using the CHIDe model implemented into the FPMC generator, predictions based on different gluon distributions can be compared to the data on exclusive jets from the CDF measurement. The comparison is presented in Figure 2.12. An agreement between the data and all four distributions can be noticed. One can see that the fit no. 4 describes the data best, however this does not really favour this particular fit versus the others. The reason is that this fit is the default one in the CHIDe model and that the values of other parameters (x and x', see in the following) have been chosen so that the data are described well. For all four fits it would be possible to obtain a similar level of compatibility with a different, but equivalent choice of the parameters.

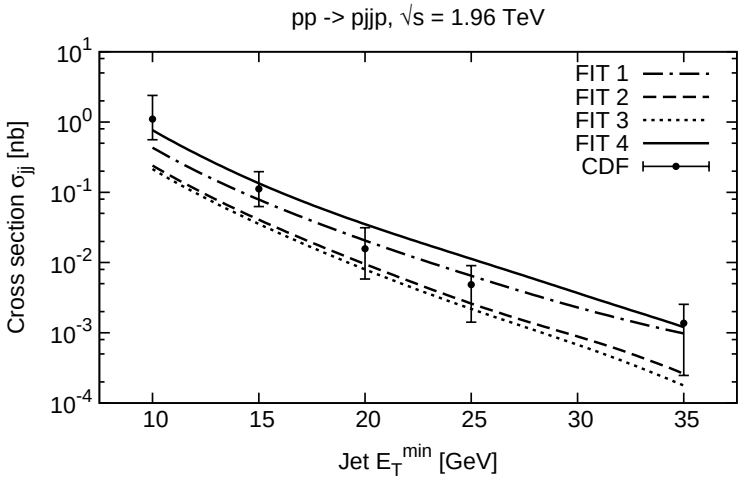

Figure 2.12: Effect of changing the gluon distribution on exclusive jet production at the Tevatron.

Figure 2.13 shows the estimation of the uncertainty at $\sqrt{s} = 14$ TeV for the exclusive jet production due to the uncertainty on the gluon distribution. For comparison, the uncertainty of the KMR model obtained with FPMC is also given. Figure 2.14 shows the predictions for exclusive Higgs production at the LHC. One

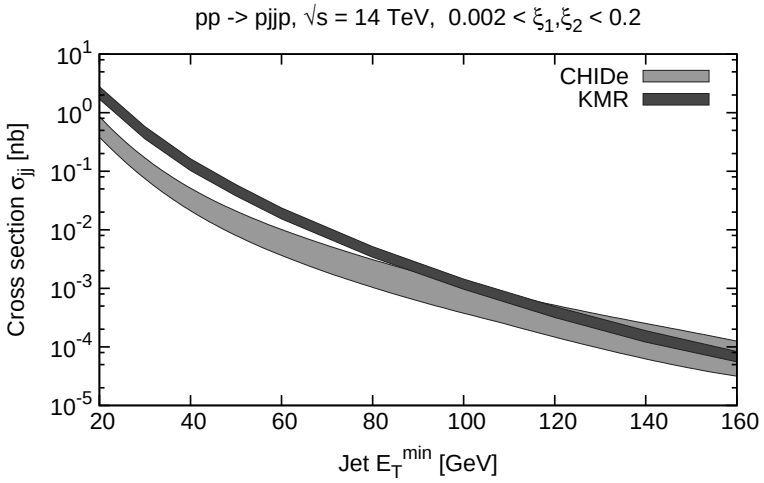

Figure 2.13: Effect of changing the gluon distribution on exclusive jet production at the LHC.

can see that the uncertainty due to the gluon distributions is approximately independent of the jet transverse momentum and the Higgs mass. For jet production it is larger than for the Higgs boson case and equals about a factor of 3 and a factor of 2, respectively.

A comment is needed about the way the uncertainty was calculated in case of the KMR model. The soft region of the unintegrated gluon distributions is not parametrised, instead a cut-off is used when integrating the distribution. The default value of this cut-off in the FPMC generator is 2 GeV, as mentioned above. The KMR uncertainty bands showed in Figures 2.13 and 2.14 were obtained by varying the cut-off from the minimal possible value (1.26 GeV^2 in the case of the MRST2002 PDF set) to 3.0 GeV^2. It should be pointed out that the assumptions used to calculate the uncertainty in both models are completely different. Nevertheless, the obtained uncertainties are very close, which suggests that the obtained estimate is correct.

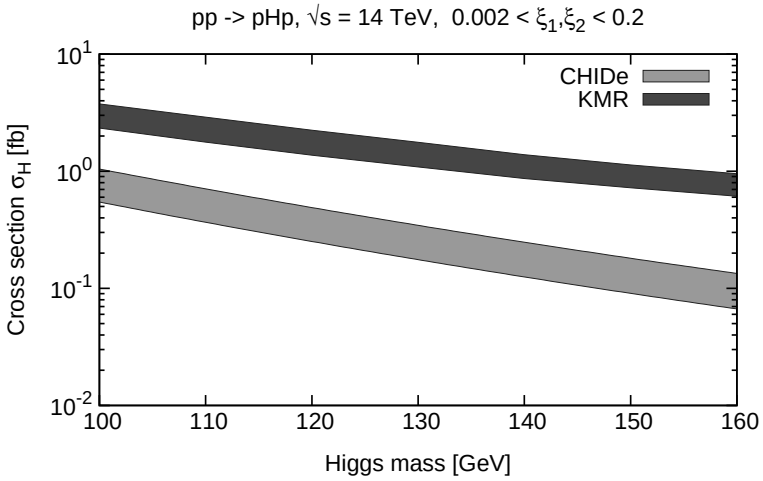

Figure 2.14: Effect of changing the gluon distribution on exclusive Higgs production at the LHC.

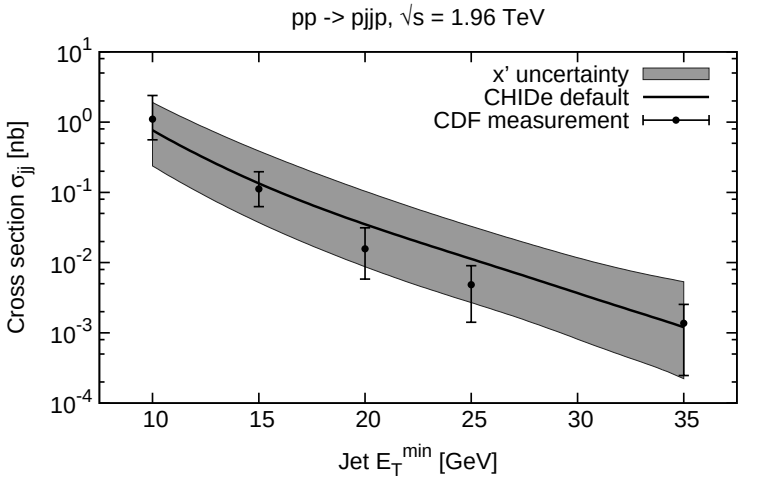

Figure 2.15: Effect of varying the lower limit of the Sudakov form factor on exclusive jets production at the Tevatron.

The last source of uncertainty is the Sudakov form factor. For the case of exclusive jets, both limits of the Sudakov integral are known only up to the order of magnitude. For the sake of this analysis the values of the limits were modified by two additional parameters, x and x':

$$T(l_i,\mu) = \exp\left[-\int_{l_i^2/x'}^{\mu^2/x} \frac{\mathrm{d}\mathbf{q}^2}{\mathbf{q}^2}\frac{\alpha_s\left(\mathbf{q}^2\right)}{2\pi}\int_0^{1-\Delta}\left(zP_{gg}+\sum_q P_{qg}(z)\right)\mathrm{d}z\right]. \tag{2.9}$$

This is slightly different for exclusive Higgs production. It has been shown [38] that the upper scale should be exactly equal to the mass of the Higgs boson. The lower limits in the two Sudakov form factors in eq. (2.7) are equal to $\mathbf{k}+\mathbf{k}_1$ and $\mathbf{k}+\mathbf{k}_2$, respectively. However, there are other uncertainties present in the Higgs

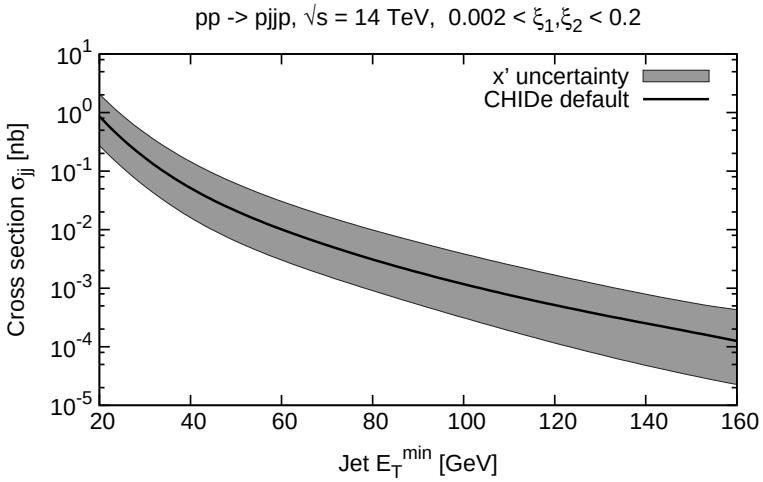

Figure 2.16: Effect of varying the lower limit of the Sudakov form factor on exclusive jets production at the LHC.

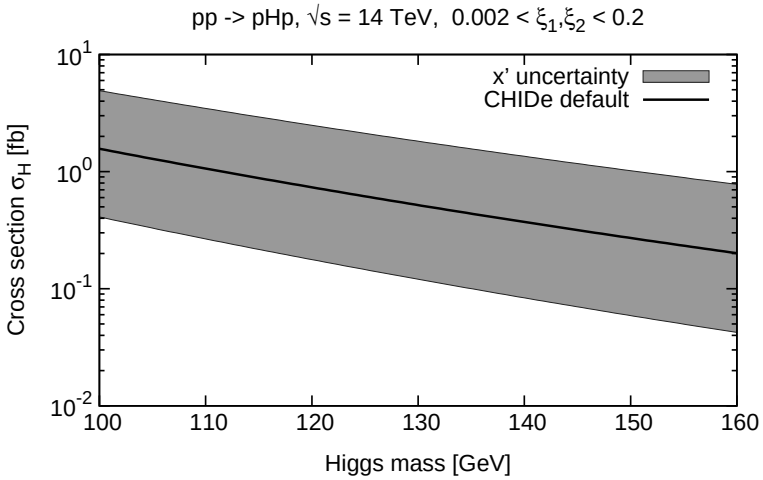

Figure 2.17: Effect of varying the lower limit of the Sudakov form factor on exclusive Higgs production at the LHC.

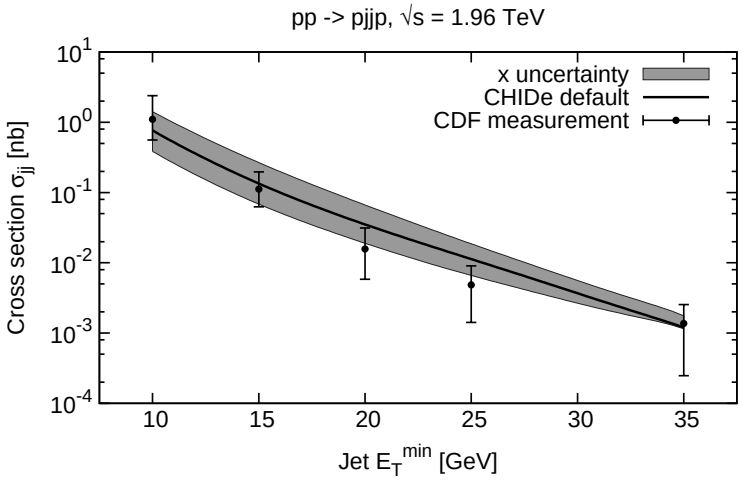

Figure 2.18: Effect of varying the upper limit of Sudakov form factor on exclusive jets production at the Tevatron.

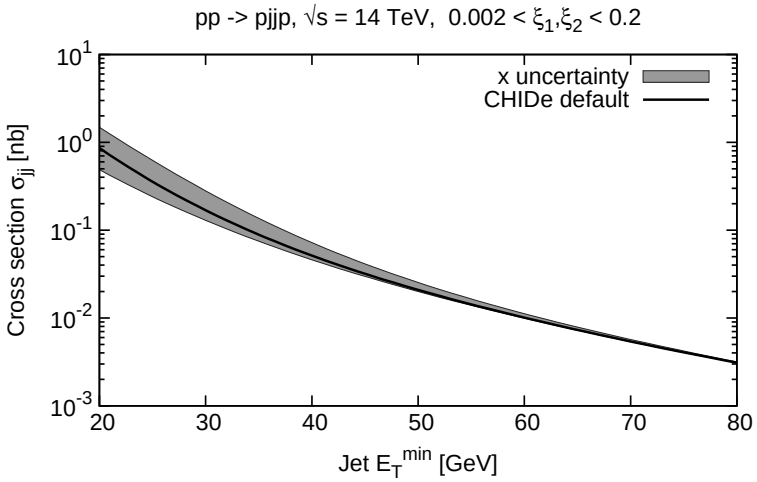

Figure 2.19: Effect of varying the upper limit of the Sudakov form factor on exclusive jets production at the LHC.

case calculation and they can be taken into account by varying the lower scale [23]. At this place it should be mentioned that there is no consensus on the uncertainty connected to the lower scale, and the CHIDe group takes it into account, while the KMR group does not. This is an important difference, because allowing the lower scale to vary indirectly affects the predictions of the CHIDe models. The reason for this is that the default value of the x' parameter is 0.5, chosen to describe the CDF measurement of exclusive jets production [51]. In the KMR model this parameter equals 1, which leads to a large difference in the prediction of the exclusive Higgs production cross section.

In order to see how the uncertainty on the lower scale affects the value of the cross section, the x' parameter was varied by a factor of 2. Increasing its value causes the increase of the integral value and reduces the cross section, see eq. (2.9), while decreasing the parameter causes the increase of the cross section. The results of the variation can be seen in Figures 2.15, 2.16 and 2.17, where the cases of jets production at the Tevatron, jets at the LHC and Higgs at the LHC are presented. For all these cases the uncertainty due to the variation on x' by a factor of 2 leads to the change of the cross section by a factor of 5. This change is roughly independent of the process and the energy scale considered.

The value of the parameter x, which specifies the upper limit on the Sudakov form factor, leads to an uncertainty only for the jets case. For the exclusive Higgs its value is fixed to 1, as discussed before. For the jets production, the default value of the x parameter is 0.5. To see the effect on the cross section, the parameter is varied by a factor of two. The results are presented in Figures 2.18 and 2.19, for Tevatron and LHC, respectively. Decreasing the value of the parameter increases the cross section. A clear scale dependence is seen – the higher the transverse momentum of the jets, the smaller the effect of the variation. At the LHC, for p_T greater then 60 GeV, the uncertainty range is hardly visible on the plot and can be safely neglected. On the other hand, for small p_T values the effect on the cross section is about a factor of 2. Although this is not negligible, it is still smaller than the effect of varying the x' parameter.

To summarise, three sources of theoretical uncertainty for the predictions of exclusive production have been studied: unintegrated gluon distributions, upper and lower Sudakov form factor scales. The dominant one for jet and Higgs boson productions is the lower Sudakov limit. However, one should remember that the results were obtained by varying the scales by an arbitrary factor of 2. This does not need to provide a good estimation of the realistic uncertainties for the LHC production. A more realistic approach is presented in the following.

2.5 Uncertainties at the LHC

In order to estimate realistically the uncertainty on the predictions for LHC energies, the variation of the parameters need to be chosen such that it represents the uncertainty of the CDF measurement. In other words, the model parameters need to be constrained with the CDF data. In turn, the values obtained in such a way will form a basis for further extrapolation of the results to the LHC energies.

The final cross sections are much less sensitive to the x parameter value than to that of the x' parameter. At the LHC the uncertainty on x can be even safely neglected for jets. For Higgs production this effect is exactly zero, since x is fixed by the theory. Therefore, in the following analysis only the x' parameter is considered.

As mentioned before, the default value of the x' parameter is equal to 0.5 and this value was chosen to describe the CDF data for the gluon distribution fit no. 4 (see Figure 2.12). For any other gluon distribution the value of the parameter would be different. Therefore, a proper analysis requires constraining x' independently for each gluon density.

For each gluon distribution, fits $1-4$, two values of the x' parameter are obtained: x'_{min} and x'_{max}. These values follow from the requirement of the compatibility of the calculated cross sections and the CDF measurement. Moreover, the difference between them must follow the uncertainty seen in the CDF data.

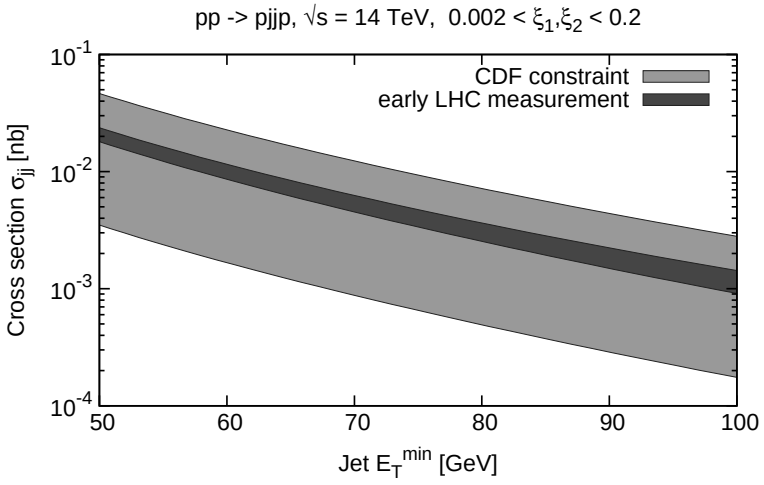

Figure 2.20: Total uncertainty on the CHIDe model from the fit to the CDF measurement (light grey) and possible exclusive jets measurement with a low luminosity of 100 pb^{-1} at the LHC (dark grey).

The obtained results can be used to extrapolate the uncertainty to the LHC energies. For each gluon density the values of x'_{min} and x'_{max} results in an uncertainty of the predictions. In order to take into account both the uncertainty due to gluon density and to the x' parameter, the minimal value of cross section calculated from all gluon densities with a respective x'_{min} value has been computed for each value of the Higgs mass or jet E_T. A similar procedure was carried out for the maximal value

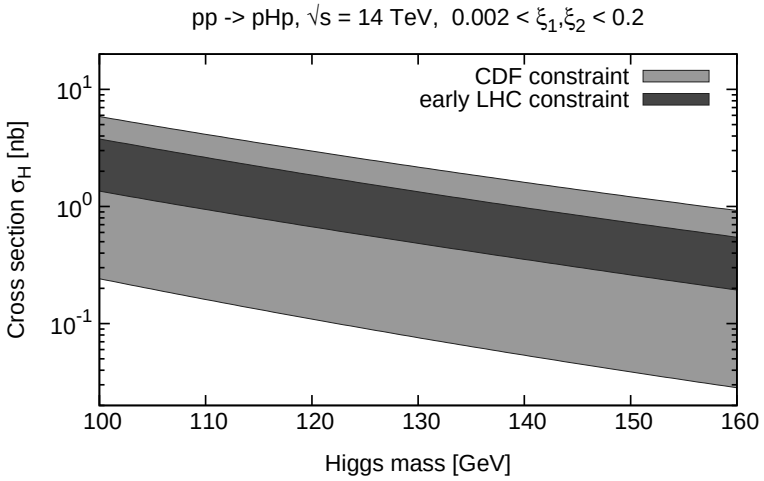

Figure 2.21: Total uncertainty on the CHIDe model for exclusive Higgs production at the LHC: constraint from the fit to the CDF measurement (light grey), constraint from possible early LHC jets measurements with 100 pb^{-1} (dark grey).

of the cross section and x'_{max}. The difference between the obtained cross sections is a measure of the total uncertainty. It is shown in light grey in Figures 2.20 and 2.21 for jets and Higgs, respectively. The obtained uncertainties are large. The values of the predicted cross section differ by a factor of 10 for jets and about a factor of 25 for Higgs production.

The uncertainty on exclusive Higgs production can be greatly reduced with a measurement of exclusive jets at the LHC. Since the cross section for jet production is quite large, a significant constraint on the model can be obtained even with a relatively small integrated luminosity. In this analysis 100 pb^{-1} was assumed. The uncertainty on the measurement is assumed to be statistical and systematic. The systematic uncertainty is assumed to consist of 3% uncertainty on jet energy scale. A number of 3% is a conservative value, which covers also other potential sources of uncertainties. A possible result of such a measurement, obtained with the default CHIDe model parameters, is presented in Fig. 2.20 as a dark area. The estimated uncertainty on the possible measurement is much smaller than that following from the constraint based on the Tevatron data.

To check how such a possible measurement can affect the uncertainty for the Higgs case the same procedure as before was repeated, based on the assumed possible measurement. For each gluon density, a range in x'_{min} and x'_{max} is chosen to describe the exclusive jets measurement at the LHC and its uncertainty. Figure 2.21 presents the extrapolation of these constraints to the Higgs case for $\sqrt{s} = 14$ TeV. One can see that this procedure leads to a considerable reduction of the model uncertainty on the Higgs cross section. Figure 2.22 shows that this uncertainty consists of contributions due to the gluon density and to the value of the x' parameter. It is interesting to notice that the uncertainties due to both mentioned factors are now compatible. Prior to the LHC measurement the effect of the x' uncertainty was much larger, cf.

Figures 2.14 and 2.17. This confirms the importance of the LHC measurement for restricting the uncertainty on the exclusive production.

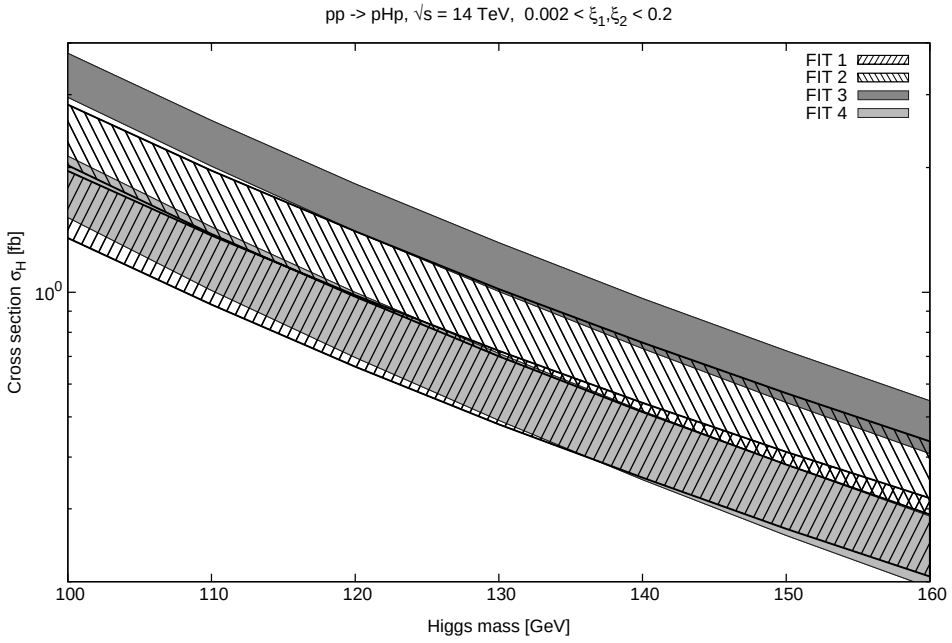

Figure 2.22: Contributions to the total uncertainty on the CHIDe model for exclusive Higgs production at the LHC. For each gluon density (FIT1 – FIT4) the x' uncertainty is shown for a luminosity of 100 fb^{-1}.

Chapter 3

Experimental Apparatus

Diffractive processes discussed in the previous chapters can be studied experimentally. Presently, many of high energy physics experiments are performed at high luminosity particle accelerators. This has a great advantage, since high statistics data can be collected in carefully selected and well controlled conditions. This leads to good reproducibility of the results.

In the following, the LHC accelerator and the ATLAS experiment are introduced and described.

3.1 The Large Hadron Collider

The Large Hadron Collider (LHC) [52] is an accelerator located on the border of France and Switzerland near Geneva. The LHC accelerates two counter-rotating beams of protons or heavy ions and collides them in order to study proton-proton and ion-ion interactions at previously inaccessible energies. The design energy of the proton beams is 7 TeV and has not been reached yet. During the years 2010 and 2011 LHC delivered 3.5 TeV beams. In the year 2012 the energy has been increased to 4 TeV.

The LHC is widely expected to shed light on some of the most important questions of present science. The first one is the possible existence of the last undiscovered particle of the Standard Model – the Higgs boson. This is very important, since the present understanding of mass origin is based on the Higgs field interacting with massive particles. If the Higgs boson exists, it should be discovered at the LHC. In fact, the 2011 ATLAS data [53], shown in Figure 3.1, might suggest the existence of the Higgs particle with mass in the vicinity of 125 GeV. In addition, of 4^{th} of July 2012 both ATLAS and CMS Collaborations reported a discovery of a particle consistent with the Higgs boson [54, 55].

Another unsolved problem regards dark matter, which was introduced to explain

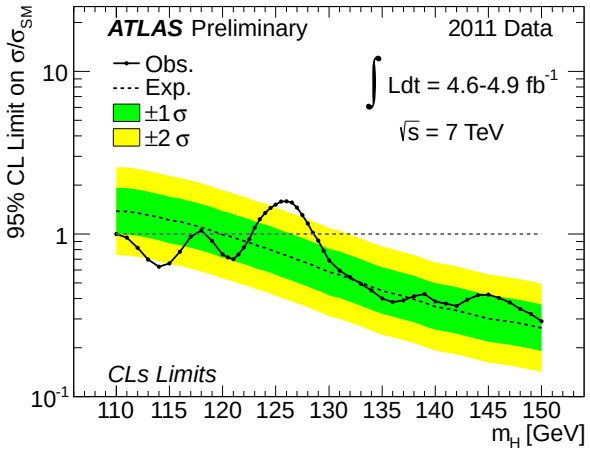

Figure 3.1: Observed (full line) and expected (dashed line) 95% CL combined upper limits on the SM Higgs boson production cross section divided by the Standard Model expectation as a function of m_H in the low mass range. The dotted curves show the median expected limit in the absence of signal and the green and yellow bands indicate the corresponding 68% and 95% CL intervals. [53]

some cosmological data, for example the orbital velocities of stars and galaxies. However, it cannot be explained in terms of presently known particles. Many theories predict new particles to be discovered at the LHC and there is a common hope that a candidate for dark matter will be observed.

One of the most popular theories expected to be confirmed at the LHC is the supersymmetry (SUSY) [56, 57, 58, 59]. It postulates an additional symmetry in the nature – a symmetry between fermions and bosons. It predicts that each presently known particle has a supersymmetric partner with different spin. If confirmed, supersymmetry could also help to construct the quantum description of gravitational interactions.

LHC measurements can also help to understand the asymmetry between matter and anti-matter that is observed in the visible Universe. This is a domain of precise measurements of CP violations in the b-sector.

All the above questions will benefit from the LHC proton-proton programme. The accelerator can also deliver heavy ion beams. So far the ^{208}Pb ions have been used and accelerated to the energy of 1.38 TeV per nucleon. This allows investigation of various phenomena, including the quark-gluon plasma (QGP) created in such collisions. Studies of QGP will help to understand the early phases of the Universe, when the matter was similarly dense and hot.

The LHC accelerator has been installed in a tunnel that previously hosted the Large Electron-Positron (LEP) collider. It is located about 100 metres underground and has about 27 kilometres in circumference. The main elements of the accelerator are 1232 dipole superconducting magnets that can provide magnetic field of 8.3 T.

They are used to keep protons in a circular orbit. There are also 392 quadrupole superconducting magnets that are used to focus the beams. The magnets are kept at a temperature of 1.9 K in order to ensure their superconductivity. This is provided by the world's largest cryogenic setup, which uses approximately 96 tons of liquid helium. In addition, the LHC contains eight radio-frequency (RF) cavities per beam, which accelerate the protons.

The LHC ring is divided into 8 arcs (containing the dipoles) and 8 straight sectors (containing the accelerating cavities and the quadrupoles). Figure 3.2 shows the LHC octants: in the middle of each octant (*Point*) there is a straight sector, the arcs are situated between them. Points 3 and 7 contain the beam cleaning systems, Points 4 the RF cavities and Point 6 the beam dump system. At Points 1, 2, 5 and 8 the two LHC beams cross and protons collide. The collisions are studied by four main experiments: ATLAS, ALICE, CMS and LHCb, respectively.

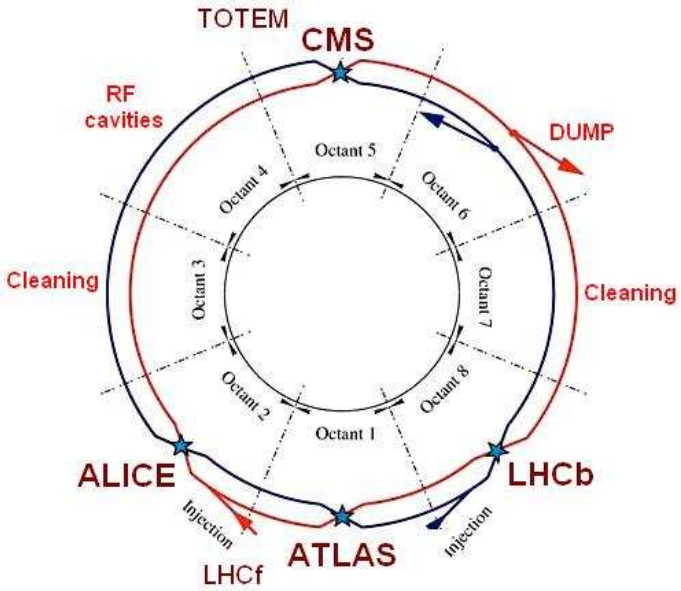

Figure 3.2: General scheme of the LHC accelerator (view from above). Beam 1 rotates clockwise and is drawn in red, beam 2 rotates counterclockwise and is drawn in blue.

The protons collided at the LHC originate from hydrogen atoms, which are stripped off electrons. They are accelerated to the energy of 50 MeV in the LINAC2 accelerator. Next, the protons pass through the whole complex of CERN accelerators (see Figure 3.3): the Proton Synchrotron Booster (PSB), the Proton Synchrotron (PS) and the Super Proton Synchrotron (SPS), where they are accelerated to 1.4 GeV, 25 GeV, 450 GeV, respectively. At the end, the they injected into the LHC ring where they are accelerated to the final energy. It should be mentioned that at the LHC beams are structured into bunches, which are prepared in the PS accelerator.

The LHC has been designed to obtain not only unprecedented energy, but also unprecedented large amount of interactions. The accelerator instantaneous lumi-

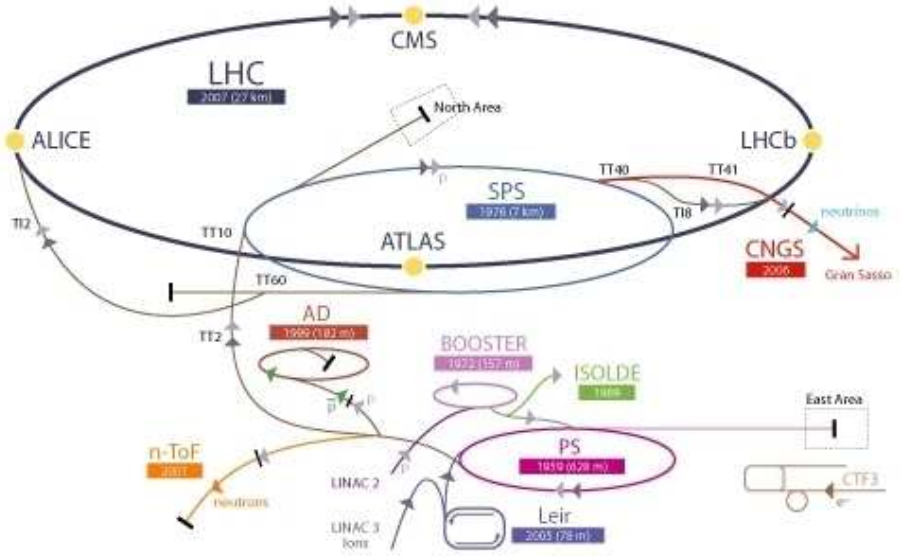

Figure 3.3: The general scheme of the CERN accelerator complex.

nosity depends on various features and can be calculated with the following formula

$$L = \frac{n_p^2 f F}{4\pi\sigma_x\sigma_y}, \tag{3.1}$$

where n_p is the number of protons in each bunch, f is the collision frequency, σ_x and σ_y are the transverse Gaussian beam size widths[1]. F is a geometric factor taking into account a possible angle between the beams (*crossing angle*) and is equal to one for head-on collisions. At the LHC, the transverse beam sizes are equal at the interaction point:

$$\sigma_x = \sigma_y = \sigma.$$

To describe the beam properties, one often uses the transverse emittance ϵ and the amplitude function β. The first reflects the quality of the beam and is fixed already at the very early stages of the beam preparation[2]. The β function describes the accelerator optics. The following formula is valid:

$$\epsilon\beta^* = \pi\sigma^2, \tag{3.2}$$

where β^* denotes the value of the β function at the IP. It should be noted that the transverse size of the beam changes along the accelerator ring due to the presence of the magnets. Also, the horizontal and vertical sizes are usually different. In order to describe this changes β_x and β_y functions are defined along the ring.

[1]The LHC coordinate system takes the x axis horizontal and pointing towards the ring centre, y axis points upwards and s (sometimes z) is a curvilinear coordinate along the nominal orbit.

[2]The emittance slightly grows with time due to interaction between protons in a bunch, between bunches, and due to B field imperfections.

The frequency of the LHC is 40 MHz and there can be 3564 bunches stored along the ring. However, a part of them are reserved for beam injection and dump purposes. Also, some bunches do not have a partner in the other beam (*pilot bunches*) and are used for background studies. Eventually, 2808 proton bunches per beam can be used for *pp* collisions. It is worth mentioning that the LHC can work with various bunch configurations, ranging from a single bunch per beam up to the maximum value of 2808.

At the nominal conditions each bunch contains about 10^{11} protons and its length is of the order of 75 mm (Gaussian width). The transverse size at Point 1 is about 16 μm in both horizontal and vertical directions.

The design LHC luminosity is $2 \cdot 10^{34}$ cm^{-2}s^{-1}. This will lead to very large statistics of interesting, rare events that can be collected. However, there are disadvantages of such a high luminosity. The first one, connected to the large frequency of the collisions, is the necessity of very large event rejection by the trigger, see Section 3.3. Also, due to the very small time interval between the collisions, the particles produced in one collision do not have time to cross the whole detectors before the next collision occurs. This leads to special requirements on the detectors, which must be able to separate such signals. The other problem is *pile-up*, *i.e.* multiple proton-proton collisions occurring during one event[3]. The pile-up multiplicity can be quite large, the nominal conditions assume an average *pp* interaction multiplicity $\mu = 46$. However, even larger values are sometimes considered.

In order to study the collisions delivered by the LHC accelerator, detectors must be able to register particles produced in the occurring interactions. It is very difficult to build a detector that is capable of studying all possible aspects of the collisions and therefore at the LHC there are 7 different experiments. In addition, it is very important to confirm the obtained results by independent groups. Thus, at the LHC there are two general-purpose detectors, ATLAS (A Toroidal LHC Apparatus) [60] and CMS (Compact Muon Solenoid) [61], with similar physics potential but different designs and technologies. These detectors are intended to provide the best possible angular coverage of the solid angle around the interaction region in order to register as many produced particles as possible. They focus on studying high-p_T signals, which can be used for *new physics* searches as well as to constrain present models.

The ALICE (A Large Ion Collider Experiment) [62] experiment is dedicated to studies of heavy ions collisions. It allows precise studies of charged particles produced in collisions with small transverse momentum. In addition, it provides a possibility of particle (hadron) identification. On the other hand the angular coverage is not as good as for ATLAS or CMS. However, for heavy ion studies it is not crucial, since usually global characteristics in central rapidities are measured.

[3]The events are understood as all the interactions that occur during the crossing of one bunch through another.

The main aim of the LHCb (LHC beauty) [63] experiment is to study the CP violation in the B-mesons decay. The LHCb detector consists of a asymmetric forward spectrometer. It covers the forward pseudorapidity region and is capable of measurements at smaller angles than the ATLAS, CMS or ALICE detectors. Such a design is sufficient for the LHCb programme, since the B-meson pairs are produced mainly in the forward direction. Also, the cross section for the production is relatively high and the direction of the two produced mesons is highly correlated.

Besides the four main experiments described above, there are three smaller ones: TOTEM [64], LHCf [65] and MoEDAL [66]. Since there are only four beam intersection regions, the small experiments need to share them with the main ones. The TOTEM (TOTal Elastic and diffractive cross section Measurement) detectors share Point 5 with the CMS experiment and provide a coverage of the very forward rapidity region. In addition, they can detect protons that are produced at very small angles. The LHCf (LHC forward) shares Point 1 with the ATLAS experiment and is located 140 metres from the interaction region on both sides. It measures the multiplicity and the energy of neutral pions produced in the forward direction, close to zero degree. Its results will allow a better understanding of the ultrahigh-energy cosmic rays. Finally, the MoEDAL (Monopole and Exotics Detector At the LHC) experiment shares Point 8 with LHCb and searches for highly ionising particles, in particular magnetic monopoles or dyons[4].

The LHC experiments produce enormous amounts of data, both recorded events as well as Monte Carlo generated ones. Their storage and processing is possible due to the *LHC Computing Grid (LCG)* [67]. Grid is a world-wide network of storage and computing clusters and its purpose is to process easily requested data without transferring them to local computers. Each Grid centre stores some part of the data and makes it available together with computing resources. A Grid user can access the data by sending a job that will process them producing results, which can be downloaded locally.

3.2 The ATLAS Detector

ATLAS [60] is one of the four main experiments measuring collisions at the LHC. It uses a general-purpose detector designed to measure a variety of different processes, focussing on high-p_T signals.

The general structure of the ATLAS detector is typical for such detectors, see Figure 3.4. The detector has a central, cylindrical part (*the barrel*) surrounding the interaction region, which is "closed" on both sides by *end-caps*. Such design provides good measurement capabilities in the central region and good coverage in the forward regions. Figure 3.4 shows also the layered structure of both barrel and

[4]Magnetic monopoles are particles with magnetic charge. Dyons are similar to monopoles, but have also electric charge. Both types of particles are yet undiscovered.

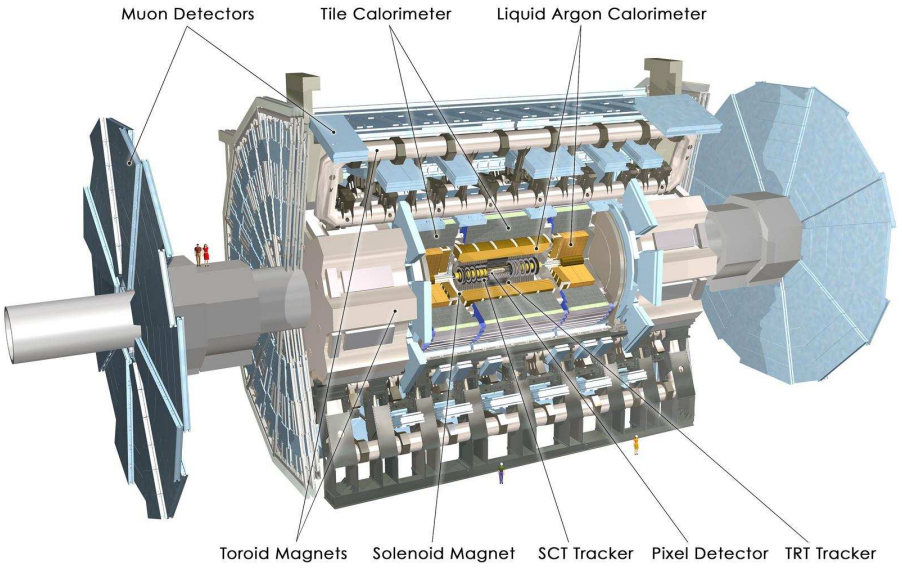

Figure 3.4: General scheme of the ATLAS main detector.

end-caps, which allows precise measurements of particles produced in the interaction. The consecutive sub-detectors crossed by these particles are: the inner detector, the calorimeters and the muon spectrometer.

The purpose of the inner detector [68, 69, 70] is to register the trajectories (tracks) of the produced charged particles. The inner detector is surrounded by a magnet providing a solenoidal magnetic field of 2 T. This provides a possibility to determine the momenta and charge signs of the charged particles by measuring the curvature of their trajectories. This is the most important purpose of the inner detector. In addition, positions of the interaction vertices can be reconstructed from the measured tracks. This is needed in order to deal with high pile-up environment. Also, the *secondary* vertices (decay points of particles) can be reconstructed. This is used for example for b-jet identification.

Similarly to the whole ATLAS detector, the inner detector has also a layered structure and consists of three sub-detector systems of different technology, see Figure 3.5. The innermost layer is the Pixel detector, located just around the LHC beam pipe. This sub-detector consists of three layers of silicon pixel detectors, both in the barrel and the end-caps. The consecutive barrel layers are placed at $R = 50.5$, 88.5 and 122.5 mm (R is a distance from the beam axis) and span $|z| < 400.5$ mm. The end-cap layers are located at $z = \pm 495$, 580 and 650 mm and span 88.8 mm $< R <$ 149.6 mm. The pixel detector provides the highest spatial resolution of all the ATLAS sub-detectors. In the barrel the resolution is 10 μm in $R\phi$ (ϕ is the azimuthal angle) and 115 μm in z, while in the end-caps it is 10 μm in $R\phi$ and 115 μm in R. This is needed to precisely reconstruct the tracks in the region close to the interaction point and, in consequence, the vertices.

The second sub-detector is the SemiConductor Tracker (SCT), located around

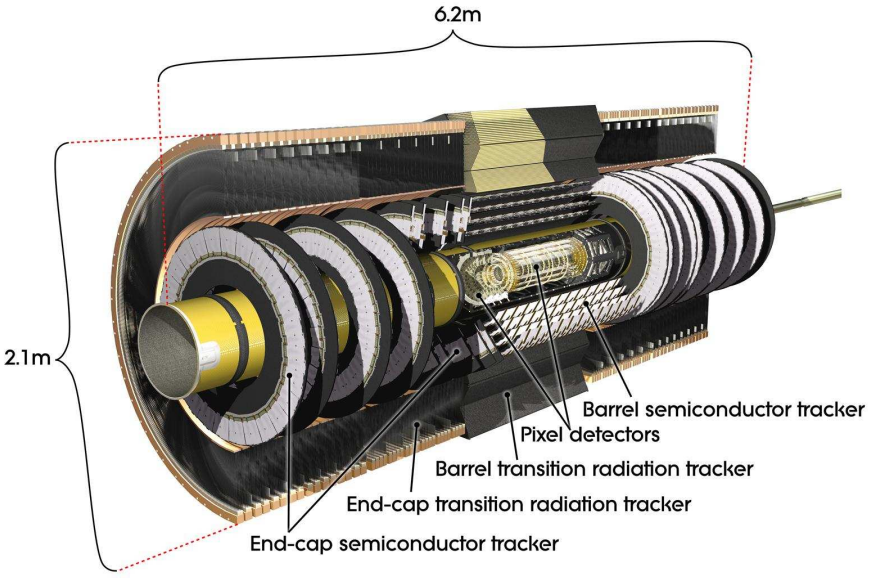

Figure 3.5: General scheme of the ATLAS inner detector.

the Pixel detector and built of silicon micro-strips. A signal from a strip does not provide information about the position along the strip. In order to reconstruct all the coordinates of the hit created by a traversing particle, micro-strip modules are arranged in pairs that are rotated by 40 mrad with respect to each other. The combined information allows reconstruction of the position along the strips. The SCT consists of 4 layers in the barrel and 9 layers in the end-caps. In the barrel the layers are placed at $R = 299$, 371, 443 and 514 mm and they span $|z| < 749$ mm. The end-cap layers are at $z = \pm 853.8$, 934, 1091.5, 1299.9, 1399.7, 1771.4, 2115.2, 2505 and 2720.2 mm. The R range spanned by the SCT end-cap varies from layer to layer. The upper limit is always 560 mm, while the lower limit equals 337.6 mm for the first and seventh layer, 275 mm for layers 2 – 5, 408 mm for the eighth layer and 438.8 for the ninth one. SCT provides a resolution of 17 μm in $R\phi$ and 580 μm in z/R in barrel/end-caps layers, respectively.

The outermost part of the inner detector is the Transition Radiation Tracker (TRT). It is build of "straw" tubes filled with gas. The conductive coating of a straw is the cathode, while the thin wire in the centre is the anode. Charged particles traversing a straw ionise the gas. This leads to a signal collected by the anode. In addition, consecutive layers of straws are separated by foil. Charged particles crossing the foil produce the transition radiation, which enhances the signal produced by the particle itself. The amount of transition radiation depends on the Lorentz γ factor of the particle and can be used to distinguish electrons from pions, kaons and other heavier particles. The barrel part of TRT spans the region of $|z| < 712$ mm and 563 mm $< R <$ 1066 mm, while its end-cap part 848 mm $< |z| <$ 2710 mm and 644 mm $< R <$ 1004 mm. The accuracy of the TRT is 130 μm in $R\phi$.

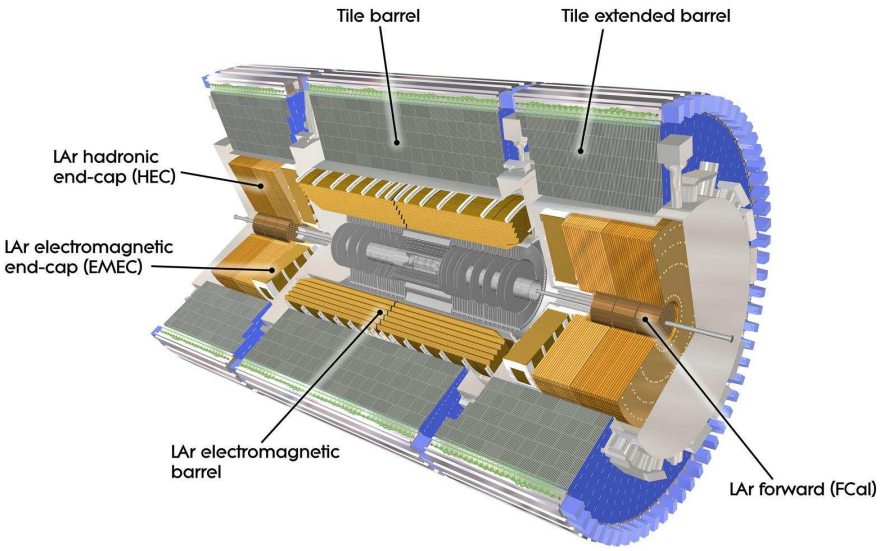

Figure 3.6: General scheme of the ATLAS calorimetry system.

The calorimeters are located around the inner detector and the solenoid magnet. Their purpose is to measure the energy of produced particles. They can detect photons and neutral hadrons, which do not leave hits in the inner detector. In addition, the calorimeters are very important for distinguishing electrons and photons from hadrons. The ATLAS calorimetry system [71, 72] is presented in Figure 3.6 and consists of the liquid argon (LAr) electromagnetic calorimeter (barrel + end-cap), the LAr hadronic end-caps, the tile calorimeter and the LAr forward calorimeter (FCal). The LAr electromagnetic calorimeters, as well as the first layer of FCal, are designed to measure the energy of electrons and photons by sampling the electromagnetic cascades that they initiate. The total thickness of the electromagnetic calorimeters is greater than 22 radiation lengths in the barrel and 24 radiation lengths in the end-caps. This ensures that the energy leakage of the electromagnetic cascades out of the electromagnetic calorimeter is very small.

The electromagnetic calorimeters are surrounded by the hadronic calorimetry system, which is meant to measure the energy of hadrons. Hadrons are much heavier than electrons and their electromagnetic interactions with matter are much weaker. On the other hand, they interact strongly with atomic nuclei. This leads to hadronic cascades, which need much more material to develop. Hence the need of additional, more dense, detectors. In the LAr calorimeters, liquid argon is used as the active medium, where the measurement is performed by collecting electrons originating from ionisation process. Lead, copper or tungsten layers (in different parts) are the main absorbers where the cascades evolve. The tile calorimeter is built of scintillating tiles as the active medium and steel layers as the absorber. The thickness of the whole calorimetry system is about 9.7 interaction lengths in the barrel and 10

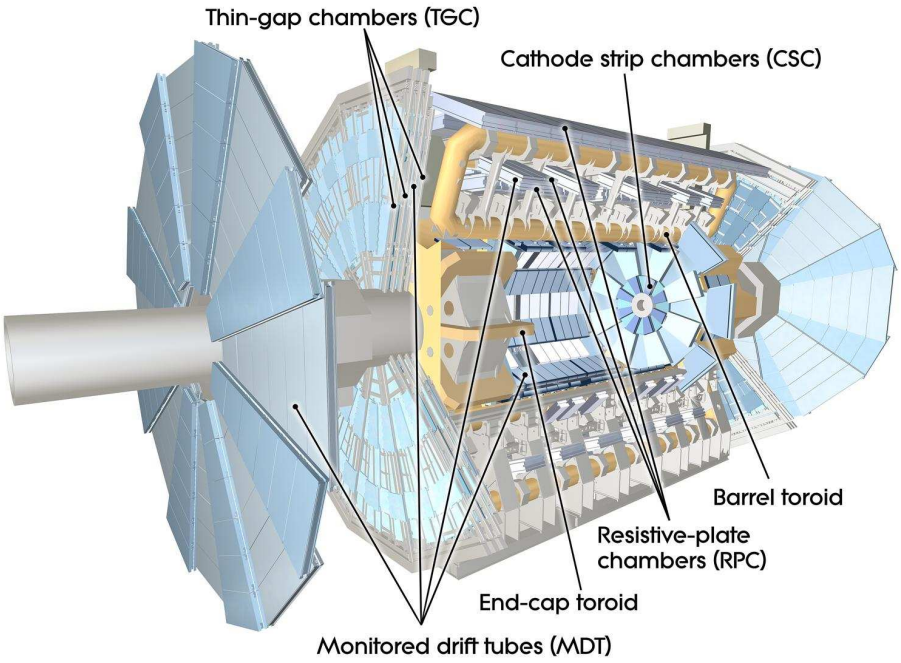

Figure 3.7: The general scheme of the ATLAS muon spectrometer.

interaction lengths in the end-caps.

The outermost layer of the ATLAS detector is the Muon Spectrometer [73]. Muons are relatively heavy particles and do not interact strongly. Therefore, usually they are not stopped in the calorimeters like other particles. The Muon Spectrometer provides the identification of muons and it allows muon momentum determination by measuring its trajectory in the magnetic field. The detector consists of four subsystems: the Monitored Drift Tubes (MDT), the Cathode Strip Chambers (CSC), the Resistive Plate Chambers (RPC) and the Thin Gap Chambers (TGC), as presented in Figure 3.7. The MDTs and the SCTs are used for position measurements, while the RPCs and the TGCs are used for triggering purposes. The barrel part of the Muon Spectrometer consists of RPSs and MDTs, the end-caps contain the CSCs, the TGSs and the MDTs. The magnetic field used for muon momentum measurements is provided by three superconducting toroid magnets, one in the barrel part and two in the end-caps.

The overall measurements capabilities of the ATLAS detector are the following:

- the reconstruction of charged particle tracks is possible up to $|\eta| < 2.5$,
- muon detection can be performed in a slightly larger range, limited to $|\eta| < 2.7$.
- the largest coverage is provided for calorimetric measurements, which are possible up to $|\eta| < 4.9$.

In addition, there are detectors dedicated to special measurements in the forward directions. The first one is LUCID (LUminosity measurement using Cherenkov In-

Table 3.1: Main parameters of the calorimeter system. From [60]

	Barrel		End-cap	
EM calorimeter				
Number of layers and $\|\eta\|$ coverage				
Presampler	1	$\|\eta\| < 1.52$	1	$1.5 < \|\eta\| < 1.8$
Calorimeter	3	$\|\eta\| < 1.35$	2	$1.375 < \|\eta\| < 1.5$
	2	$1.35 < \|\eta\| < 1.475$	3	$1.5 < \|\eta\| < 2.5$
			2	$2.5 < \|\eta\| < 3.2$
Granularity $\Delta\eta \times \Delta\varphi$ versus $\|\eta\|$				
Presampler	0.025×0.1	$\|\eta\| < 1.52$	0.025×0.1	$1.5 < \|\eta\| < 1.8$
Calorimeter 1st layer	$0.025/8 \times 0.1$	$\|\eta\| < 1.40$	0.050×0.1	$1.375 < \|\eta\| < 1.425$
	0.025×0.025	$1.40 < \|\eta\| < 1.475$	0.025×0.1	$1.425 < \|\eta\| < 1.5$
			$0.025/8 \times 0.1$	$1.5 < \|\eta\| < 1.8$
			$0.025/6 \times 0.1$	$1.8 < \|\eta\| < 2.0$
			$0.025/4 \times 0.1$	$2.0 < \|\eta\| < 2.4$
			0.025×0.1	$2.4 < \|\eta\| < 2.5$
			0.1×0.1	$2.5 < \|\eta\| < 3.2$
Calorimeter 2nd layer	0.025×0.025	$\|\eta\| < 1.40$	0.050×0.025	$1.375 < \|\eta\| < 1.425$
	0.075×0.025	$1.40 < \|\eta\| < 1.475$	0.025×0.025	$1.425 < \|\eta\| < 2.5$
			0.1×0.1	$2.5 < \|\eta\| < 3.2$
Calorimeter 3rd layer	0.050×0.025	$\|\eta\| < 1.35$	0.050×0.025	$1.5 < \|\eta\| < 2.5$
Number of readout channels				
Presampler	7808		1536 (both sides)	
Calorimeter	101760		62208 (both sides)	
LAr hadronic end-cap				
$\|\eta\|$ coverage			$1.5 < \|\eta\| < 3.2$	
Number of layers			4	
Granularity $\Delta\eta \times \Delta\varphi$			0.1×0.1	$1.5 < \|\eta\| < 2.5$
			0.2×0.2	$2.5 < \|\eta\| < 3.2$
Readout channels			5632 (both sides)	
LAr forward calorimeter				
$\|\eta\|$ coverage			$3.1 < \|\eta\| < 4.9$	
Number of layers			3	
Granularity $\Delta x \times \Delta y$ (cm)			FCal1: 3.0×2.6	$3.15 < \|\eta\| < 4.30$
			FCal1: $\sim$ four times finer	$3.10 < \|\eta\| < 3.15$,
				$4.30 < \|\eta\| < 4.83$
			FCal2: 3.3×4.2	$3.24 < \|\eta\| < 4.50$
			FCal2: $\sim$ four times finer	$3.20 < \|\eta\| < 3.24$,
				$4.50 < \|\eta\| < 4.81$
			FCal3: 5.4×4.7	$3.32 < \|\eta\| < 4.60$
			FCal3: $\sim$ four times finer	$3.29 < \|\eta\| < 3.32$,
				$4.60 < \|\eta\| < 4.75$
Readout channels			3524 (both sides)	
Scintillator tile calorimeter				
	Barrel		Extended barrel	
$\|\eta\|$ coverage	$\|\eta\| < 1.0$		$0.8 < \|\eta\| < 1.7$	
Number of layers	3		3	
Granularity $\Delta\eta \times \Delta\varphi$	0.1×0.1		0.1×0.1	
Last layer	0.2×0.1		0.2×0.1	
Readout channels	5760		4092 (both sides)	

Table 3.2: Main parameters of the Muon Spectrometer. From [60]

Monitored drift tubes	MDT
- Coverage	$\|\eta\| < 2.7$ (innermost layer: $\|\eta\| < 2.0$)
- Number of chambers	1088 (1150)
- Number of channels	339 000 (354 000)
- Function	Precision tracking
Cathode strip chambers	CSC
- Coverage	$2.0 < \|\eta\| < 2.7$
- Number of chambers	32
- Number of channels	31 000
- Function	Precision tracking
Resistive plate chambers	RPC
- Coverage	$\|\eta\| < 1.05$
- Number of chambers	544 (606)
- Number of channels	359 000 (373 000)
- Function	Triggering, second coordinate
Thin gap chambers	TGC
- Coverage	$1.05 < \|\eta\| < 2.7$ (2.4 for triggering)
- Number of chambers	3588
- Number of channels	318 000
- Function	Triggering, second coordinate

tegrating Detector). It is dedicated to relative luminosity measurement by recording charged particle multiplicities in $5.4 < |\eta| < 6.1$. The second one is the Zero Degree Calorimeter (ZDC). It is capable of measuring the energy of neutral particles produced with $|\eta| > 8.3$. It is used mainly in heavy ion runs.

The last ATLAS forward detector is ALFA (Absolute Luminosity For ATLAS) [74]. Its aim is to detect protons scattered elastically into the beam pipe. However, they also allow measurements of protons scattered diffractively. ALFA is dedicated to measurements of the elastic scattering processes, which can be used to determine the total cross section. This, in turn, can lead to absolute measurement of luminosity and calibration of the relative luminosity detectors, *e.g.* LUCID.

The ALFA detectors consist of four stations located at 237.4 and 241.5 metres from the ATLAS interaction point, symmetrically on both sides. At such a large distance, even protons that were scattered with very small transverse momenta are far enough from the beam so that they can be safely measured. However, because of the LHC magnets that protons traverse before reaching the ALFA position, the vertical deflection caused by the vertical component of the transverse momentum is greater than the horizontal one. In order to detect protons with the smallest possible transverse momenta, the detectors need to be placed close to the proton beam. This is done by means of the *Roman Pot* devices that insert the ALFA

detectors close to the LHC beam from below and above. The vertical direction of the detectors insertion is favourable with respect to the horizontal one due to the better sensitivity to the vertical momentum. This leads both to better resolution of the measurement as well as a better lower limit of the momentum acceptance.

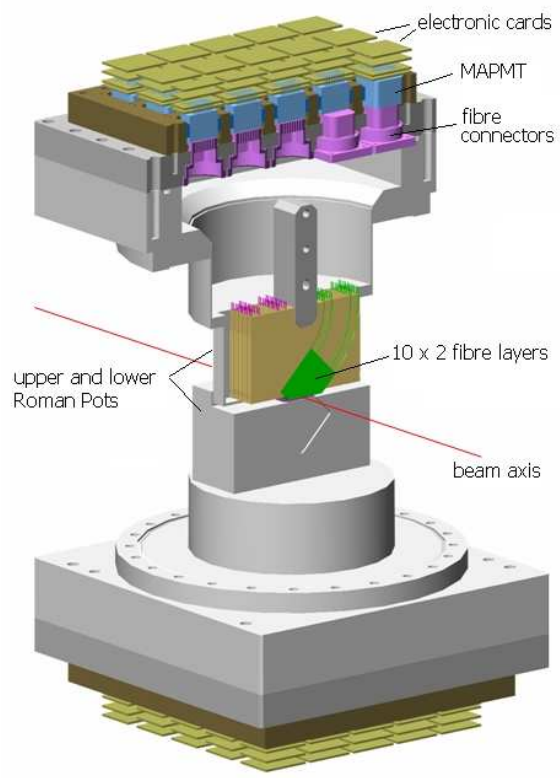

Figure 3.8: General scheme of an ALFA detector (one station).

A sketch of the ALFA detector is presented in Figure 3.8. It shows two Roman Pots approaching the beam from above and from below. Each pot contains a detector that can measure the positions of traversing protons. Such detector consists of 20 layers, each consisting of 64 parallel scintillating fibres. Fibres in consecutive layers are rotated by 90 degrees around the axis perpendicular to the layer (UV geometry). This allows determination of the scattered trajectory position in the transverse plane. Signals from fibres are read out by photomultipliers located on top/bottom of the pot.

In order to measure very small transverse momenta, the ALFA detectors need special settings of the LHC beams. This is because the transverse momentum corresponding to the angular spread of the beam must be smaller than the momentum that one wants to measure. Otherwise, the scattered protons could not be distinguished from the protons of the beam. This requires an LHC optics with large β^* value. The nominal β^* value for the ALFA runs is 2625 m. However, for 2011 runs an intermediate optics was used with $\beta^* = 90$ m, which is still much larger than the standard LHC value of 0.55 m.

Figure 3.9 presents the acceptance of the ALFA detectors as a function of the proton transverse momentum p_T and its energy loss ΔE. Two plots are presented for both mentioned dedicated LHC optics settings. It should be pointed out that for elastic scattering $\Delta E = 0$, while for diffractive interactions $\Delta E > 0$. One can see that the $\beta^* = 2625$ m optics provides a better acceptance for small values of p_T (below 0.15 GeV) and a smaller one for larger values (above 0.2 GeV). For $\Delta E > 0$, both settings allow to measure with good acceptance up to 600 GeV.

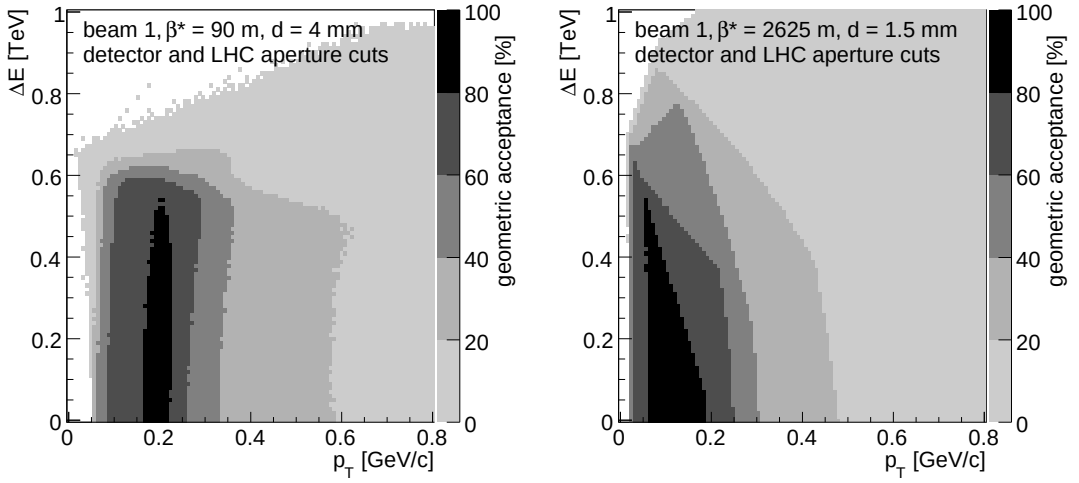

Figure 3.9: Geometrical acceptance of the ALFA detector as a function of the proton energy loss (ΔE) and transverse momentum (p_T) for two LHC settings – $\beta^* = 90$ m (left) and $\beta^* = 2625$ m (right). The distance between the beam centre and the detector edge was set to the expected values of 4 mm and 1.5 mm, respectively.

3.3 ATLAS Trigger

The ATLAS data acquisition system [75, 76] allows to store the collected data at the maximal rate of about 300 Hz. This is mainly due to the large amount of information provided by the ATLAS detector – the typical compressed event size is of the order of 1.5 MB. The ATLAS trigger system analyses the registered events in real time and decides which ones are interesting and worth storing for further analysis. Since the interesting processes are very rare, the approach of having a very high rate of events and rejecting the great majority of them works well.

The trigger system is made of 3 levels: the Level 1 trigger (L1), the Level 2 trigger (L2) and the Event Filter (EF). Each one either accepts the event and passes it further or rejects it. The reason behind this is that the information from different detector systems is not available equally fast, *i.e.* it is possible to reject some events based on partial information, even before the rest is read-out. Also, the algorithms at each step are more complicated than at the previous one and the number of events that can be processed in parallel is smaller.

The L1 trigger is hardware based and makes use of the reduced information coming from the calorimeters and the muon spectrometer. The decision is taken in 2.5 μs and is based on a simplified reconstruction of muons, electrons, photons and jets with high transverse momentum, high missing transverse energy and high total energy. Technically, L1 defines the Regions of Interest (RoIs), containing the position, type and energy of the observed objects. The final decision is taken based on the combined information from all the RoIs and the accepted output event rate at L1 is limited to 75 kHz.

The L2 trigger accesses detailed information from the detector, but only in the vicinity of the RoIs provided by L1. It reduces the output rate to 3.5 kHz and its latency (decision time) is about 40 ms. The Event Filter is the last step of the triggering system. All detector information is available and it takes about 4 seconds to decide whether to keep an event or not. Both L2 and EF are software based triggers and use a dedicated computer farm.

3.4 Data Processing

The events accepted by the EF trigger are stored and processed with the ATLAS reconstruction software [77], which aims at reconstructing the properties of the physical objects produced in the interaction from the information provided by the detector (raw data). A typical analysis does not use directly the information from the detector, but rather the reconstructed objects. These are charged leptons (electrons, muons and τ's), photons, jets and neutrinos, via the missing transverse energy. There are also "lower level" objects, the most important ones being tracks, which represent the trajectories of charged particles. Tracks are reconstructed from hits left by the particles in the tracking detectors. The reconstruction takes into account the magnetic field and the particle interactions with the detector, which decrease the energy and can alter the trajectory. Other objects of this type are clusters, which represent calorimeter energy deposits, and primary vertices, which represent separate interactions occurring in the same bunch crossing.

The electron or photon reconstruction starts with an energy cluster in the electromagnetic calorimeter. The lateral and longitudinal shape of the energy deposit must be consistent with an electromagnetic shower. In addition, it is checked whether the energy leaked into the hadronic calorimeter is small. In order to distinguish between photon and electron induced showers, one searches for the existence of a charged particle track matching the shower position. If such a track is found the object can be reconstructed as an electron, otherwise it is treated as a photon. Several more properties are checked, for example the TRT response or the energy to momentum ratio. For photons, two other possibilities are examined: first a cluster with a matching track comes from a photon conversion, second a track-less energy deposition is due to a π^0 decaying into photon pairs.

The muon reconstruction is based on the information from the muon spectrometer, since it is very unlikely that other particles would give signal there. Track information from the inner detector can also be used to improve the momentum measurement resolution. An expected value of the energy loss for the muon traversing the calorimeters is taken into account in order to combine these two tracks.

In addition, reconstructed electrons and muons are processed through identification algorithms in order to reject the remaining background. There are three kinds of such algorithms: *loose*, *medium* and *tight*. Each consecutive one ensures a better purity of the resulting sample, at the cost of rejecting also a part of the signal. They take into account more subtle effects and are tuned using Monte Carlo events or recorded data.

The jet reconstruction is purely calorimeter based and uses *topological clusters*. The cluster reconstruction starts with a calorimeter cell that shows a substantial energy deposit. The actual requirement is that the measured cell signal has to be at least four standard deviations of the noise above the average noise in the cell. This is to ensure that the deposit is not due to a fluctuation. Such a cell is called the cluster seed and all the neighbouring cells are added to the cluster. If one of the added cells has the energy deposit greater than two standard deviations above the average noise, it becomes a secondary seed, for which the procedure is repeated. The clusters obtained in such a way are then merged into jets with the *anti-k_T algorithm* [78]. The algorithm is both infrared and collinear safe and results in cone-like jet shapes.

The τ-leptons decay very quickly and cannot be directly detected. Taus can decay leptonically or hadronically. In the first case they decay into electron or muon, neutrino and anti-neutrino. Unfortunately, it is very difficult to distinguish such events from a direct electron or muon production (*i.e.* not from the τ decay). Therefore, the τ reconstruction is performed only for the hadronic decay channel. It exploits the fact that τ-jets[5] have always either one or three tracks and the width of the energy deposit is smaller than in jets. Additional identification can be performed based on more detailed information about the tracks and shapes of the energy deposits in the calorimeters.

The missing transverse energy (MET, E_T^{miss}) is an indirect way to measure neutrinos produced in the event. It is based on the momentum conservation, particularly the momentum components transverse to the direction of the colliding beams. The transverse momenta of both protons before the interaction are close to zero, and the sum of the transverse momenta of all the final state particles must be the same. Since the produced neutrinos are not detected, the sum of momenta of all observed particles must give the momentum opposite to the sum of momenta of all neutrinos. Naturally, some particles are not detected due to the limited acceptance of

[5]Hadronically decaying τ's look very similar to jets. However they are not jets, in the sense that they to not originate from direct hadronisation of single quarks or gluons.

the detector in the forward region. However, for the interesting high-p_T events, the transverse momentum of such particles is usually very small compared to the p_T of the produced neutrino(s). On the other hand, the longitudinal momentum of such particles is not negligible. That is why one cannot obtain the information about the longitudinal momentum of the neutrino(s). In the ATLAS experiment, the missing transverse energy is reconstructed as a vector sum of the transverse energies of the reconstructed electrons, photons, muons, τ's, jets and clusters not associated to any of these objects.

Chapter 4

Diffractive Measurements with ALFA Detectors

UNDOUBTEDLY, the best way of measuring diffractive interactions is via a direct observation of the scattered intact protons. In a collider experiment it is a difficult task, since such protons are scattered at very small angles, and requires dedicated detectors. In the ATLAS experiment such possibility is provided by the ALFA detectors described in the previous chapter.

The main ALFA physics programme is the measurement of elastic scattering. In addition, studies of soft single diffractive dissociation are planned. Unfortunately, due to the fact that ALFA detectors are used only during dedicated runs with low instantaneous luminosity, the possible measurements are limited to processes characterised by very large cross sections. One possibility, which has not been considered before, is the soft exclusive production, in particular the non-resonant $pp \to p\pi^+\pi^- p$ process.

The $pp \to p\pi^+\pi^- p$ process was measured at the CERN ISR collider for $\sqrt{s} =$ 62 GeV [79, 80] and $\sqrt{s} = 63$ GeV [81]. Its measurements at higher energy can provide a deeper understanding of the diffractive reaction mechanism. This process is an important background for exclusive production of resonances decaying into pions, such as: $f_2(1270)$, glueball candidates (*e.g.* $f_0(1500)$) or charmonia (*e.g.* $\chi_c(0)$). The possibility of the $pp \to p\pi^+\pi^- p$ measurement in the ATLAS experiment with the ALFA detectors used for proton tagging is discussed below, following the lines of [82].

The plan of the chapter is as follows. At the beginning, the theoretical description of the process is presented and briefly described. Then, the basic idea of the mea-

surement and the most important properties of the detectors are discussed. Finally, the results of the simulation are presented, taking into account the experimental environment.

The work presented in this chapter was partially published in ISRN High Energy Physics, vol. 2012, Article ID 491460 and Acta Phys. Polon. B42 (2011) 1861-1870.

4.1 Theoretical Model

This study is based on the theoretical calculations of the exclusive $\pi^+\pi^-$ production described earlier in [20, 83]. Only the main aspects of the calculations are presented below.

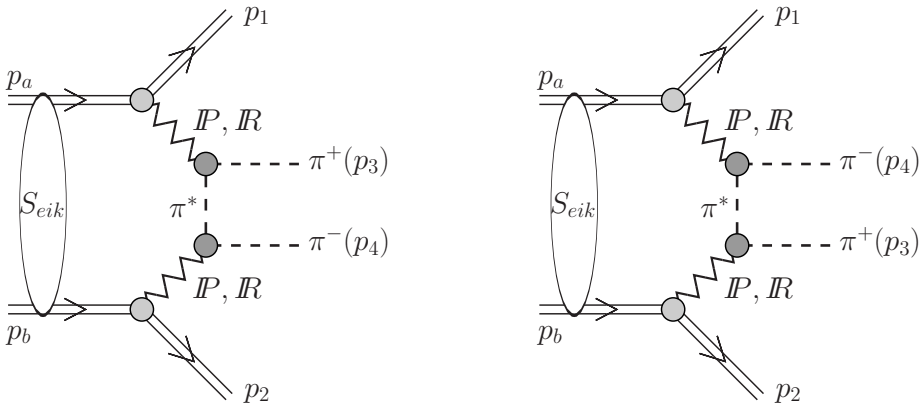

Figure 4.1: Double-diffractive mechanism of exclusive production of $\pi^+\pi^-$ pairs including absorptive corrections.

The assumed mechanism of the process is based on Regge exchanges between interacting particles and is presented in Figure 4.1. The naming convention is the following: a and b denote the incoming protons, 1 and 2 the outgoing ones, while 3 and 4 the produced π^+ and π^-, respectively. The additional virtual pion necessary to produce a pair of pions is denoted with π^*

In order to account for the possibility of additional interactions between the protons (indicated in Figure 4.1 with blobs), the amplitude for the process consists of the bare amplitude and the rescattering amplitude:

$$\mathcal{M}^{full} = \mathcal{M}^{bare} + \mathcal{M}^{rescatt} . \tag{4.1}$$

The bare amplitude is given by the formula:

$$\begin{aligned} \mathcal{M}^{bare} &= M_{13}(s_{13}, t_1) F_\pi(t_a) \frac{1}{t_a - m_\pi^2} F_\pi(t_a) M_{24}(s_{24}, t_2) \\ &+ M_{14}(s_{14}, t_1) F_\pi(t_b) \frac{1}{t_b - m_\pi^2} F_\pi(t_b) M_{23}(s_{23}, t_2) , \end{aligned} \tag{4.2}$$

where M_{ij} are the couplings between particles i and j, $F_\pi(t)$ are the form factors

and $1/(t - m_\pi^2)$ terms are the pion propagators. The form factors correct for the off-shellness of the virtual pions and the following parametrisation is assumed:

$$F_\pi(t) = \exp\left(\frac{t - m_\pi^2}{\Lambda_{off}^2}\right), \tag{4.3}$$

where $\Lambda_{off}^2 = 2$ GeV^2 was obtained from a fit to the ISR data [83]. It should be mentioned that the exact shape of the form factor is rather poorly known in the non-perturbative domain and measurements at higher energies can help to constrain it.

The energy dependence of the πp elastic amplitudes is parametrised in terms of Regge theory [1] by Pomeron and Reggeon exchanges. The coupling values and the Regge trajectory parameters are taken from the Donnachie-Landshoff analysis of the total and elastic cross sections for πN scattering [84]. The slope parameters of the elastic πp scattering are taken as

$$B(s) = B_i + 2\alpha_i' \ln\left(\frac{s}{s_0}\right), \tag{4.4}$$

where $B_{I\!P} = 5.5$ GeV^{-2}, $\alpha'_{I\!P} = 0.25$ GeV^{-2} and $B_{I\!R} = 4$ GeV^{-2}, $\alpha'_{I\!R} = 0.93$ GeV^{-2}, for Pomeron and Reggeon exchanges, respectively and $s_0 = 1$ GeV^2.

In the low mass region where D-L parametrisation is not valid, an additional correction factor is introduced [20]. It allows a smooth behaviour of M_{ij} terms for πp subsystem masses below 2 – 3 GeV.

The absorptive corrections to the bare amplitude are taken into account as:

$$\mathcal{M}^{rescat} = \mathrm{i} \int \frac{d^2\mathbf{k}_t}{2(2\pi)^2} \frac{A_{pp}(s, k_t^2)}{s} \mathcal{M}^{bare}(\boldsymbol{p}_{a,t}^* - \boldsymbol{p}_{1,t}, \boldsymbol{p}_{b,t}^* - \boldsymbol{p}_{2,t}), \tag{4.5}$$

where $\boldsymbol{p}_a^* = \boldsymbol{p}_a - \mathbf{k}_t$, $\boldsymbol{p}_b^* = \boldsymbol{p}_b + \mathbf{k}_t$, $\mathbf{k}_t$ is the transverse momentum exchanged in the pp scattering and the amplitude of elastic proton-proton scattering is taken as:

$$A_{pp}(s, k_t^2) = A_0(s) \exp(-Bk_t^2/2). \tag{4.6}$$

It is assumed that the real part of A_0 is negligible in the high energy limit. The imaginary part is taken from the optical theorem: $\mathrm{Im}A_0(s, t = 0) = s\sigma_{tot}(s)$. The Donnachie-Landshoff parametrisation of the total and elastic pp or $p\bar{p}$ cross sections [84] is used to calculate the rescattering amplitude and $B_{I\!P}^{pp} = 9$ GeV^{-2} is assumed.

For the sake of this analysis, a simple Monte Carlo generator based on this model has been developed. It uses numerical integration over the four-body phase space reduced to 8 dimensions (by invariance under rotation of the total azimuthal angle), to obtain the cross sections and weighted events. An unweighted event MC generator is being developed.

4.2 Dedicated LHC Runs with $\beta^* = 90$ m

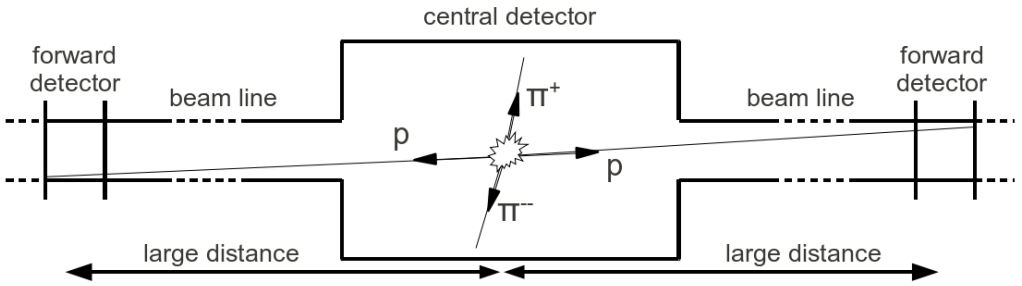

Figure 4.2: Scheme of the measurement concept – pions are measured in the central detectors, whereas protons are detected in the very forward detectors.

The final state of the $pp \to p\pi^+\pi^- p$ process consists of two protons and two pions. The analysis assumes that the pions are detected in the ATLAS central detector, while the protons in the ALFA stations, as sketched in Figure 4.2. The analysis assumed the conditions for the ALFA run in 2011 [85]: $\sqrt{s} = 7$ TeV, $\beta^* = 90$ m LHC optics, an integrated luminosity of 100 μb^{-1} (about 30 hours of data acquisition time at the instantaneous luminosity of 10^{27} cm^{-2}s^{-1}) and the distance between the ALFA detector and the beam centre equal to 4 mm[1].

The nominal optics for the ALFA dedicated runs has $\beta^* = 2625$ m. Such conditions are planned for the future, so far only the $\beta^* = 90$ m runs have been performed. In the following, a few properties of this optics settings, which are important for ALFA measurement, are discussed.

Figure 4.3 presents the proton positions at the first ALFA station together with the detector active area and the shape of the beam pipe. The plotted positions originate from two different processes: elastic – $\Delta E = 0$ and diffractive – $\Delta E = 500$ GeV, corresponding to $\xi \approx 0.14$. Obviously, other non-zero values are also possible for diffractive events. For both processes, two values of the transverse momentum are assumed: 0.1 and 0.2 GeV. Allowing different values of the azimuthal angle leads to the elliptical shapes shown in Figure 4.3. One can see that with increasing transverse momentum, the size of the ellipse increases. Increasing the energy loss, ΔE, moves the centre of the ellipse to the right. The size of the ellipse depends also on ΔE, but this influence is relatively small.

Due to the fact that the ALFA detectors approach the beam in the vertical direction, the acceptance of the detectors at given conditions is to a first approximation independent of ΔE, while being very sensitive to the p_T value. This can be seen in Figure 4.4, where the geometrical acceptance of the ALFA stations as a function of ΔE and p_T is presented. The acceptance value in each $(\Delta E, p_T)$ bin has

[1]The obtained results motivated a common data-taking of the ATLAS central detector and the ALFA stations, which was not planned previously to the study because it is not needed for elastic scattering measurements. Such a run was performed and the data are being analysed.

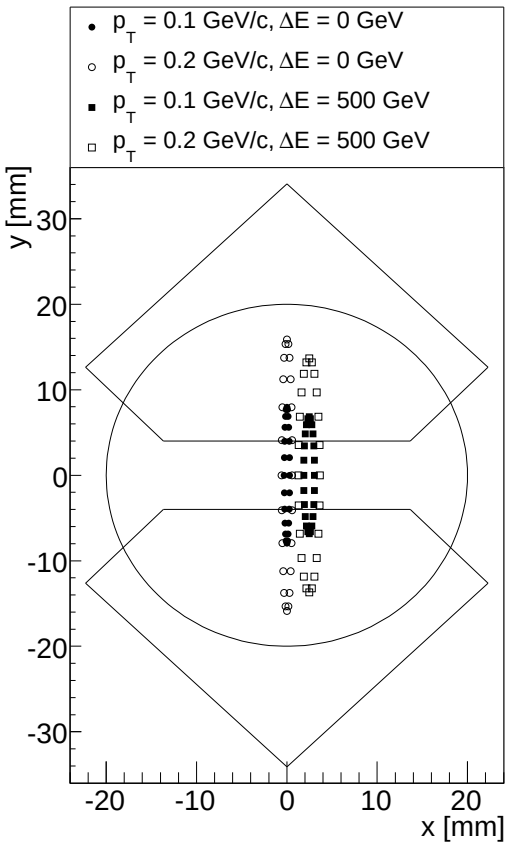

Figure 4.3: Positions of protons with different energy loss (ΔE) and transverse momentum (p_T) in the first ALFA station. The solid lines indicate the beam pipe aperture and the ALFA detector active area.

been obtained by generating a set of protons uniformly distributed in azimuthal angle, transporting them through the magnetic structure of the LHC with the special $\beta^* = 90$ m optics, and calculating the percentage of the protons hitting the detector. One can see that the highest acceptance, above 80%, is obtained for protons with p_T between 0.15 and 0.20 GeV and energy loss up to 500 GeV. A smaller acceptance, above 40%, is obtained for p_T between about 0.1 and 0.3 GeV, with ΔE smaller than 600 GeV. The measurement with a 20% acceptance is possible up to $p_T = 0.6$ GeV.

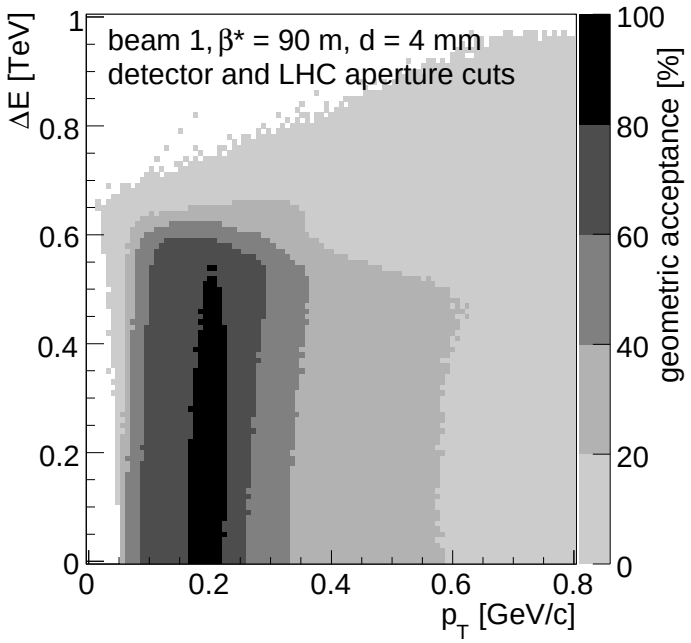

Figure 4.4: Geometrical acceptance of the ALFA detector as a function of the proton energy loss (ΔE) and its transverse momentum (p_T), for a distance between the beam centre and the detector edge of to 4 mm.

The detector acceptance, especially the minimal transverse momentum that can be observed, depends on the distance between the detector edge and the beam centre. This dependence has been studied for the $pp \to p\pi^+\pi^- p$ events and is presented in Figure 4.5. The plot shows the visible cross section, requiring both protons tagged in ALFA detectors, as a function of the studied distance. It is worth mentioning that the total cross section resulting from the calculations is 234 μb. This is much larger than the maximal visible cross section of 135 μb (see Figure 4.5). This is the effect of the properties of the LHC magnetic lattice, namely some protons do not reach the ALFA position, for example due to beam pipe aperture. For a 4 mm distance between the detector edge and the beam centre, which is a realistic value that can be achieved in a run, the visible cross section is 75 μb.

In the $pp \to p\pi^+\pi^- p$ process the key variable is the proton transverse momentum. This is because the energy loss is quite small and does not affect the acceptance of the detectors, see Figure 4.4. The proton p_T distribution is shown in Figure 4.6. One

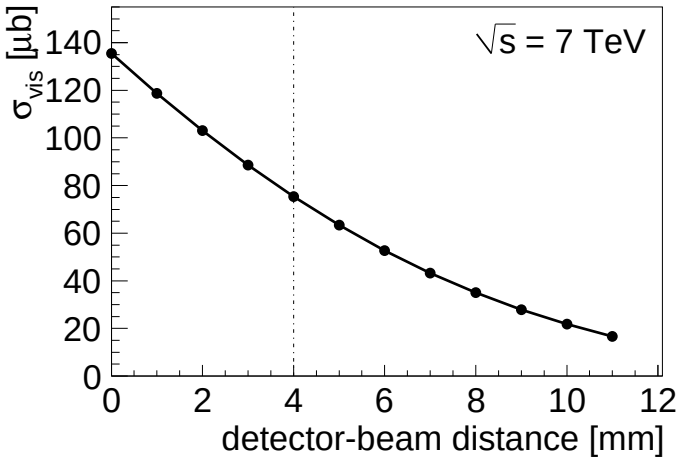

Figure 4.5: Visible $pp \to p\pi^+\pi^- p$ cross section with both protons tagged in the ALFA detectors as a function of the distance between the detectors and the beam centre.

can see that the peak of the distribution is located in the region of high detector acceptance, which makes the measurement possible. Figure 4.6 presents also the distribution after requiring both protons to be tagged in the detectors placed at 4 mm from the beam centre. This reduces the cross section by a factor of about 3, while the distribution peak value is reduced only by a factor of about 2.

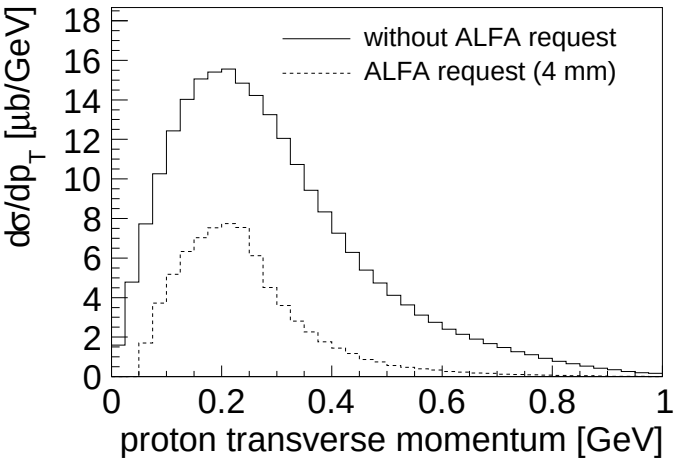

Figure 4.6: Proton transverse momentum distribution. Solid line indicates the generated distribution, without any experimental requirement. Dashed line shows the distributions for events with both protons tagged by ALFA detectors positioned at 4 mm from the beam centre.

4.3 Measurement Using the ATLAS Central Detector

Pions produced in the $pp \to p\pi^+\pi^- p$ process can be measured in the ATLAS central detector. The pion pseudorapidity distribution is presented in Figure 4.7. Taking into account the fact that ATLAS allows pion measurements only the for $|\eta| < 4.9$, see Chapter 3, a large fraction of the events remains undetected. However, due to a strong correlation between the pseudorapidities of both pions, when one of them falls in the detector acceptance, it is very likely that the other one also can be detected. This correlation is presented in Figure 4.8.

The pion measurement can be performed either in the tracking detector or in the calorimeter. In the central region ($|\eta| < 2.5$) the measurement is possible using both detectors. However, the tracker is favoured, because it provides particle charge identification. In addition, particles with transverse momentum below 400 MeV cannot reach the calorimeter due to the detector magnetic field. In the forward region, $2.5 < |\eta| < 4.9$, only the calorimeter measurement is possible. For the sake of simplicity, the study assumes that either both pions are measured in the tracker, or both in the calorimeter, as depicted in Figure 4.8 with black rectangles. In reality, these two measurements can be combined to increase the statistics and cross check the results. It is worth noticing that the ATLAS magnetic field is quite large in order to measure the transverse momentum of particles with very large energy. The discussed measurement could benefit from a reduction of the magnetic field strength. Naturally, this would require certain changes in the ATLAS reconstruction procedure [86]. However, it would increase the efficiency of low p_T tracks reconstruction.

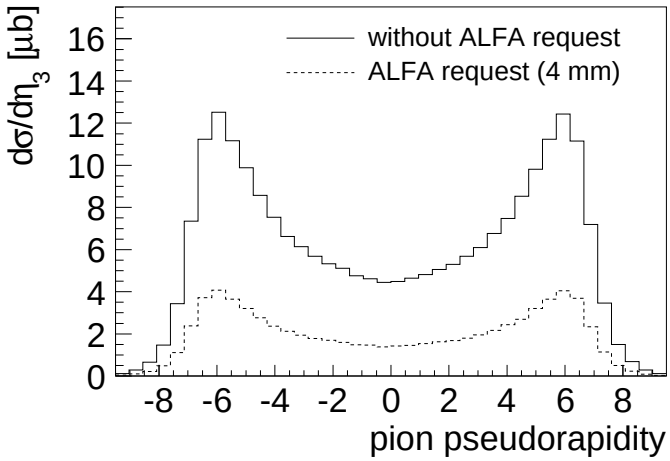

Figure 4.7: Total cross section as a function of the pion pseudorapidity.

The inner detector measurement uses reconstructed tracks, which leads to the determination of the pion momentum and charge. In the standard ATLAS event processing, only tracks with $p_T > 500$ MeV are reconstructed. However, with a

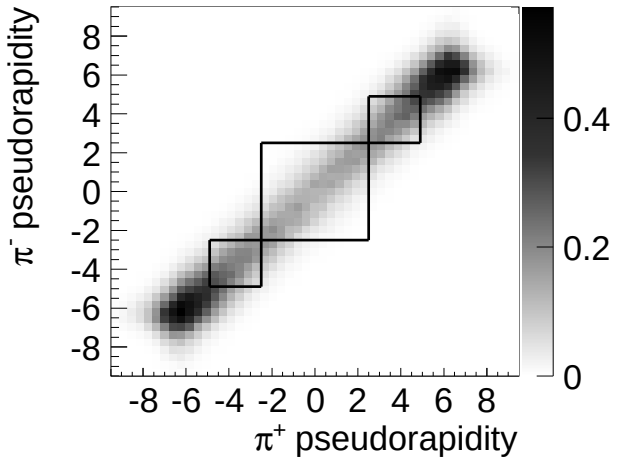

Figure 4.8: Correlation between the pseudorapidities of produced pions. Black squares show the different regions that can be used for the measurement.

dedicated low-p_T reconstruction it is possible to reconstruct tracks down to $p_T = 100$ MeV, as was done for the ATLAS minimum bias analysis [87]. In that case the efficiency to reconstruct such low-p_T tracks was quite small, see Figure 4.9, because of their high curvature in the magnetic field, which makes the track reconstruction difficult. For the exclusive pion production process the reconstruction efficiency is expected to be higher due to the simplicity of the events containing only two tracks. This would probably need a different track reconstruction method, better suited for such simple events.

Figure 4.10 shows the distribution of the pion transverse momentum before and after requesting the proton tags. The shaded area shows the region where the measurement is possible due to the limitation on the minimal p_T discussed above. Figure 4.11 presents the visible cross section, requesting the protons to be tagged in ALFA detectors and pions p_T above a given threshold, as a function of this threshold. For a minimal pion p_T of 100 MeV, the cross section is about 12 μb, while for the standard ATLAS threshold of 500 MeV it is only about 3 μb. This clearly shows that in order to keep the majority of events, the tracking needs to be extended down to the lowest possible transverse momenta.

The calorimetric measurements can be influenced by noise, which can be quite high, especially in the forward regions of the calorimeter, in particular in the ATLAS FCal. In order to avoid the signal contamination, one needs to select particles of high enough energy. Energy greater than 4 GeV is well above the FCal noise [88]. The distribution of the pion energy is presented in Figure 4.12, where the shaded area shows the part of the distribution that can be accessed experimentally. Figure 4.13 shows the visible cross section as a function of the energy threshold. For $E = 4$ GeV one obtains about 9 μb.

The combination of the visible cross sections from both the calorimetric and the tracker measurements leads to a total visible cross section of about 21 μb. For the

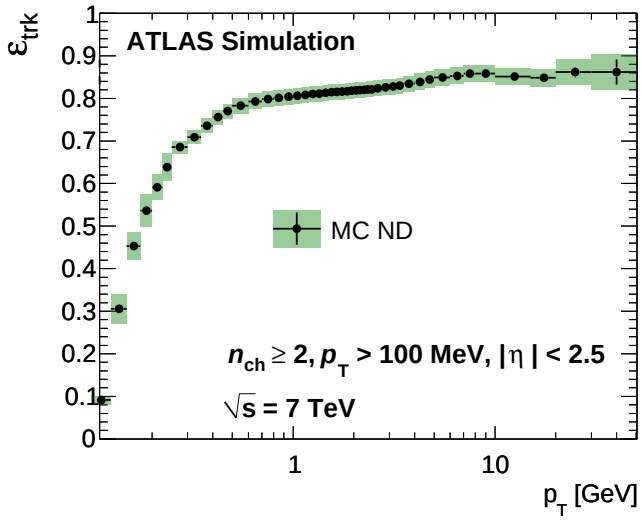

Figure 4.9: Track reconstruction efficiency as a function of p_T.

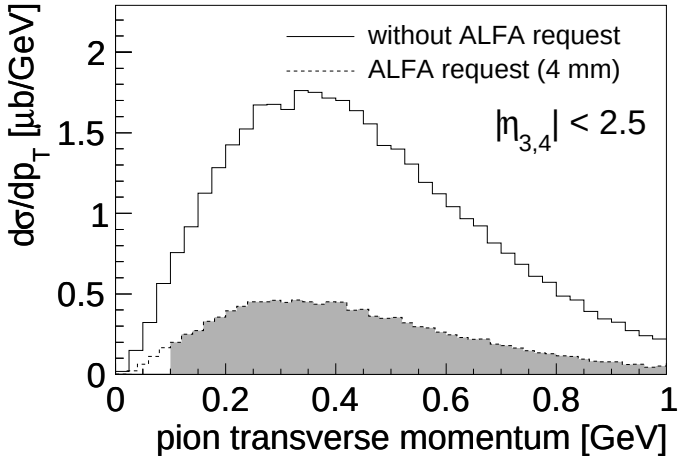

Figure 4.10: Pion transverse momentum distribution in the tracking detector.

assumed luminosity of 100 μb^{-1} this results in more than 2000 events that can be recorded. This could lead to measurements of not only the visible cross section, but also of various distributions. The most important one is the $\pi^+\pi^-$ invariant mass distribution, where various resonances could show up. Figure 4.14 shows a possible measurement of this distribution that could be performed using the ATLAS inner detector only, and assuming only the statistical uncertainty.

On 20$^{\text{th}}$ of October 2011 an ALFA run (no. 191373) of about four hours was performed. The instantaneous luminosity during the run was about $7 \cdot 10^{27}$ cm^{-2}s^{-1}. Slightly more than 100 μb^{-1} of integrated luminosity was collected, which is the same as was used for this analysis. However, the distance between the detector and the beam centre was equal to 6 mm, instead of 4 mm. This leads to a decrease of the visible cross section by about 30%. However, a substantial number of events has

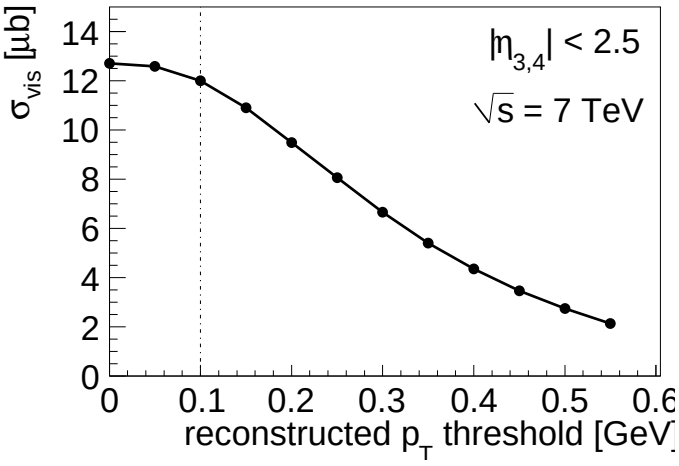

Figure 4.11: Cross section for $|\eta| < 2.5$ as a function of the p_T threshold of the track reconstruction. The dash-dotted line shows the lower boundary of the region accessible by ATLAS.

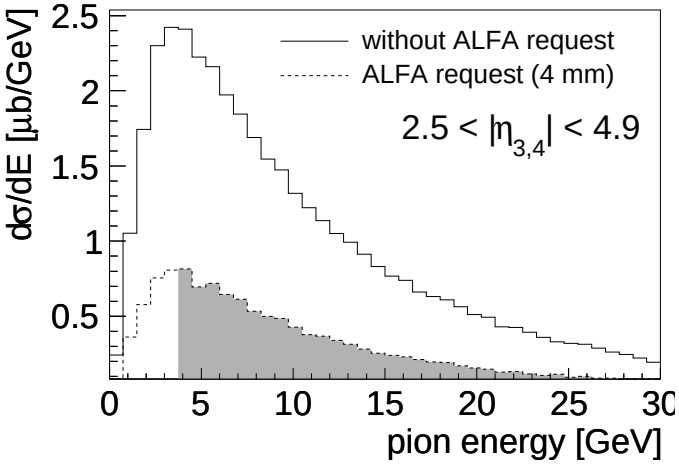

Figure 4.12: Pion energy distribution in the calorimeter.

been registered. The proposed investigation is now being carried out by the ALFA Group.

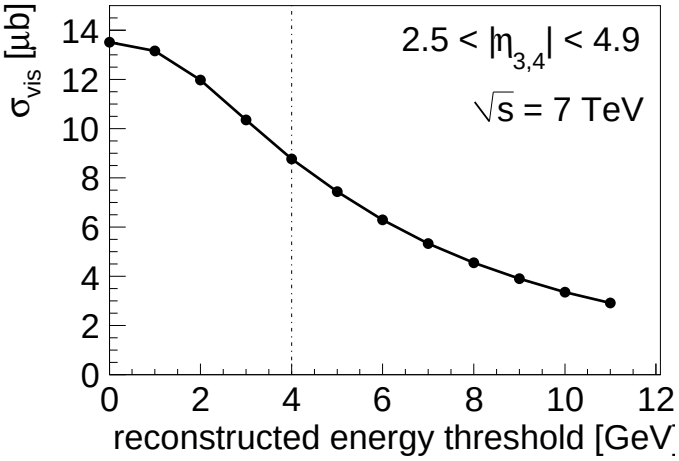

Figure 4.13: Cross section for $2.5 < |\eta| < 4.9$ as a function of energy threshold. The dash-dotted line shows the lower boundary of the region accessible by ATLAS.

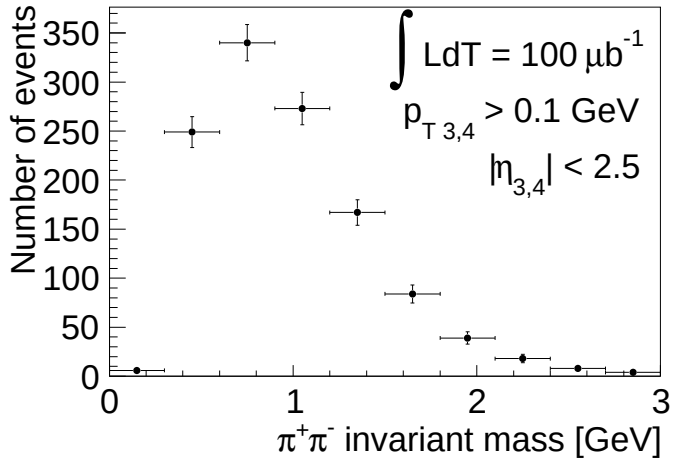

Figure 4.14: Possible measurement of the $\pi^+\pi^-$ invariant mass distribution for an integrated luminosity of 100 μb^{-1} (only statistical errors are shown).

Chapter 5

The AFP Detectors

Limitations of the ALFA detectors, both in the acceptance and the impossibility to work during the nominal LHC luminosity runs, imply the necessity of additional detectors, better suited for diffractive measurements, especially for low cross section processes and exploratory physics. This chapter presents the ATLAS Forward Proton (AFP) detectors, which are planned to be installed in the ATLAS experiment [89].

The AFP project aims at installing detectors at 210 metres from the ATLAS Interaction Point (AFP210). The first phase of the installation is planned for the LHC shutdown in 2013 – 2014. The AFP210 detectors will allow measurements of protons that lost 2 – 14% of their initial energy. This leads to the acceptance in centrally produced mass between 300 and 2000 GeV (at $\sqrt{s} = 14$ TeV). The physical programme motivating the need of these detectors is presented in Section 5.1. Section 5.2 discusses the detectors design, while Sections 5.3 and 5.4 their features due to the LHC optics, namely the detector acceptance and resolutions of the proton energy reconstruction.

The AFP project considers also a possibility of installing additional detectors at 420 meters (AFP420). These detectors would be sensitive to smaller energy losses of protons and hence smaller masses. The installation of the AFP420 detectors is technically difficult, due to the LHC cryostat that is present at 420 metres and needs to be redesigned and rebuilt in order to incorporate the proposed detectors. Therefore, the installation is considered for the LHC shutdown scheduled after 2017 and will depend on the physics results obtained before. This is because the main motivation for the AFP420 detectors is the exclusive Higgs boson measurements. The AFP210 measurements may considerably improve the uncertainties of the exclusive Higgs production models, as argued in Chapter 2. This, together with recent reports on the discovery of a particle consistent with the Higgs boson [54, 55], can strongly

support the AFP420 detectors installation.

Since the timescale of the AFP420 detectors is quite long and their installation is not certain, only the role of the AFP210 detectors is discussed here. Therefore, in the following the AFP acronym will regard only the AFP210.

The work presented in this chapter was partially published in ATL-LUM-INT-2009-003, Nucl. Instrum. Meth. A609 (2009) 136-141 and ATL-COM-PHYS-2012-775.

5.1 Physics Motivation

The physics motivation behind the AFP detectors consists of many possible QCD studies of diffraction, as well as searches for *new physics*. The AFP detectors enhance considerably the ATLAS capabilities in both fields, while not compromising any other measurements in ATLAS.

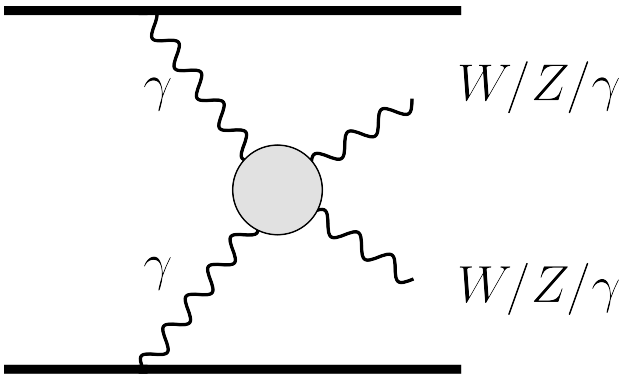

Figure 5.1: Feynman diagram of two-photon production of $W/Z/\gamma$ pairs.

One of the possible *new physics* searches is based on the measurements of electroweak boson pair production in two-photon processes (see Figure 5.1). In the Standard Model the cross sections for these processes are well known, since they involve only electroweak interactions. In some theories beyond the Standard Model (BSM) the cross sections for these processes are increased, *e.g.* due to the exchange of a virtual new particle. This is especially true for Higgs-less and extra dimension scenarios [90]. Since a large number of such theories exist, it is convenient to use an effective approach – the values of the *anomalous coupling constants* are introduced by hand rather then calculated from first principles for a given model. Instead of analysing a specific theoretical model, the Standard Model Lagrangian can be modified by adding new terms representing the BSM effects:

$$\begin{aligned}\mathcal{L}_{\text{eff}}^{\text{BSM}} = &- \frac{e^2}{8}\frac{a_0^W}{\Lambda^2}F_{\mu\nu}F^{\mu\nu}W^{+\alpha}W^-_\alpha - \frac{e^2}{16}\frac{a_C^W}{\Lambda^2}F_{\mu\alpha}F^{\mu\beta}(W^{+\alpha}W^-_\beta + W^{-\alpha}W^+_\beta) \\ &- \frac{e^2}{16\cos^2\theta_W}\frac{a_0^Z}{\Lambda^2}F_{\mu\nu}F^{\mu\nu}Z^\alpha Z_\alpha - \frac{e^2}{16\cos^2\theta_W}\frac{a_C^Z}{\Lambda^2}F_{\mu\alpha}F^{\mu\beta}Z^\alpha Z_\beta,\end{aligned} \tag{5.1}$$

Table 5.1: 95% CL interval, 3σ evidence, and 5σ discovery potential on the $WW\gamma\gamma$ and $ZZ\gamma\gamma$ anomalous quartic parameters using $\mathcal{L}$=30fb^{-1} (left) and $\mathcal{L}$=200fb^{-1} of data at high luminosity with forward detectors, and with or without the form factors applied. From [91].

		limits for $\mathcal{L}$=30 fb^{-1} [10^{-6} GeV^{-2}]				limits for $\mathcal{L}$=300 fb^{-1} [10^{-6} GeV^{-2}]			
	form factor	$\left\lvert\frac{a_0^W}{\Lambda^2}\right\rvert$	$\left\lvert\frac{a_C^W}{\Lambda^2}\right\rvert$	$\left\lvert\frac{a_0^Z}{\Lambda^2}\right\rvert$	$\left\lvert\frac{a_C^Z}{\Lambda^2}\right\rvert$	$\left\lvert\frac{a_0^W}{\Lambda^2}\right\rvert$	$\left\lvert\frac{a_C^W}{\Lambda^2}\right\rvert$	$\left\lvert\frac{a_0^Z}{\Lambda^2}\right\rvert$	$\left\lvert\frac{a_C^Z}{\Lambda^2}\right\rvert$
95%	$\Lambda_{cut} = \infty$	1.2	4.2	2.8	10	0.7	2.4	1.1	4.1
	$\Lambda_{cut} = 2$ TeV	2.6	9.4	6.4	24	1.4	5.2	2.5	9.2
3σ	$\Lambda_{cut} = \infty$	1.6	5.8	4.0	14	0.85	3.0	1.6	5.7
	$\Lambda_{cut} = 2$ TeV	3.6	13	9.0	34	1.8	6.7	3.5	13
5σ	$\Lambda_{cut} = \infty$	2.3	9.7	6.2	23	1.2	4.3	4.1	8.9
	$\Lambda_{cut} = 2$ TeV	5.4	20	14	52	2.7	9.6	5.5	20

where a_0^W, a_C^W, a_0^Z and a_C^Z are the anomalous couplings constants and Λ is the mass scale of *new physics*. The values of all these couplings in the Standard Model are equal to zero and can be non-zero in BSM scenarios.

The main process to study is the production of the W boson pairs. Apart from the BSM motivations, it is interesting also from the Standard Model point of view. This measurement can provide a direct check of the existence of the quartic $\gamma\gamma WW$ coupling, which is needed to ensure the tree level unitarity of the Standard Model, but has never been verified experimentally. A study showing the possibility of reaching coupling values several orders of magnitude below the present limits has been performed with fast simulation of the ATLAS detector[1], without taking into account the pile-up background and considering only the fully leptonic decay channel (both W bosons decaying leptonically) [91]. The obtained limits possible to reach with an integrated luminosity of 30 and 300 fb^{-1} are presented in Table 5.1.

Recently, these results have been confirmed with the full ATLAS simulation [92]. Figure 5.2 presents the number of expected signal events as a function of the anomalous a_0^W coupling for LHC runs at $\sqrt{s} = 14$ TeV, an integrated luminosity of 300 fb^{-1} and average pile-up multiplicity $\mu = 46$. For these conditions the expected background amounts about 0.5 event. This leads to the sensitivity presented in Table 5.2. This sensitivity is four orders of magnitude better than the present LEP limits [94]. In addition, it is two orders of magnitude better than the one achievable at the LHC with alternative methods that does not use the AFP detectors – non-diffractive production of events containing two photons and a W boson [95, 96]. The values that can be reached with AFP are small enough to probe extra-dimension models.

[1]The fast simulation of the detector smears the momenta of produced particles according to Gaussian distributions with widths equal to the expected resolutions of the detector. It does not take fully into account effects like reconstruction efficiency or misidentification.

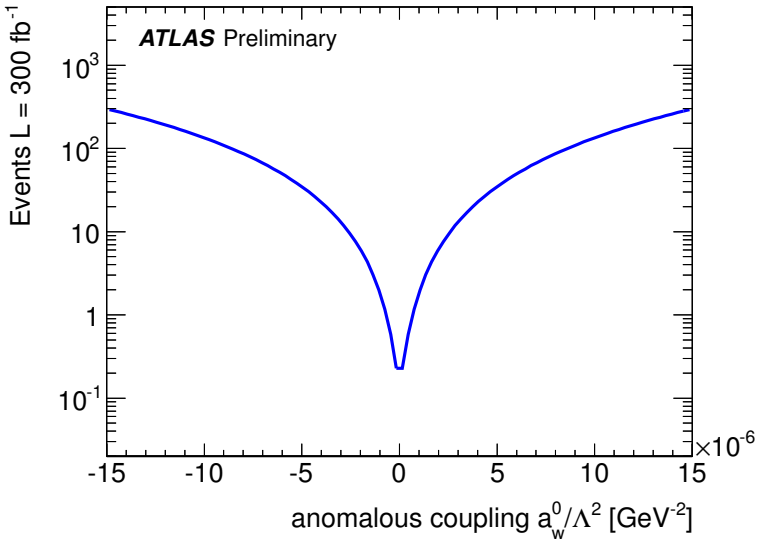

Figure 5.2: Number of W pair events in two-photon exchange process after event selection, as a function of the value of a_0^W/Λ^2 coupling. [92]

Table 5.2: Expected sensitivity on a_0^W/Λ^2 anomalous coupling in two-photon WW production processes measured with the AFP detectors. The limits are given for 5σ discovery and 95% confidence level limits, for two LHC running scenarios: 40 fb^{-1} with an average pile-up multiplicity $\mu = 23$ and 300 fb^{-1} with $\mu = 46$.

	5σ	95% CL
$\mu = 23$, L $= 40$ fb^{-1}	$5.5 \cdot 10^{-6}$	$2.4 \cdot 10^{-6}$
$\mu = 46$, L $= 300$ fb^{-1}	$3.2 \cdot 10^{-6}$	$1.3 \cdot 10^{-6}$

The QCD programme of the AFP detectors consists of measuring single and central diffractive production of jets, W and Z bosons. The feasibility study for central diffractive W boson production is presented in detail in Chapter 6. These processes can be measured in dedicated runs with small pile-up multiplicity, optimally $\mu = 1$, which will lead to clean measurements with greatly reduced backgrounds. These measurements will probe the Pomeron quark and gluon structure as well as the mechanism of diffractive interactions. They will extend the studies performed at HERA and Tevatron to a new kinematic domain.

With the AFP detectors it is also possible to measure the central exclusive production of jets. This is very important in order to constrain the exclusive production models, in particular the exclusive production of the Higgs boson, see Chapter 2. The studies of exclusive jet production have also been performed with the full ATLAS detector simulation and taking into account the influence of large pile-up environment in nominal, high luminosity LHC runs [92]. This measurement will fully make use of all the potential of the AFP detectors, therefore the key steps are described below.

In order to select exclusive events, where two protons stay intact and are scattered at very small angles, it is requested that on both sides of the interaction point there are protons tagged in the AFP detectors (*double tag*). However, due to pile-up, also non-diffractive jet production can have similar signature, when accompanied by two soft single diffractive interactions, see Figure 5.3. Such a case is actually the dominant background for the considered process. Another possibility is single diffractive jet production accompanied by at least one soft interaction giving a forward proton. Finally, non-exclusive central diffractive jet production also contributes to the background.

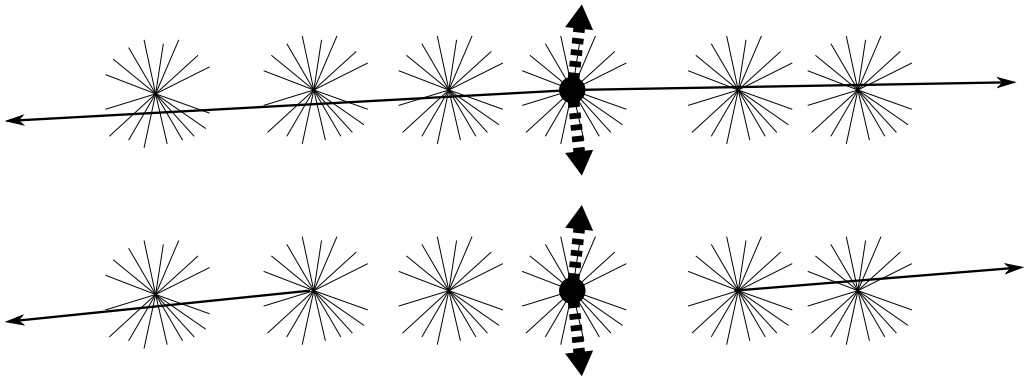

Figure 5.3: Schematic diagrams of multiple interaction events (with pile-up). The thin lines represent the particles produced, thick dashed line the produced hard object and the thin line with arrow the intact protons. Top: diffractive production. Bottom: non-diffractive production with a diffractive signature (2 intact protons) due to pile-up.

The probability that a non-diffractive interaction has a double tag signature depends on the average pile-up multiplicity, as presented in Figure 5.4. The inverse of

this probability is the non-diffractive background reduction factor caused by requesting a double tag in the event. One can see that for small values of μ the reduction is quite large, up to $5 \cdot 10^3$ for $\mu = 1$. It decreases very quickly with μ and above $\mu = 10$ the dependence flattens. At $\mu = 25$ the probability is about 10%. This is quite a large value, taking into account that the cross section for non-diffractive jet production is greater than for exclusive jets by about six orders of magnitude. Hence, additional discriminants are needed.

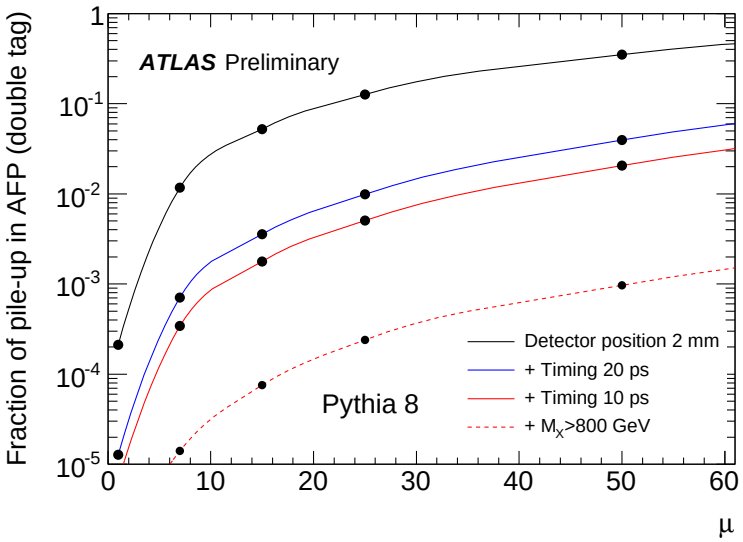

Figure 5.4: Fraction of non-diffractive events that pass the successive experimental selection criteria as a function of the average pile-up multiplicity μ. The experimental cuts are: AFP double tag with active detector area 2 mm from the beam centre (solid black line), time compatibility with timing detectors providing a resolution of 20 and 10 ps (solid blue and red line, respectively), the missing mass M_X being greater then 800 GeV (dashed red line).

Since in the exclusive events all particles in the event are measured, the kinematics is fully constrained. One can compare the properties of the central state with the ones of the tagged protons and check whether they are compatible. One example is the mass of the jet system M_{jj} and the missing mass M_X calculated from AFP measurements (ξ_1 and ξ_2). In the case of exclusive jets, the ratio of these two masses is around one modulo various experimental effects, while for background processes the value is lower, see Figure 5.5. By requesting the mass fraction to be larger than 0.9 and smaller than 1.15 (marked in the plot with vertical dashed lines) a background reduction of about an order of magnitude is obtained. In a similar way, one can compare the rapidity of the jet system y_{jj} and the rapidity of the central system calculated from the kinematics of the protons:

$$y_X = \frac{1}{2} \log \frac{\xi_1}{\xi_2}. \tag{5.2}$$

The distribution of the difference between these two values is plotted in Figure 5.6. For exclusive jets it peaks strongly at zero, while for the discussed backgrounds it is flatter. Requesting the absolute value of the difference being smaller than 0.075 results in a background reduction factor of about 20.

Instrumentation of the AFP detectors with additional detectors capable of time-of-flight measurement with picosecond resolution (see next section) will allow additional constraint on the event exclusivity. The time information can be compared with the longitudinal position of the vertex reconstructed in the ATLAS inner detector. This can further reduce the background by a factor of about 10, see Figure 5.7.

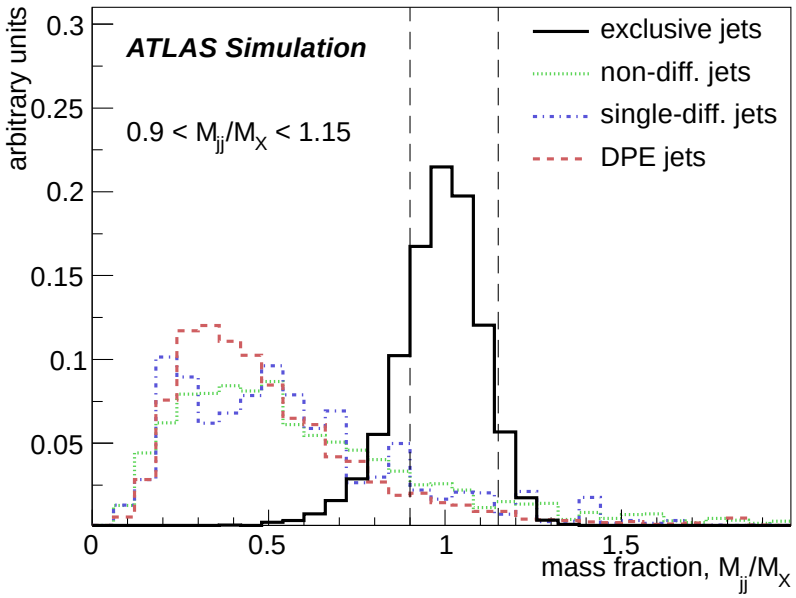

Figure 5.5: Mass fraction (ratio of the dijet mass m_{jj} to the missing mass M_X) distribution for exclusive jets and the dominant backgrounds: non-diffractive, single diffractive and central diffractive (DPE).

Figure 5.8 presents a possible measurement of exclusive jet production – the distribution of the leading jet transverse momentum. The analysis [92] assumed the average pile-up multiplicity equal 23 and integrated luminosity of 40 fb^{-1}. One can see the contributions from the non-diffractive, single diffractive and central diffractive (DPE) processes, as well as from the exclusive signal. S values written in each p_T bin are the statistical significances of the measurement. The dashed lines mark the present uncertainty of the exclusive production models. It is important to point out that although the final sample is considerably contaminated with background, the number of collected events is high enough to make the measurement significant. In addition, the obtained results confirm the ones presented in Chapter 2, *i.e.* an exclusive jet measurement can be used for constraining the exclusive production models.

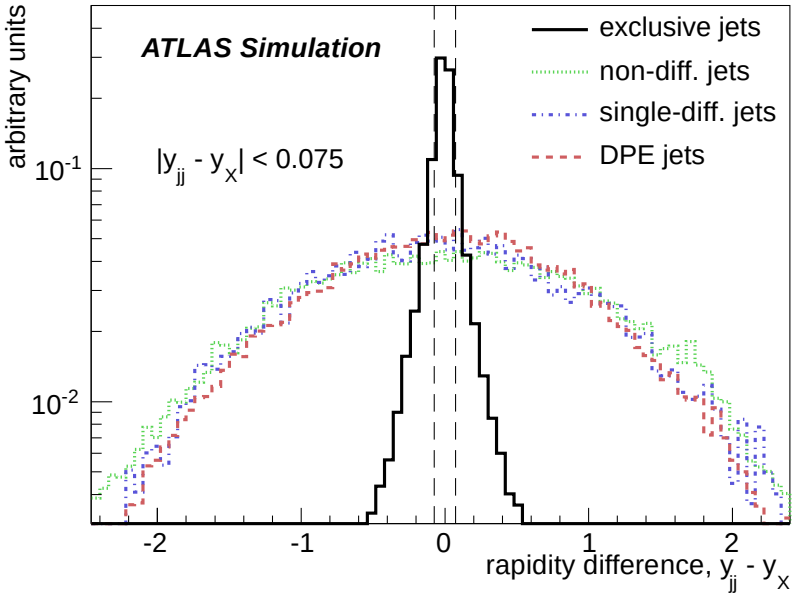

Figure 5.6: Distribution of rapidity difference (rapidity of the dijet system y_{jj} minus the rapidity of the central system y_X) for exclusive jets and the dominant backgrounds: non-diffractive, single diffractive and central diffractive (DPE).

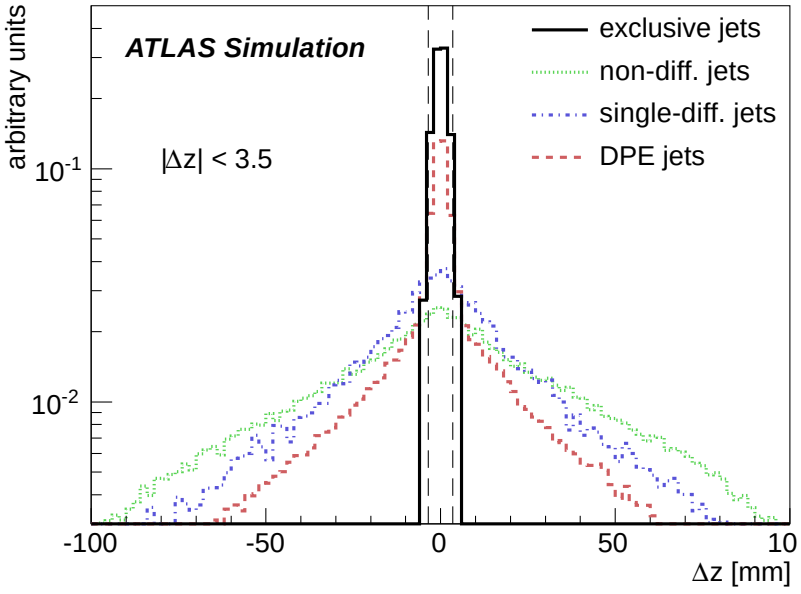

Figure 5.7: Distribution of the difference between the longitudinal vertex position reconstructed from the inner detector measurement and from the timing measurement in the AFP detectors. The distribution is shown for exclusive jets and the dominant backgrounds: non-diffractive, single diffractive and central diffractive (DPE).

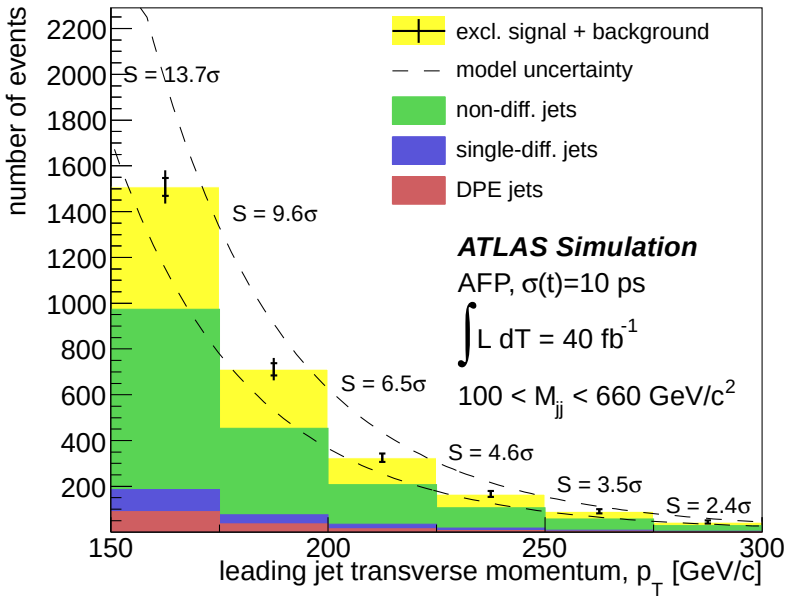

Figure 5.8: Distribution of the leading jet transverse momentum after central exclusive jets selection (see text).

5.2 Detector System

The aim of the AFP detectors design is to measure the kinematics of the intact proton, *i.e.* the position and the direction of its trajectory and its time of flight. From the position and angle measurements it is possible to obtain the momentum of the scattered proton emerging from the interaction. This is because the proton path in the magnetic field depends its momentum and it is possible to unfold this dependence (details in Section 5.4). The proton time-of-flight measurement is crucial in high pile-up environment. It provides a way to reject events in which the protons tagged in the AFP detectors come from minimum bias collisions accompanying a hard non-diffractive interaction, mimicking the diffractive signature.

For position measurements, the AFP stations will be equipped with silicon tracking detectors with spacial resolution of 10 μm in the horizontal direction and 30 μm in the vertical one. Such resolutions will be provided by six layers of silicon 3D pixel sensors [93] in each station. A pixel layer will cover an area of about 20×19 mm^2 and the size of a pixel will be 50×250 μm^2 in the x and y directions, respectively. The horizontal resolution is better because the energy reconstruction is based on the information coming from this direction, as will be discussed later on.

The elevation angles of the trajectory are small, of the order of microradians, both in the horizontal and the vertical direction. In order to measure them precisely, the position measurement needs to be performed at two locations separated along the proton trajectory. Therefore, on each outgoing proton beam (each side of ATLAS) there will be two AFP stations, located at 206 and 214 metres from the interaction point, see Figure 5.9.

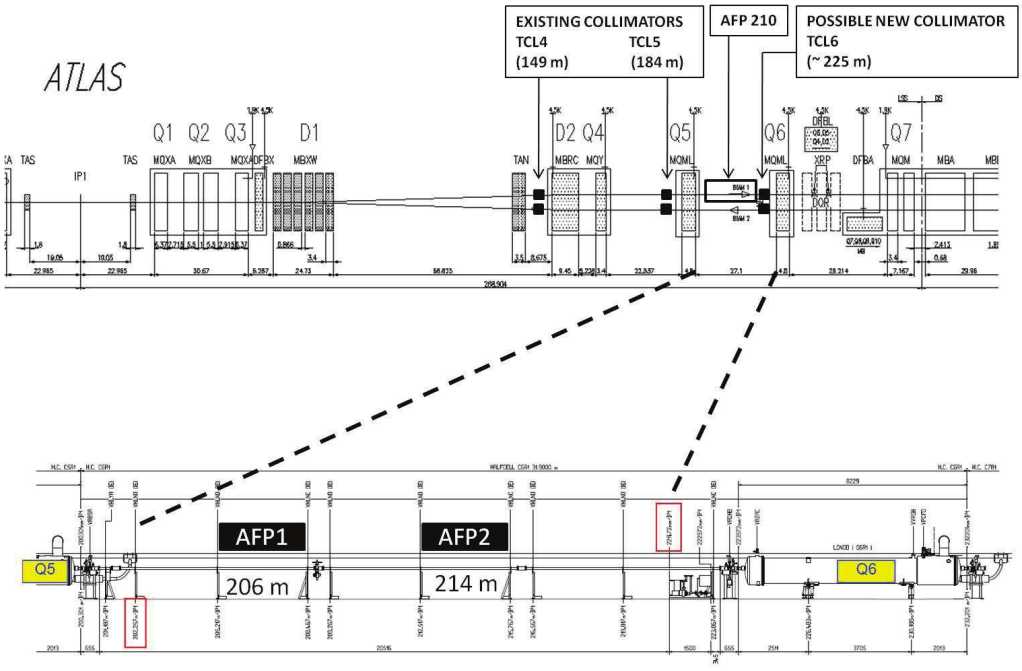

Figure 5.9: Top: the LHC beam line on one side of the ATLAS IP. Bottom: A zoom on the region of the AFP detectors.

The time of flight measurements will be performed with the QUARTIC detectors [97], developed specially for the AFP project. They consist of quartz bars oriented at the Cerenkov angle with respect to the beam trajectory. A proton traversing such a bar emits Cerenkov photons, which are then detected in a MCP-PMT detector, c.f. Figure 5.10. This provides a time measurement with a resolution of about 30 ps.

In order to provide a sufficient rejection for pile-up events the timing resolution needs to be of the order of 10 ps. This resolution can be obtained with eight quartz bars, arranged one after another in the beam direction, see Figure 5.10. Eight independent time measurements lead to resolution improvement by a factor of about $\sqrt{8}$. Timing resolution of 10 ps corresponds to about 3 mm resolution of the interaction vertex longitudinal position and allows a rejection of about 90% of the background events.

The actual design of the detector assumes four rows of eight bars, in order to be able to measure events in which there is more than one proton crossing the detector. Each bar has a cross section of 5×5 mm^2 and a length varying between 8 and 12 cm. Such a detector will fully cover the silicon detector area. One should mention that a design with quartz fibres or varied bar widths (thinner bars close to the beam), which would equalise the proton hit rates among the bars, is also considered. Eight quartz bars crossed by a proton correspond to about 0.3 radiation length and 0.1 nuclear interaction length. A proton traversing the QUARTIC detector is thus

likely to interact with its material. Therefore, the position measurement in the silicon detectors must be performed before the timing one – the QUARTIC detector will be located in the second AFP station (at 214 m), after the silicon detector. Otherwise, the position measurement could be compromised.

Other key issues of the timing detectors involve radiation hardness of the MCP-PMT detector, read-out electronics and reference clock. The obtained solutions can be also adapted for medical applications. In particular, the PET devices could benefit from picosecond timing measurements [98].

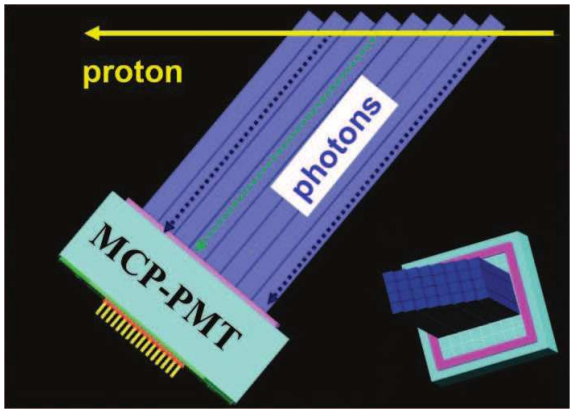

Figure 5.10: Schematic diagram of the QUARTIC detector.

In order to measure diffractively scattered protons, the detectors need to be located very close to the beam. Usually, a distance of 15σ is assumed, where σ is the beam width at the detector location. However, depending on the beam quality the available distance may vary, so that a realistic assumption is $10 - 20\sigma$. At 210 metres the beam width is of the order of 100 μm, leading to possible distances varying between 1 and 2 mm. This is well inside the LHC beam pipe, which has a radius of about 25 mm at this location.

In addition, it must be possible to change the position of the detectors (their distance from the beam) according to the beam conditions. This is due to the fact that usually at the beginning of a run the beams can be unstable, which may lead to detector or beam pipe damages. This requires special devices that are capable of moving the detectors close to the beam, changing their distance from the beam and keeping the accelerator vacuum safe.

There are two solutions to this problem. The first one is the *Roman Pot* apparatus, which enables the insertion of the detectors into the accelerator beam pipe. It is used in the ALFA detectors, see Chapter 3. This solution is not well suitable for the AFP detectors for two reasons. First, moving a Roman Pot involves changing the vacuum volume and requires a force proportional to the area of the inserted part (about 10 N per cm^2). This may compromise the requested positioning precision of 10 μm. Second, the trajectories of the diffractively scattered protons are bent mainly in the horizontal direction. This requires that the detectors must approach

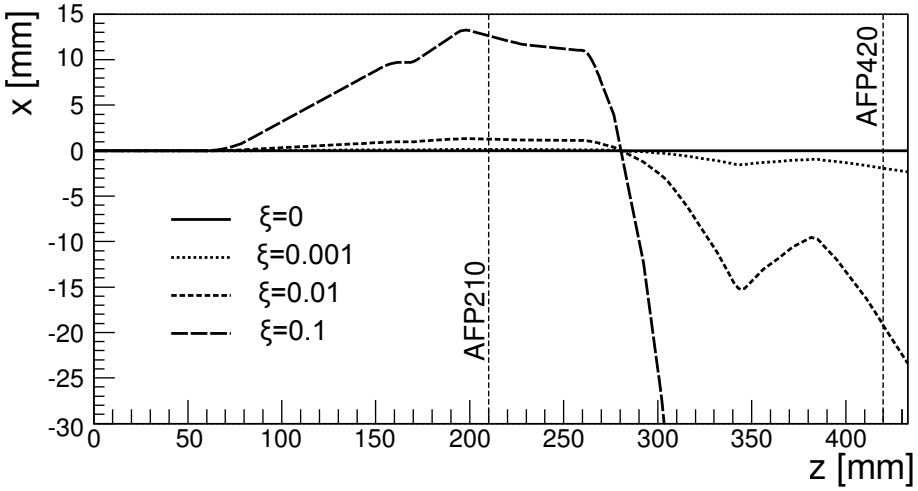

Figure 5.11: Simulated horizontal trajectory of a 7 TeV ($\xi = 0$) proton and protons with three different values of reduced energy loss: $\xi = 0.001$, $\xi = 0.01$ and $\xi = 0.1$ (the x-axis points towards the LHC ring centre).

the beam horizontally. This is not a real problem in the case of the AFP stations around 210 metres, but would make impossible the optional AFP420 stage. At 420 m from the ATLAS IP the positions of the diffractive protons are on the other side of the beam pipe than at 210 m, see Figure 5.11. The space there is very limited due to the presence of the second beam pipe and would make a Roman Pot mechanism impossible to fit in.

The solution chosen for the AFP detectors assumes that a large section of the beam pipe containing the detectors moves close to the beam when the beam is stable. This mechanism has been used at the HERA collider and is called *Hamburg movable beam pipe*. Figure 5.12 shows a design of the beam pipe section that is made movable. One can see the pocket, in which the detectors will be installed, with its windows and floor. In addition, the proton beam going through the beam pipe and a diffractively scattered proton are indicated on the plot. In order to put the detectors very close to the beam, the floor needs to be very thin. Also the windows must be thin to minimise the number of events in which there is an interaction between the proton and a nucleus from the window/floor material. On the other hand the thickness must be high enough to sustain the material stress. The design assumes the thickness of the floor and the windows to be 250 and 300 μm, respectively. In addition, in order to prevent the LHC vacuum breakdown a secondary vacuum will be maintained in the box surrounding the movable beam pipe and the detectors.

Figure 5.13 shows the overall setup of the AFP detectors around 210 metres from the IP and the section of the LHC accelerator where the detectors are to be installed, as well as the 206 and 214 stations. The 206 station consists of a secondary vacuum container with a pocket for the silicon detectors. The 214 station contains an additional pocket and additional container for the timing detector.

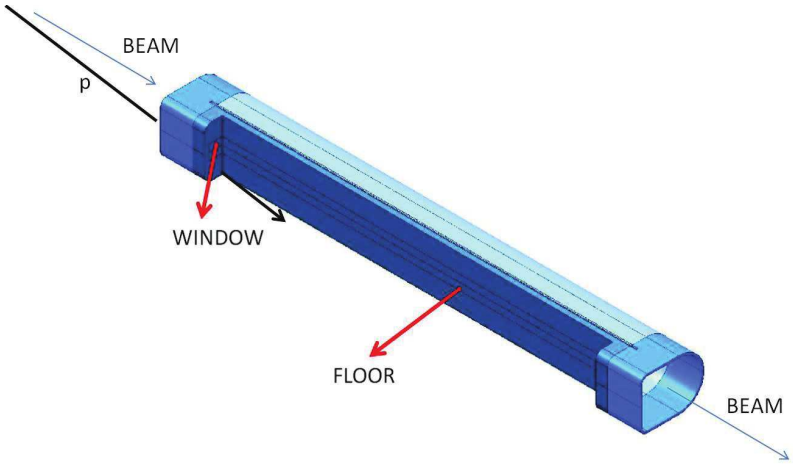

Figure 5.12: Schematic design of the AFP movable beam pipe with a pocket.

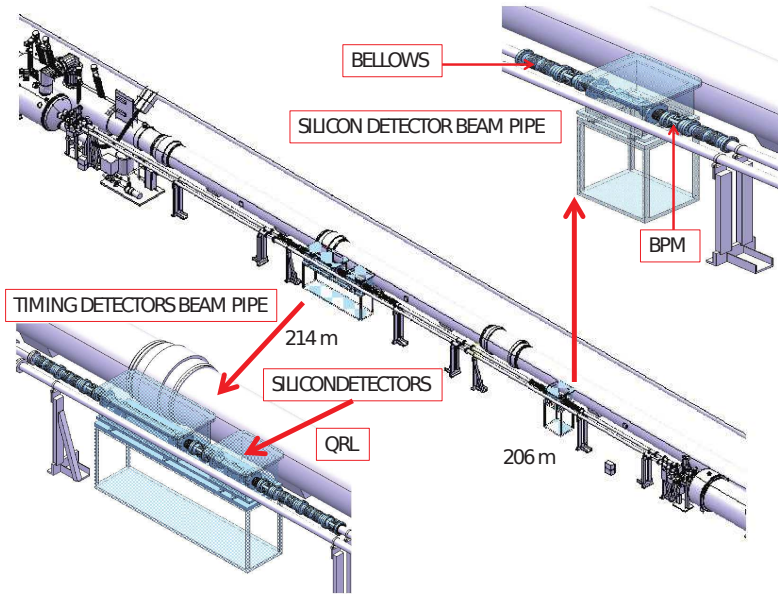

Figure 5.13: Schematic design of the overall AFP detector setup.

5.3 Proton Transport

Before a proton, scattered in a diffractive interaction, reaches the AFP stations, it traverses a part of the LHC magnetic lattice. *Proton transport* or *proton tracking* is the simulation of this process using the information about the magnetic field of the accelerator magnets. A proton trajectory depends on all momentum components and this dependence determines the key properties of the AFP detectors – their geometrical acceptance and momentum resolution.

There are several applications on the market that can be used for proton transport. MAD-X [99] is the one used by the LHC machine in order to calculate the closed beam orbit, when it simulates multiple rotations of a single proton around the whole accelerator circumference. It uses the *thin lens* approximation[2]. This is not satisfactory for the studies of diffractively scattered protons, which may go at large distances from the beam centre. MAD-X PTC [99] is a MAD-X extension designed to work with *thick lenses*. It provides a good description of the proton trajectories and its results are treated as a reference for other programs.

FPTrack [100] and FPTracker [101] are programs that calculate the proton transport for diffractive physics. They are faster and easier to use than MAD-X or MAD-X PTC, while providing compatible results in case of dipole and quadrupole fields. FPTrack and FPTracker differ in the implementation. The last available program is HECTOR [102]. It has been developed for the CMS experiment and is not widely used in the ATLAS community.

To describe the proton kinematics, one often uses the transverse momentum p_T, the azimuthal angle ϕ and the reduced momentum loss ξ, instead of using the Cartesian components of the momentum. This is convenient, since the detectors measure the proton position with respect to the nominal beam position, described by $p_T = 0$ and $\xi = 0$. Effectively, the proton position depends on the deviation from the nominal proton energy, not the energy itself. Sometimes, instead of the transverse momentum, the Mandelstam's four-momentum transfer t is used.

The positions of the diffractively scattered protons at the AFP location[3] are shown in Figure 5.14. The area that can be covered by the detector is indicated with a black rectangle and the point $(0, 0)$ corresponds to the nominal beam centre position. One can see that the position of the majority of the protons is very close to the beam position. This is because the energy lost by a proton in a diffractive interaction is rather small in most cases. Actually, only a small part of diffractively scattered protons can be detected in AFP detectors. However, this is not really a disadvantage when one intends to study the production of heavy objects, used for *new physics* searches. The mass of a centrally produced system is equal to $\sqrt{s \cdot \xi_1 \cdot \xi_2}$. This clearly shows that large ξ values are needed in order to produce

[2] In analogy to the *thin lens* approximation in geometrical optics.

[3] The coordinate system for AFP uses the x-axis pointing outwards the ring, in order to avoid negative values.

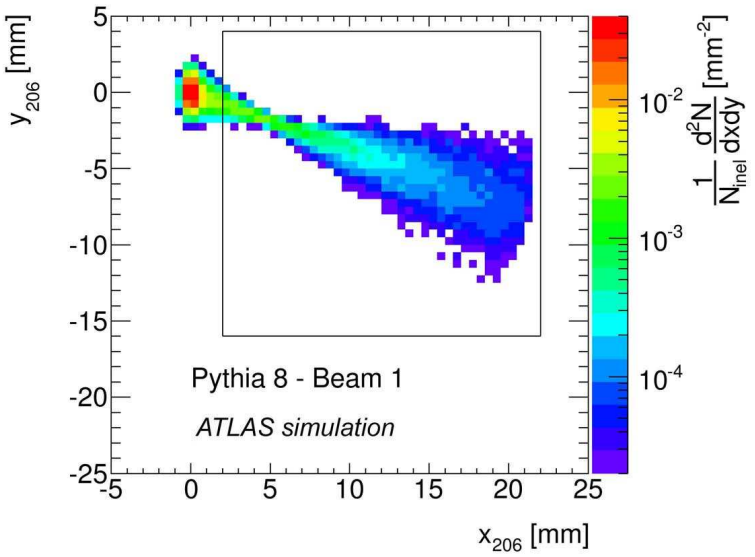

Figure 5.14: Positions of diffractively scattered protons at the AFP location. Black rectangle represents the AFP detector.

heavy objects. Protons that lost a large part of their energy undergo larger deflection in the machine magnets and will cross the AFP detector at a relatively large distance from the beam centre.

The shape observed in Figure 5.14 can be explained using Figure 5.15, where the positions of protons with different values of ξ increasing from 0 in steps of 0.02 are shown. The centre of each ellipse corresponds to $t = 0$ GeV^2, while the points in the ellipses have $t = 0.5$ GeV^2 and different azimuthal angles ϕ.

In order to study the detectors acceptance, a sample of proton uniformly distributed in ξ, p_T and ϕ was generated and transported to the AFP position with FPTracker. Figure 5.16 shows the fraction of protons that are tagged in the AFP detectors as a function of ξ and p_T. One can see that a high value of the acceptance is obtained for $0.02 < \xi < 0.12$ and $p_T < 3$ GeV. It should be noted that the p_T distribution of the diffractively scattered protons is steeply falling. Therefore, it is safe to claim that the AFP acceptance is practically independent of p_T and sensitive mainly to the ξ value.

The AFP detectors acceptance discussed above requires a single proton tagged on one side of the interaction point. For double tag events, in which both protons remain intact and are tagged on both sides of the IP, the important information is the detector acceptance as a function of the *missing mass* M_X, *i.e.* the mass of the centrally produced state. For exclusive production this mass is equal to the invariant mass of the produced hard system (Higgs boson, two jets). For central diffraction also the Pomeron remnants contribute to this mass.

The AFP acceptance for double tag events as a function of the mass of the centrally produced system is presented in Figure 5.17. The plot has been generated

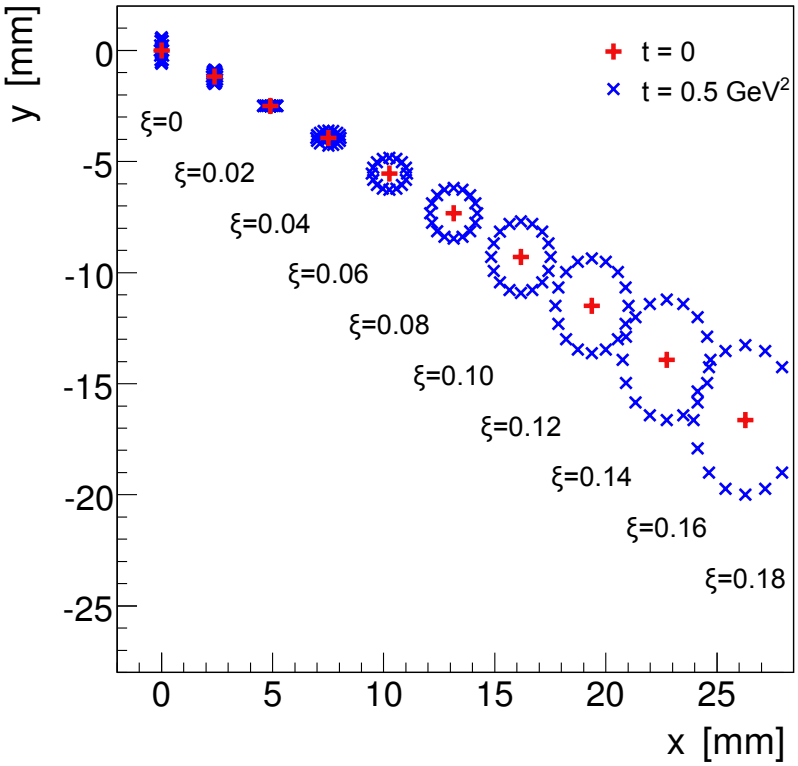

Figure 5.15: Position of protons protons with different ξ and t (see the main text) at the AFP detector position.

using two-photon interaction events, in which M_X is equal to the invariant mass of the two-photon system. It should be mentioned that the exact values of the acceptance can slightly depend on the process considered (the type of produced particle/system and the production mechanism, which can slightly modify the ξ_1 and ξ_2 distributions). The plot shows the acceptance for three distances between the detector and the beam centre: realistic[4] – 1.5 mm, conservative – 2.0 mm and pessimistic – 2.5 mm. The acceptance starts at 150 – 250 GeV and reaches a maximum at about 500 – 650 GeV, depending on the distance. The maximal acceptance is of the order of 60% for M_X around 550 GeV and then decreases to zero at about 1.5 TeV. It is worth noticing that only the smaller mass acceptance depends on the distance between the detector and the beam centre. This is because in order to obtain a large mass system both protons must lose a large part of their energy. This leads to proton positions far away from the edge of the detector.

[4]According to LHC experts the detectors can be placed at 10σ distance from the beam centre. In addition, one has to take into account the thin window width and the detector dead edge.

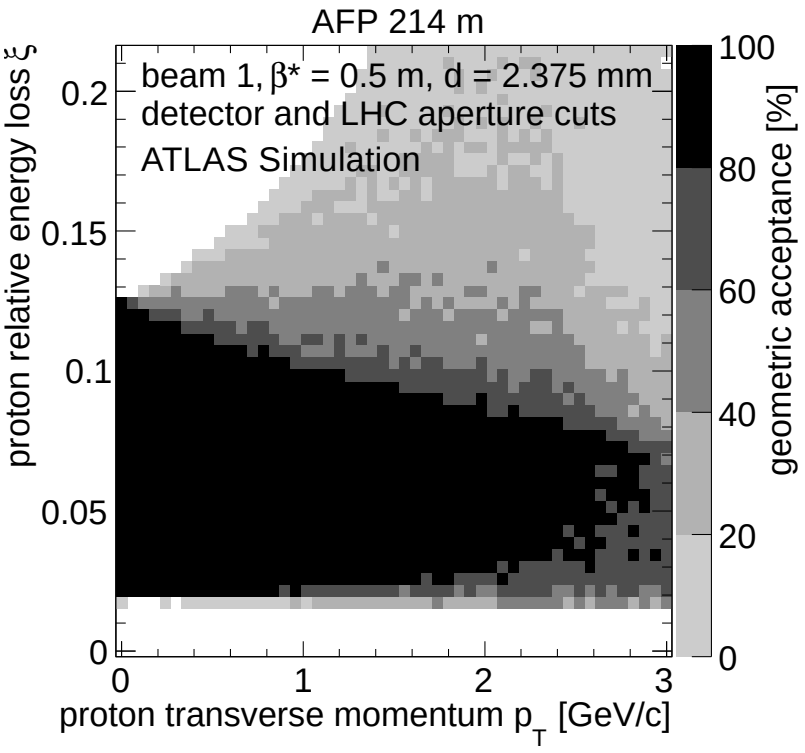

Figure 5.16: Geometrical acceptance of the AFP station at 214 metres from the IP.

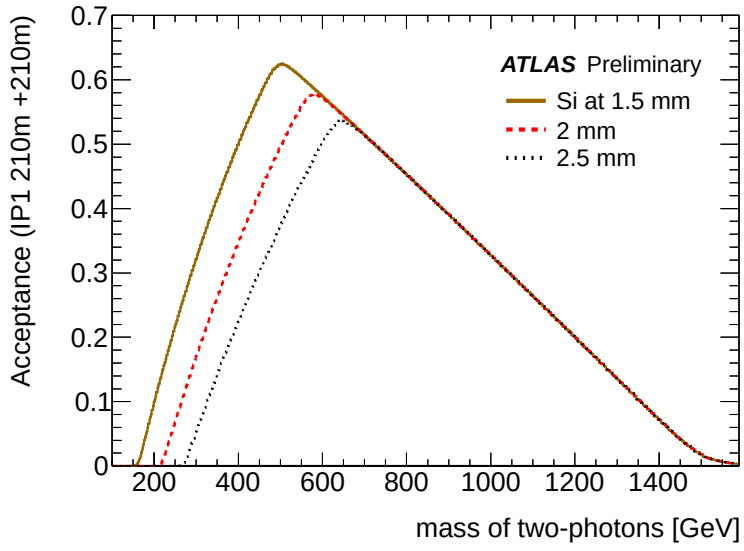

Figure 5.17: Geometrical acceptance of the AFP detectors as a function of central mass in two-photon events.

5.4 Scattered Proton Energy Unfolding

The position measurement at two stations located at 206 and 214 meters provides information about the position and direction of the proton trajectory. However, the physically interesting information is that on the proton four-momentum at the interaction vertex. It is possible to unfold it from the trajectory measurements, because the relation between the momentum and the trajectory is invertible.

There is one complication in the inverting procedure – the proton position at the AFP station depends also on the position of the interaction point, which randomly changes due to the finite bunch widths and length. This could be a problem, because the transverse position of the interaction vertex can only be measured with precision comparable to the transverse beam size. Thus its constraint is quite weak. Fortunately, the dependence on the vertex position is small, thus it only gives a contribution to the unfolding resolution, not compromises it completely.

The unfolding procedure has been presented in [103]. The first step was to parametrise the transport with simple analytical formulae. The following parametrisation formula has been proposed:

$$\begin{aligned} x &= A_x + x'_0 B_x + x_0 C_x + x'_0 z_0 D_x + z_0 F_x, \\ y &= A_y + y'_0 B_y + y_0 C_y + y'_0 z_0 D_y + z_0 F_y, \\ x' &= A_{sx} + x'_0 B_{sx} + x_0 C_{sx} + x'_0 z_0 D_{sx} + z_0 F_{sx}, \\ y' &= A_{sy} + y'_0 B_{sy} + y_0 C_{sy} + y'_0 z_0 D_{sy} + z_0 F_{sy}, \end{aligned} \tag{5.3}$$

where (x, y) is the proton position in the first station, x' and y' are the vertical and horizontal elevation angles of the trajectory between the two stations, (x_0, y_0, z_0) is the interaction vertex position, x'_0 and y'_0 are the scattering angles of the proton outgoing from the IP. All the coefficients A to F are polynomials in ξ and were obtained by fitting the positions obtained using the FPTrack program. The order of the polynomials was taken as the smallest one that fulfils the assumed accuracy of the parametrisation. For the position parametrisation, x and y, it was requested to be a factor of 10 better than the respective detector resolution. For the parametrisation of the angles, x' and y', the accuracy was requested to be better than 0.1 μrad, which is by a factor of 10 better than the estimated effect of the multiple Coulomb scattering that leads to elevation angle smearing [104]. Results of the transport calculation performed using the parametrisation and the FPTrack program were compared using Pythia generated single diffractive events. The distribution of the differences between trajectory parameters obtained with these two methods were obtained. Figure 5.18 presents the worst of the obtained distributions for the positions and angles. One can see that the differences are indeed negligible with respect to the detector resolution and multiple scattering.

The parametrisation form shows an important feature of the LHC optics. For

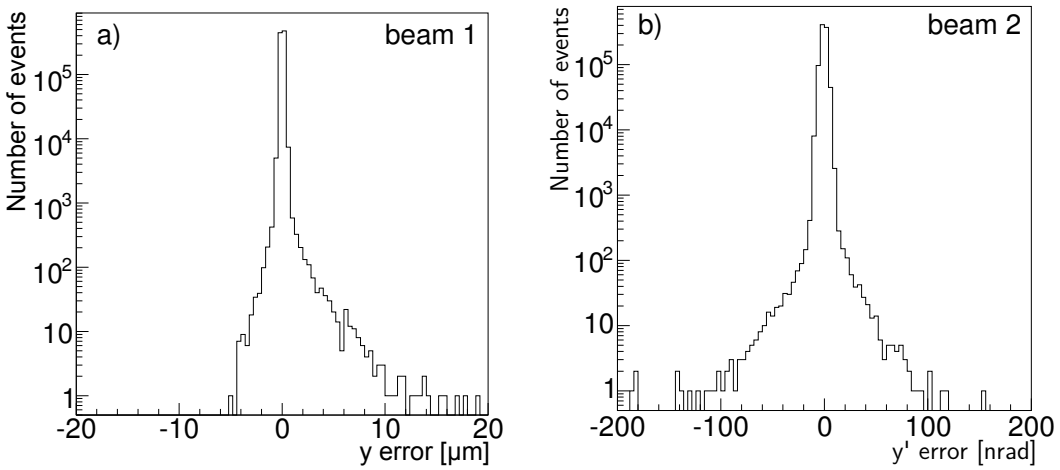

Figure 5.18: Examples of the parametrisation accuracy estimation (see text). Pictures show the accuracy on the y (left) and y' (right) parametrisation of beam 1 and beam 2 transport, respectively.

example, the horizontal position x and angle x' depend on ξ (through the coefficients A to F), x_0, x'_0 and z_0, while it does not depend on y_0 and y'_0. It is similar for the vertical variables y and y' that do not depend on x_0 and x'_0. This is due to the fact the LHC magnets can be, up to a very good accuracy, described only by the two leading magnetic moments, the dipole and the quadrupole one. If higher moments could not be neglected, one would have to consider a mixing between the horizontal and vertical coordinates.

Neglecting the dependence on x_0 and z_0, the horizontal position and angle at the AFP detectors position (x and x') depend only on ξ and x'_0. This dependence can be shown graphically on the chromaticity plot, see Figure 5.19 (left), where (x, x') points are drawn for protons with the same ξ and different x'_0 (iso-energy lines) as well as for protons with the same x'_0 and different ξ (iso-angle lines). This plot illustrates that the dependence between (ξ, x'_0) at the IP and (x, x') is a one-to-one correspondence within the acceptance range of the AFP detector and thus can be inverted. A similar situation occurs also for the vertical direction, see 5.19 (right).

It is worth noticing, see for example Figure 5.15, that the displacement in the horizontal direction is much more sensitive to the proton energy than the displacement in the vertical direction. This is also seen in Figure 5.19, where the distance between points corresponding to energy of 6 TeV and 7 TeV with no transverse momentum, $(6, 0)$ and $(7, 0)$, is much smaller for the horizontal direction. This distance corresponds to the change of trajectory due to the energy loss of 1 TeV. The greater such distance is, the easier it is to distinguish between two distinct energies.

Actually, the fact that the vertical position coordinate of protons with t equal to

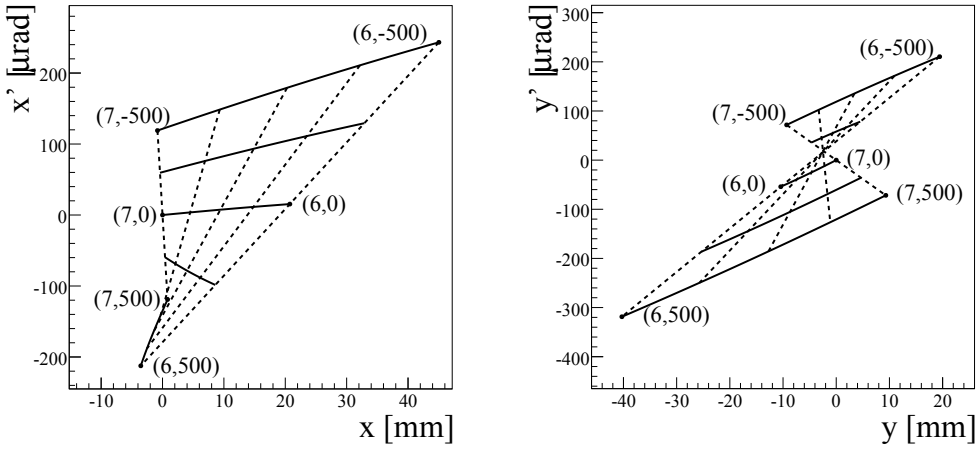

Figure 5.19: Chromaticity plots showing the dependence between the initial proton kinematics and its trajectory in the AFP. Axes of the plots describe the trajectory that is measured in the AFP: x and y are the positions x' and y' are the angles. Points marked on the plots describe the scattered proton kinematics: $(E,\ x'_0)$ in the left plot and $(E,\ y'_0)$ in the right plot, where E is the energy in TeV, while x'_0 and y'_0 are the scattering angles in μrad. Dashed and solid lines indicate trajectories of protons with constant energy and constant scattering angle, respectively. The lines of constant energy correspond to 7000, 6825, 6650, 6475, 6300 GeV from left to right, respectively. The lines of constant angle correspond to -500, -250, 0, 250 and 500 μrad respectively from top to bottom.

zero[5] can be different from zero, is only due to the existence of the beam *crossing angle* at the ATLAS IP, *i.e.* the fact than the two beams are tilted vertically at the IP. This implies that the nominal orbit does not coincide exactly with the magnetic axis of the final focussing LHC quadrupoles. This small mismatch is corrected further away from the IP. However, this correction works only for the protons with nominal (beam) energy. For protons originating from diffractive interactions, which have lost a part of energy, the correction will not remove the deviation. For dedicated machine tunes without crossing angle, all protons with $t = 0$ ($p_T = 0$) would remain in the accelerator plane ($y = 0$), independently of the energy loss.

From the measurements of position and angles in both directions, all the three components of proton momentum can be obtained assuming that the vertex position is known. Since the horizontal direction is more sensitive to the proton energy, one can unfold ξ and x'_0 only from the x and x' measurements, then use the y or y' measurements to obtain y'_0. The first step can be performed by solving numerically

[5]Actually, when the proton mass is not neglected, the four-momentum transfer cannot be equal exactly to zero. The mass is neglected in this calculation.

the following equation:

$$\frac{x - A_x - F_x z_0 - x_0 C_x}{B_x + z_0 D_x} = \frac{x' - A_{sx} - F_{sx} z_0 - x_0 C_{sx}}{B_{sx} + z_0 D_{sx}} \tag{5.4}$$

which can be obtained by a simple transformation of the first two parametrisation equations. The knowledge of the vertex position is assumed here. For a numerical solution, one of the simplest methods is chosen – searching for the zeros of the following function:

$$\begin{aligned} f(E) = &(x - A_x - F_x z_0 - x_0 C_x) \cdot (B_{sx} + z_0 D_{sx}) \\ &- (x' - A_{sx} - F_{sx} z_0 - x_0 C_{sx}) \cdot (B_x + z_0 D_x). \end{aligned} \tag{5.5}$$

It was observed that $f(E)$ has only one zero. Finding the zero of f was performed using the bisection method [105]. The procedure was tested using the same Pythia single diffractive sample as before. A very good agreement was found between the original and unfolded energy. The observed differences were negligible (below 0.01 GeV) and could be further reduced, if necessary, by increasing the rank of the polynomials used in the parametrisation.

In reality, the measurement cannot be that good due to various experimental effects. First of all, the AFP detectors have a finite spacial resolution (10 μm in x and 30 μm in y). Therefore, the measured trajectory parameters will differ from the true ones, which will lead to a difference between the true energy and the one reconstructed from the measurement. The second effect is the lack of knowledge about the transverse vertex position, x_0 and y_0 (however, in this method only the horizontal coordinate x_0 is important for the energy unfolding). The longitudinal component z_0 can usually be measured precisely with the ATLAS central detector. However, in the case when the proton comes from a soft pile-up interaction and accidentally fulfils the timing criteria, the z_0 position can be wrongly assigned. Therefore, it also makes sense to consider the effect of lacking this information. The last factor that can affect the reconstruction is the interaction of the proton with the first AFP station. Due to Coulomb multiple scattering effect, the proton trajectory direction can be altered [104]. It should be noted that hadron interactions with the first station material were not studied, since they affect the detector acceptance rather then the resolution.

The final resolution of the energy reconstruction is shown in Figure 5.20. In addition, the contributions due to different experimental effects are presented. For an energy of 6000 GeV, corresponding to the edge of the AFP acceptance, the total resolution is about 9 GeV and it decreases to about 3 GeV for protons at 6900 GeV, corresponding to the other edge. This could suggest resolution better than 1‰. However, one should have in mind that the detectors measurement is sensitive not to the proton energy, but to the energy loss (ΔE or ξ). For protons with $\xi = 0.15$

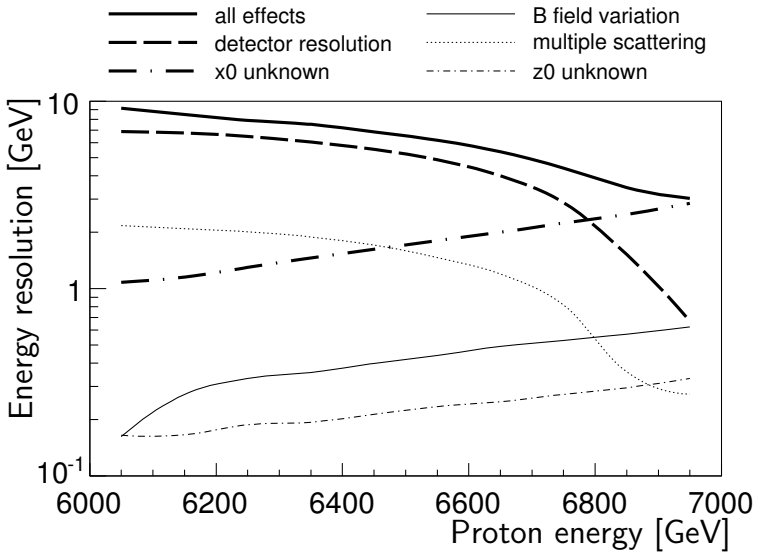

Figure 5.20: Proton energy reconstruction resolution for $beam1$ as a function of its energy. The overall resolution is indicated in thick solid line, the influence of the detector spatial resolution in thick dashed line, the vertex position in the transverse plane in thick dash-dotted line, the multiple Coulomb scattering in dotted line, the vertex position along the beam axis in dash-dotted line and the magnetic field variation in solid line.

($E \approx 6000$ GeV) the ξ resolution is about 1%, while for $\xi = 0.015$ ($E \approx 6900$ GeV) it is about 3%.

The dominant contribution to the high ξ reconstruction uncertainty is the detector spatial resolution. At small values of ξ, the lack of knowledge about the vertex transverse position becomes the most important effect. This was taken into account by taking $x_0 = 0$ in the unfolding procedure, while in the simulation the vertex was smeared with a Gaussian distribution of 12.7 μm, which corresponds to the transverse size of the beam spot. The other effects do not play a large role. This includes the variation of the B field, which was taken into account by changing the magnetic field of the LHC magnets used in FPTrack by $\pm 1‰$, while for unfolding using the original parametrisation obtained with unaltered magnets parameters. Actually, 1‰ is a rather large value, since it is by a factor of 10 larger than the accuracy accepted by the machine and by a factor of 50 larger than the measured values [106]. One can see that even such a large variation of the field would not affect the resolution. However, it does lead to a systematic offset of the reconstructed energy value – about 1 GeV at large ξ and about 0.1 GeV at small ξ, *i.e.* roughly a 1‰ offset (not shown in the plot). Of course, since this offset is a systematic effect, it should be possible to correct for it.

For processes in which both protons stay intact, one is interested in reconstructing the missing mass, M_X. For this case, additional factors can have a non-trivial effect on the resolution. In reality, the beam energy at the LHC has a Gaussian dis-

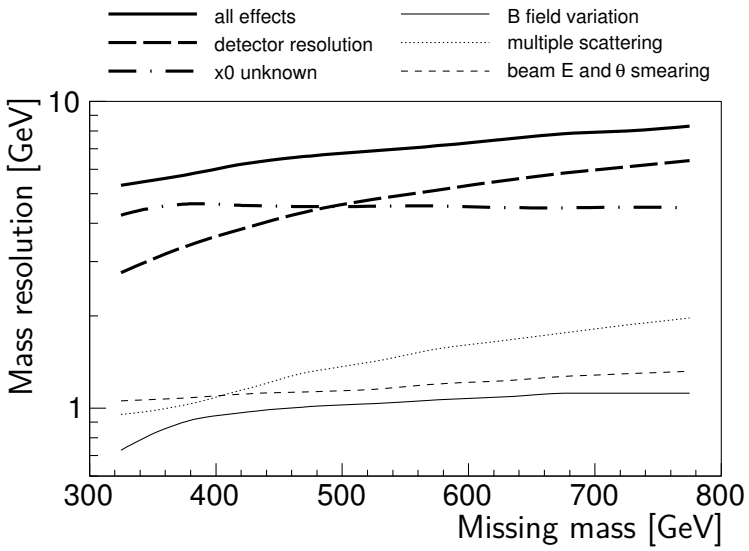

Figure 5.21: Missing mass resolution determined with outgoing protons as a function of the missing mass. The overall mass reconstruction resolution is indicated in thick solid line. The influence of different effects is presented: detector spatial resolution, vertex position in the transverse plane, multiple Coulomb scattering, magnetic field variation, the beam energy and the proton direction angular spreads.

tribution with a mean of 7 TeV and a width of 0.77 GeV (beam energy spread). A similar situation occurs also for the proton direction – at the ATLAS IP the angular spread in both horizontal and vertical directions is designed to be 32.2 μrad (beam angular spread). In order to reconstruct the missing mass one has to assume that the initial energy is equal to 7 TeV and the initial angles are zero[6], which affects the reconstruction.

Similarly to the acceptance case, the actual value of the M_X resolution will depend on the process considered and on the shape of ξ_1 and ξ_2 distributions. However, the differences will not be large. The following results have been obtained for events generated such that the ξ values of both protons follow a $1/\xi$ distribution, t is generated according to e^{-bt}, where $b = 6$ GeV^{-2} and the azimuthal angles are distributed uniformly.

Figure 5.21 shows the resolution of the missing mass reconstruction. The leading contributions originate from the detector resolution and the unknown value of the vertex x_0 position. The first one dominates at small masses, below 500 GeV. The latter one becomes dominant above this value. Other effects are negligible compared to these two. The total resolution, taking into account all contributions, increases from 5 GeV for $M_X = 300$ GeV to 8 GeV at $M_X = 800$ GeV. It should be emphasised that this represents the resolution for a single measurement. This is one of the key advantages of the AFP detectors. It leads to a very good background rejection for

[6]With respect to the nominal beam trajectory, which takes into account the beam crossing angle.

exclusive processes based on the compatibility of the mass measured in the central detector with the mass reconstructed from protons, as discussed before.

Chapter 6

Central Diffractive W Charge Asymmetry Measurement

Among all the Standard Model particles the only bosons with an electric charge are the W bosons: W^+ and W^-. Usually their production is studied together. For example one measures the cross section for W production, *i.e.* the sum of cross sections for W^+ and W^- production. When one is interested in differences between them, the charge asymmetry A is studied. It is defined as:

$$A = \frac{N_+ - N_-}{N_+ + N_-}, \tag{6.1}$$

where N_+ and N_- are respectively the number of W^+ and W^- particles produced in a given period of time. Measurements of the total W cross section and the asymmetry have one great advantage over measuring separately the cross sections for W^+ and W^-. Some of the experimental systematic errors are common for the W^+ and W^- particles, which means that they can cancel for the asymmetry measurement. This can lead to precise results.

Measurements of charge asymmetry of the W boson production at a pp collider can provide important information about the proton structure. Such data are used in determination of the parton distribution functions (PDFs) [107, 108, 109, 110, 111]. In particular, they are important for the light quarks distributions. This is because the W boson is produced in the annihilation of quark and anti-quark of different flavour with the dominant contributions of $u\bar{d} \to W^+$, $\bar{u}d \to W^-$ processes.

The W boson can be produced also in diffractive interactions, both in single and central diffractive processes. The single diffractive production has been already observed at the Tevatron (see Chapter 1), while the W production in central diffractive processes has not been observed yet. This may be possible at the LHC, where the

large luminosity gives the opportunity to measure small cross section phenomena. Such a measurement can be performed by tagging the forward protons with the AFP detectors to ensure the diffractive nature of the process. Measurements with the rapidity gap method is impossible, because the expected gap sizes in this process are too small to be observed with the LHC detectors.

The measurement of charge asymmetry in the central diffractive W production processes can shed light on the mechanism of the hard diffractive production. For example, in the resolved Pomeron model of diffraction [112, 113] the Pomerons exchanged in the process exhibit their partonic structure. The quarks annihilating into W bosons originate from the Pomerons. On the other hand, in the Soft Colour Interaction models [114] the quarks originate from the protons and the diffractive signature emerges as the effect of soft gluon exchanges that neutralise colour in the rapidity space between the protons and the central system [115, 116].

These two approaches lead to different predictions for W charge asymmetry in the central diffractive processes. In the resolved Pomeron model, the quark distributions in the Pomeron are both charge and flavour symmetric, in order to account for the quantum numbers of the Pomeron. In this case the expected asymmetry is exactly equal to zero. In the SCI approach, the asymmetry is expected to be the same as in non-diffractive W production. For a centre-of-mass energy of 14 TeV the predicted asymmetry is about 0.14.

The measurement of the production cross section for central diffractive W production can constrain the diffractive PDFs. However, such measurement can have large uncertainties both theoretical, especially due to the gap survival probability, and due to various experimental effects. A much cleaner way is to measure also the central diffractive Z production and use the W/Z cross section ratio. This is particularly interesting, because it allows tests of the light flavour symmetry of the Pomeron, which has never been studied before.

The work presented in this chapter was partially published in Phys. Rev. D84 (2011) 114006 and ATL-COM-PHYS-2012-775.

6.1 W Boson Charge Asymmetry

The kinematics of non-diffractive W production is given by the momenta of the quarks producing the W boson. In the collinear approximation, the fractional momenta of quarks, x_1 and x_2, are connected to the boson rapidity, y, and mass, M_W:

$$x_1 = \frac{M_W}{\sqrt{s}}\mathrm{e}^{y}, \qquad x_2 = \frac{M_W}{\sqrt{s}}\mathrm{e}^{-y}, \tag{6.2}$$

where $\sqrt{s}$ is the centre-of-mass energy. Since M_W is fixed (the width of the boson can be neglected), there is only one independent variable, namely the rapidity, y. The maximal energy available in the process leads to the constraints on the W boson

rapidity:

$$|y| < \ln \frac{\sqrt{s}}{M} \approx 5.2, \tag{6.3}$$

where the numerical value is given for $\sqrt{s} = 14$ TeV.

The cross sections for W^+ and W^- production is approximately equal to [117]:

$$\frac{\mathrm{d}\sigma_{W^+}}{\mathrm{d}y} = \frac{2\pi G_F M_W^2}{3\sqrt{2}s}|V_{ud}|\Big[u(x_1, M_W^2)\bar{d}(x_2, M_W^2) + u(x_2, M_W^2)\bar{d}(x_1, M_W^2)\Big], \tag{6.4}$$

$$\frac{\mathrm{d}\sigma_{W^-}}{\mathrm{d}y} = \frac{2\pi G_F M_W^2}{3\sqrt{2}s}|V_{ud}|\Big[d(x_1, M_W^2)\bar{u}(x_2, M_W^2) + d(x_2, M_W^2)\bar{u}(x_1, M_W^2)\Big], \tag{6.5}$$

where G_F is the Fermi constant, while $u(x, Q^2)$, $\bar{u}(x, Q^2)$, $d(x, Q^2)$, $\bar{d}(x, Q^2)$ denote the PDFs for the respective quarks and V is the CKM matrix. The formulae take into account only the leading contributions: $u\bar{d} \to W^+$, $\bar{u}d \to W^-$. In reality, an important contribution comes also from processes involving the s quark: $u\bar{s} \to W^+$, $\bar{u}s \to W^-$. This contribution is not shown in the above formulae, but is present in the calculations. Figure 6.1 (left) shows the cross sections for W^+ and W^- production as a function of the boson rapidity. In addition, the cross section for the Z boson production is presented and it can be obtained in a similar way.

The rapidity dependent charge asymmetry is defined as:

$$A_{ND}(y) = \frac{d\sigma_{W^+}/dy - d\sigma_{W^-}/dy}{d\sigma_{W^+}/dy + d\sigma_{W^-}/dy}\,. \tag{6.6}$$

Taking into account eq. 6.4 and 6.5 and the simplifying assumption that the sea quark distributions are equal ($\bar{u} = \bar{d}$) it can be written as:

$$A_{ND}(y) = \frac{\Big[u(x_1) - d(x_1)\Big]\,\overline{u}(x_2) \;+\; \overline{u}(x_1)\,\Big[u(x_2) - d(x_2)\Big]}{\Big[u(x_1) + d(x_1)\Big]\,\overline{u}(x_2) \;+\; \overline{u}(x_1)\,\Big[u(x_2) + d(x_2)\Big]}\,, \tag{6.7}$$

where x_1 and x_2 are functions of y, eq. (6.2), and the scale of PDFs is not written explicitly (it is equal to M_W^2 in all cases).

The non-zero value of the asymmetry comes from the fact that the u and d quark distributions are different. This is also the reason why the charge asymmetry measurements can be used to constrain the parton distributions. The charge asymmetry as a function of the W rapidity is presented in Figure 6.1 (right). Although the asymmetry values are quite large (up to the maximal value of 1) one needs to remember that the production is strongly suppressed for rapidity absolute values greater than 3.5 (see Figure 6.1, left). Eventually, the average value of the asymmetry equals about 0.14.

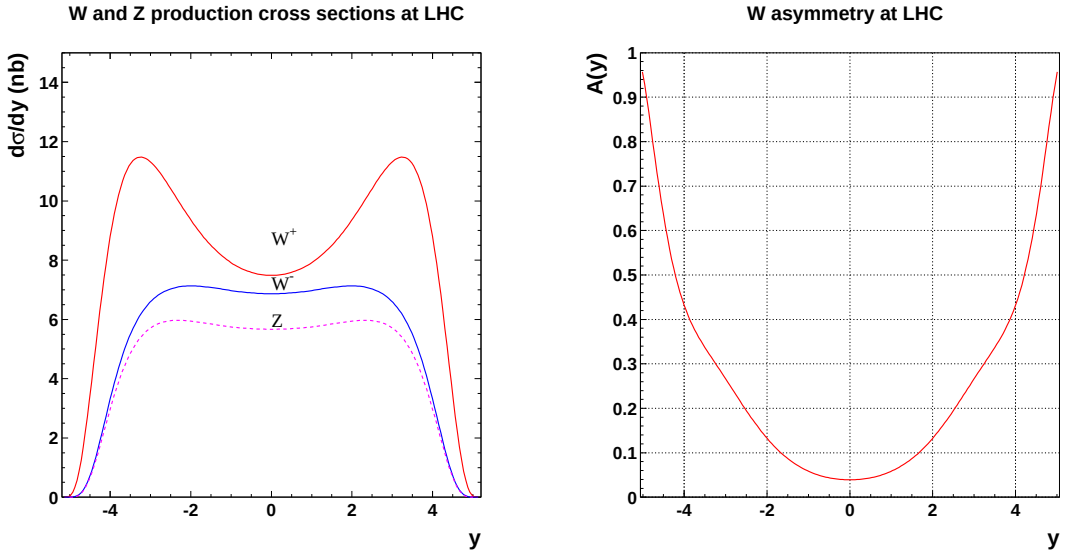

Figure 6.1: W and Z boson production cross sections for $\sqrt{s} = 14$TeV as a function of the boson rapidity y (left) and corresponding W boson rapidity asymmetry (right) for the LO MSTW08 [118] parton distributions.

6.2 Central Diffractive W Production

In the non-diffractive W production the only independent variable was the W rapidity. In the central diffractive case, where protons are intact, additional degrees of freedom are available. The most important ones are the fractional energy losses of the scattered protons, ξ_1 and ξ_2, which to a good approximation can be interpreted as the momentum fractions carried by two Pomerons involved in the process. The centrally produced mass, $M_X = \sqrt{s \cdot \xi_1 \cdot \xi_2}$, must be greater than the boson mass, M_W (neglecting the W width). Also, the momentum fractions of the quarks cannot be larger than the respective momentum fractions of the Pomerons:

$$x_1 < \xi_1, \qquad x_2 < \xi_2. \tag{6.8}$$

This leads to the constraint on the W rapidity:

$$-\ln\frac{\sqrt{s}}{M_W} - \ln\xi_2 < y < \ln\frac{\sqrt{s}}{M_W} + \ln\xi_1. \tag{6.9}$$

The cross sections for the W production can be calculated similarly to the non-diffractive case. However, instead of standard PDF, one has to use diffractive PDFs (DPDFs):

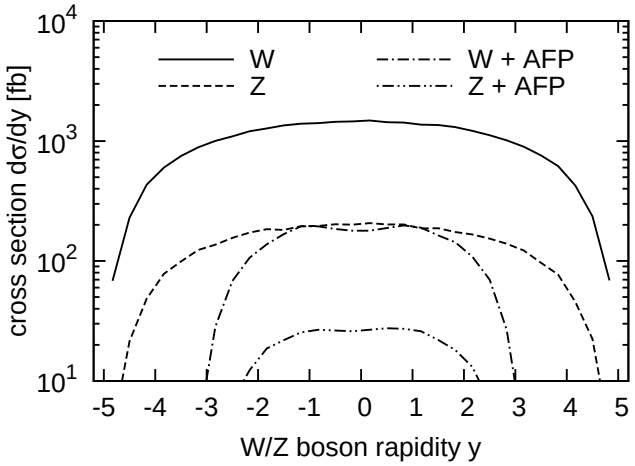

Figure 6.2: Diffractive W and Z boson production cross sections as a function of rapidity in the DPE model with and without taking into account the AFP acceptance computed using the FPMC generator.

$$\frac{\mathrm{d}\sigma_{W^+}}{\mathrm{d}y\mathrm{d}\xi_1\mathrm{d}\xi_2} = S^2\frac{2\pi G_F M_W^2}{3\sqrt{2}s}\Big[u_D(x_1,M_W^2)\bar{d}_D(x_2,M_W^2) + u_D(x_2,M_W^2)\bar{d}_D(x_1,M_W^2)\Big], \tag{6.10}$$

$$\frac{\mathrm{d}\sigma_{W^-}}{\mathrm{d}y\mathrm{d}\xi_1\mathrm{d}\xi_2} = S^2\frac{2\pi G_F M_W^2}{3\sqrt{2}s}\Big[d_D(x_1,M_W^2)\bar{u}_D(x_2,M_W^2 + d_D(x_2,M_W^2)\bar{u}_D(x_1,M_W^2)\Big]. \tag{6.11}$$

The additional factor S^2 is the gap survival probability, which takes into account the possibility of destroying the diffractive signature by a soft interaction. For a centre-of-mass energy of 14 TeV the value of 0.03 is assumed for S^2 [50]. Figure 6.2 presents the cross section for W production integrated over $0 \leq \xi_1, \xi_2 \leq 1$ (the full possible range) and and $0.02 < \xi_1, \xi_2 < 0.14$ (the approximate AFP acceptance range). In addition, the cross sections for Z production are shown in this figure. One can see that the requirement of having both scattered protons tagged in the AFP detectors reduces the cross section by about one order of magnitude. The allowed W rapidity range is reduced from $|y| < 5$ to $|y| < 3$. The reason of this is that the AFP detectors have considerable acceptance for events with missing mass of few hundreds GeV, which is much higher than the W mass. Therefore, W events in which remnants of the Pomerons carry small energy cannot be detected. This could be much improved by installing the AFP420 detectors, which will be sensitive to smaller mass values.

The charge asymmetry in the case of central diffractive production can be treated not only as a function of y, but also of ξ_1 and ξ_2. Due to the fact the Pomeron carries the vacuum quantum numbers, the diffractive PDFs need to be both charge and light flavour symmetric. Actually, it is enough to assume the charge symmetry, $u_D = \overline{u}_D$

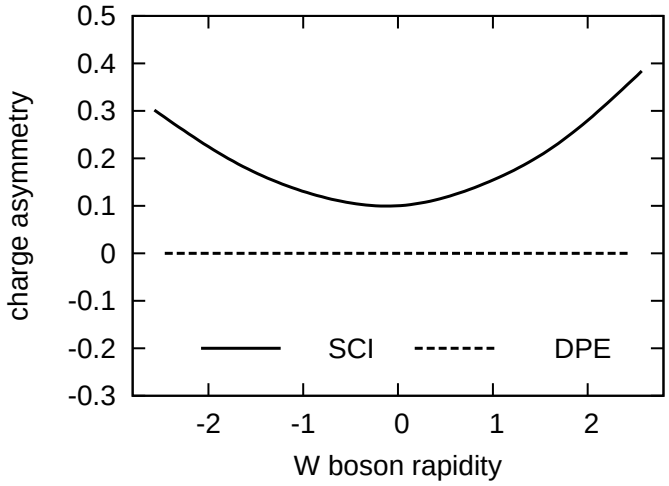

Figure 6.3: Charge asymmetry in central diffractive W production process as a function of the W boson rapidity y. Two cases are presented: DPE – the process is governed by the Pomeron mechanism, SCI – the process is governed by Soft Colour Interactions mechanism.

and $d_D = \overline{d}_D$, to obtain the expected value of the asymmetry:

$$A_D(y, \xi_1, \xi_2) = 0\,, \tag{6.12}$$

which is y, ξ_1 and ξ_2 independent.

In the case of the Soft Colour Interaction approach, the processes leading to the diffractive structure of the event, with two intact protons, happen after the hard interaction of the W boson production. Therefore, the asymmetry should be equal, or very close, to the asymmetry in the non-diffractive production. This has been confirmed with Monte Carlo predictions [119]. The obtained asymmetry is presented in Figure 6.3 and compared to the prediction of the Pomeron model. The difference between these two predictions is quite substantial. The asymmetry measurement can be thus used for testing the mechanism of hard diffractive interactions. A good observable for such a test is the asymmetry integrated over the W rapidity. Such a measurement is much easier, since the W rapidity is not directly accessible experimentally[1]. For the Pomeron model it is expected to be 0, while for SCI about 0.14. It should be mentioned that recent, preliminary results [120] show that in some SCI Monte Carlo implementations, other than the one used for this study, the asymmetry similar to non-diffractive production is not observed. The details are still not well understood and are being investigated.

[1]Measurements in the hadronic channel are impossible due to the overwhelming QCD background. In the leptonic channel, the transverse coordinates of the neutrino momentum is determined via the missing transverse energy, while the longitudinal coordinate remains unknown. This leads to two possible solutions for the W rapidity.

6.3 W/Z Cross Section Ratio

Additional information about the diffraction mechanism can be obtained from the measurements of the Z boson production cross section. A particularly interesting observable is the ratio of the cross sections for the W and the Z boson production. This is because, for such measurements, many of the sources of systematic uncertainty are the same and cancel in the final result.

The cross section for central diffractive Z production can be calculated using the diffractive parton distributions:

$$\begin{aligned}\frac{d\sigma_Z}{dy} = \frac{2\pi G_F M_Z^2}{(3\sqrt{2}s)}\Big[&C_u u_D(x_1')\,\overline{u}_D(x_2') \;+\; C_d d_D(x_1')\,\overline{d}_D(x_2') \\ &+ C_u u_D(x_2')\,\overline{u}_D(x_1') \;+\; C_d d_D(x_2')\,\overline{d}_D(x_1')\Big]\end{aligned} \tag{6.13}$$

where $C_{ud} = V_{ud}^2 + A_{u,d}^2$ where $V_{ud} = T_{ud}^3 - 2Q_{ud}\sin^2\theta_W$ and $A_{ud} = T_{ud}^3$ are the vector and axial couplings of u and d quarks to Z boson and θ_W is the Weinberg angle. The scale of the PDFs is not written explicitly and is taken at $Q^2 = M_Z^2$. Similarly to the W boson case, the momentum fractions x_1' and x_2' are functions of the Z rapidity, y:

$$x_1' = \frac{M_Z}{\sqrt{s}}\mathrm{e}^{y}, \qquad x_2' = \frac{M_Z}{\sqrt{s}}\mathrm{e}^{-y}. \tag{6.14}$$

The ratio of W over Z cross sections reads:

$$\begin{aligned}R_{\mathrm{incl}}(y) \;=&\frac{M_W^2|V_{ud}|^2}{M_Z^2}\Big[u_p(x_1)\,\overline{d}_D(x_2) + \overline{d}_D(x_1)\,u_D(x_2) + d_D(x_1)\,\overline{u}_D(x_2) \\ &+ \overline{u}_D(x_1)\,d_D(x_2)\Big]\Big/\Big[C_u u_D(x_1')\,\overline{u}_D(x_2') + C_d d_D(x_1')\,\overline{d}_D(x_2') \\ &+ C_u u_D(x_2')\,\overline{u}_D(x_1') + C_d d_D(x_2')\,\overline{d}_D(x_1')\Big],\end{aligned} \tag{6.15}$$

where in the numerator the distributions are taken at the scale $Q^2 = M_W$ and $x_{1,2} = M_W\mathrm{e}^{\pm y}/\sqrt{s}$, while in the denominator $Q^2 = M_Z$ and $x_{1,2}' = M_Z\mathrm{e}^{\pm y}/\sqrt{s}$.

Assuming the flavour and charge symmetry of the DPDFs, and neglecting the difference between W and Z masses, the ratio is a constant function:

$$R_D(y, \xi_2, \xi_2) \;\approx\; \frac{M_W^2|V_{ud}|^2}{M_Z^2}\frac{1}{C_u + C_d}\,. \tag{6.16}$$

However, the light flavour symmetry of the Pomeron has never been tested experimentally. The DPDF fits performed by the HERA experiments [121, 122] always assumed $u_D = d_D = s_D$ since this is a natural assumption accounting for the vacuum quantum numbers exchanged in diffractive interactions. The HERA data cannot differentiate between the light flavours and effectively constrain only their

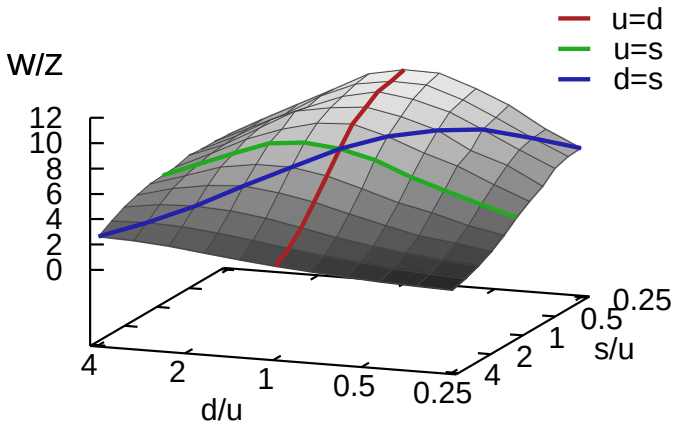

Figure 6.4: Effect of varying the d/u and s/u quark density ratios in the Pomeron on the W/Z cross section ratio keeping $u + d + s$ constant.

sum $u_D + d_D + s_D$. The measurement of the W over Z cross section ratio will allow to probe the different contributions.

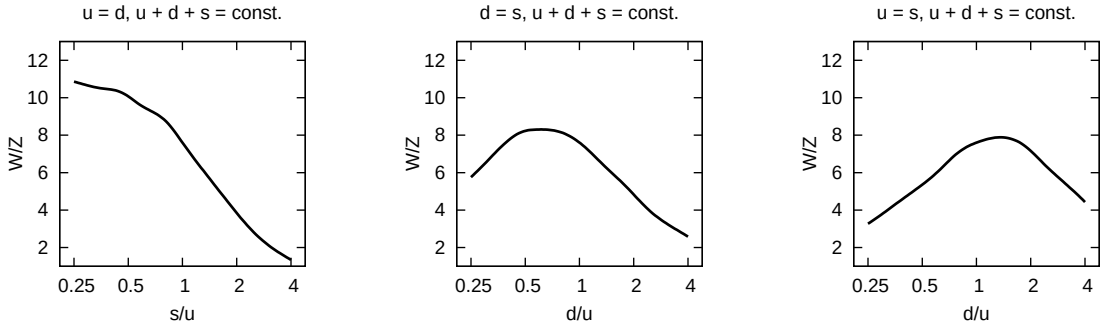

Figure 6.5: Effect of varying the d/u (resp. s/u and d/u) quark density ratio on the W/Z cross section ratio keeping $u + d + s$ constant and assuming $d = s$ (resp. $u = d$, $u = s$).

This can be seen in Figures 6.4 and 6.5, where the W/Z cross section ratio as a function of flavour composition is shown. The plots were obtained with the FPMC generator with diffractive PDFs modified by multiplying them by a constant factors (*i.e.* not depending on x and Q^2) in such a way, that their sum stays constant. This leaves two independent variables that describe the flavour composition, namely the d/u and s/u quark ratios (however, a different choice would be also correct). In this study the ratios were varied by a factor 4, up and down. This might seem a large factor, but one should remember that presently there are no constraints on these values. Figure 6.4 shows how the W/Z cross section varies as a function of d/u and s/u. In addition, three lines, corresponding to situations where two distributions

are equal, are depicted. In order to present the results in a more precise way, these three lines are shown in the two-dimensional plots in Figure 6.5. One can see that the variations are quite large. Therefore, the measurement of the W/Z cross section ratio can lead to constraints on quark diffractive PDFs.

6.4 ATLAS Simulation and Pile-up Treatment

In order to obtain reliable predictions for the possibility of central diffractive W measurements with AFP detectors, the following study has been performed on MC samples that were processed through the full ATLAS detector simulation. The event generation is performed in four main steps. The first one is the MC *generation*, where for each event a set of particles with their momenta is produced. The second step is the detector *simulation*, where interactions between the produced particles and the material of the ATLAS detector is simulated. This results in energy deposits in the detector. In the third step, called *digitisation*, the response of the detector electronics is simulated. As the result, one obtains data similar to the those from a real measurement. The last step is processing the event through the *reconstruction* software in order to extract meaningful information, like tracks, particles, *etc.*

An important issue in the generation chain is the treatment of pile-up events. Of course, in order to obtain events that agree with measured data, pile-up must be included in the simulation. This is performed by running the detector simulation separately on generated minimum bias data. The generator used is Pythia 8 tuned to describe the minimum bias measurement at $\sqrt{s} = 7$ TeV [6]. In fact, a large sample of pile-up events is used for all production at a given energy. The energy deposits from these events are then added to the hard event deposits before the digitisation step.

During the event generation, the generator level information (MC truth) about the hard interaction is passed on at each step. On the other hand, for pile-up events, the list of particles and their momenta is not kept in order to save storage space. This led to problems for AFP analyses, since by the time of writing this thesis the AFP detectors had not yet been fully included in the ATLAS simulation framework. Therefore, the information about forward protons coming from pile-up events and scattered into the beam pipe is lost. Fortunately, for hard events it is still available among the MC truth.

The correct way of dealing with this problem would require a proper implementation of the AFP detectors into the geometry model of ATLAS. This is being done presently, but, was not available at the moment of this analysis. Thus, a different approach has been taken. It consisted of three main steps described below.

1. Perform a standard ATLAS simulation of a hard event with pile-up. Information about forward protons originating from hard interaction is present in

MC truth. During the standard processing information about forward protons from all minimum bias interactions is not stored.

2. Generate minimum bias events independently (only generator-level events).
3. To each minimum bias interaction in pt. 1 "add" protons from one event from pt. 2. For each proton perform the FPTracker transport with vertex position coming from pt. 1. If the proton is within the AFP acceptance, the measurement (the response of the position and timing detectors) is simulated according to the appropriate Gaussian distributions.

Such a procedure has a major drawback – the correlation between the features of the pile-up events and the forward protons is completely lost, *i.e.* the events that were passed to digitisation can be different than the events from which the protons were taken. It has also a great advantage – very easily one can produce a sample that is preselected requesting a single or double tag in AFP, without loosing events simulated in pt. 1. This is done by repeating pt. 3 until the requested criteria are fulfilled.

The preselection is especially useful for non-diffractive samples and small values of pile-up multiplicity. In that case, only very few events would normally fulfil the double tag criteria, which would lead to a loss of the majority of simulated events. Using the preselection, all the available statistics can be used for the analysis. It must be emphasised that such a special treatment regards only the pile-up protons. The protons coming from hard interactions are kept in the simulation.

6.5 Monte Carlo Samples

The main backgrounds to the measurements of central diffractive production of the W boson are the non-diffractive and single diffractive W production with additional pile-up protons tagged in AFP. For this study, two sets of event samples were generated: with an average pile-up multiplicity, μ, equal to one and three. This is because $\mu = 1$ is the value for which the frequency of events without pile-up is the highest[2], whereas $\mu = 3$ has been estimated to be optimal in the early stage of this analysis, when only the non-diffractive background was considered and is kept here for reference.

The study has been done only for the W boson decaying into muons. As mentioned before, preselected samples have been used in the analysis, when appropriate. Since there are two possible preselections, there are three types of samples: NP – not preselected, ST – preselected on a single tag and DT – preselected on double tag. Table 6.1 presents the samples used in the analysis with their respective cross sections. Six different samples were used: non diffractive W production with NP,

[2]This is also useful for other analyses, *e.g.* precision measurements in electro-weak sector.

ST and DT preselections, single diffractive with NP and ST preselection and central diffractive with NP preselection. The single diffractive samples consist of two sub-samples with intact protons going in each direction. In the following they are presented together.

Figure 6.6 shows the distribution of muon transverse momentum after the W boson selection and the request of double AFP tag. The distributions of the three non-diffractive and two single diffractive samples are compatible, which confirms the correctness of the procedure. One can also clearly see the higher statistics of the preselected samples.

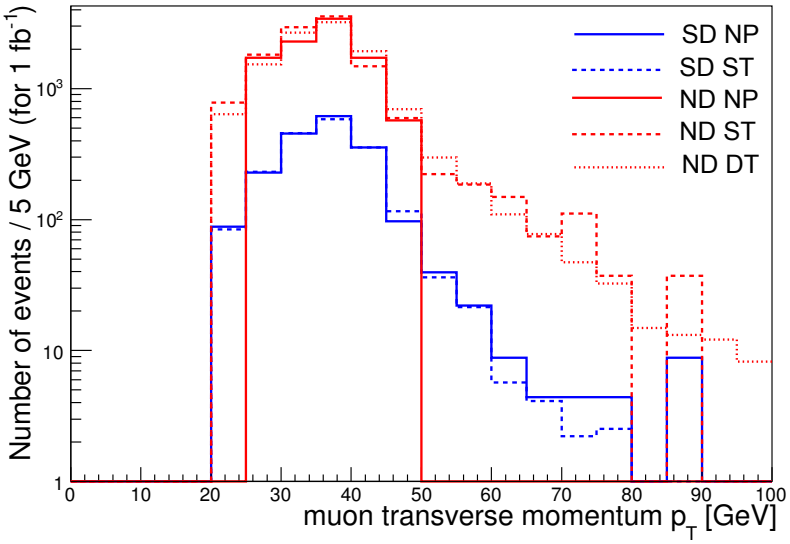

Figure 6.6: Distributions of muon transverse momentum after the requirement on the W selection and the AFP double tag for samples of non-diffractive and single diffractive production with different preselections.

Table 6.1: Cross sections for the MC samples of W production used in the analysis. ND – non-diffractive, SD – single diffractive, CD – central diffractive; NP – no preselection, ST – preselection on single tag, DT – preselection on double tag (as explained in the text).

Process	ND			SD		CD
Preselection	NP	ST	DT	NP	ST	NP
σ	20 nb	1.3 nb	17 pb	220 pb	16 pb	3.5 pb

6.6 Signal Selection

The signal selection for central diffractive W production will consist of two major parts. The reason for this is that there are two types of backgrounds for the process. The first one comes from QCD jets, which can sometimes mimic the W production. The second one is a true W production process, however not central diffractive.

In order to ensure that the events contain W bosons decaying into muons the following requirements are applied:

- presence of at least one reconstructed muon, satisfying the *medium* identification criteria (see Chapter 3),
- muon track isolation – the sum of the transverse momenta of tracks within a cone of radius $\sqrt{\Delta\phi^2 + \Delta\eta^2} < 0.2$ around the muon momentum direction must be less then 10% of the muon p_T,
- the transverse momentum of the muon is required to be greater than 20 GeV,
- the missing transverse energy must be greater then 25 GeV,
- the transverse mass, calculated as

$$m_T = \sqrt{2p_T^\mu p_T^\nu \left(1 - \cos(\phi^\mu - \phi^\nu)\right)}, \tag{6.17}$$

  must be greater then 40 GeV (p_T^μ and p_T^ν are the transverse momenta of the muon and the neutrino, ϕ^μ and ϕ^ν are their azimuthal angles; the neutrino momentum components are given by the measured missing transverse energy).

The above requirements follow the standard ATLAS W selection. It has been shown that they remove the great majority the non-diffractive QCD background, which becomes negligible compared to non-diffractive W production [123]. However, one needs to check whether this is still true for central diffractive production, where the W production is suppressed with respect to the jet production, because the Pomeron consists mainly of gluons and its quark content is small.

Table 6.2: QCD samples used in the analysis. k_T denotes the transverse momentum of the final-state partons.

Sample	k_T **range**	**Cross section**	**Number of events**
J2	$25 < k_T < 70$	31.0 nb	100000
J3	$70 < k_T < 140$	1.6 nb	50000
J4	$140 < k_T < 280$	60 pb	90000
J5	$280 < k_T$	1.4 pb	10000

Four QCD samples of central diffractive jets were used for this analysis, see Table 6.2. The samples are characterised by different, but complementary, ranges

of transverse momenta of partons fragmenting into jets. This gives a possibility to study all ranges of jet transverse momenta, using reasonable statistics of generated events. The samples with parton transverse momenta smaller that 25 GeV were not used in the analysis, since jets in these samples have the energy much too small to fake the W events.

The W selection cuts presented above proved to be effective in removing the central diffractive QCD background. The available statistics was satisfactory to claim that this background is negligible for the considered measurement. However, a precise determination of the selection efficiency was not possible. In fact, only four events passed the cuts: one event from the J3 sample, one from J4 and two from J5. This results in a visible cross section that is about two orders of magnitude smaller than the one for central diffractive W production. Figures 6.7, 6.8 and 6.9 present the distributions of few variables that are used in the W selection (muon transverse momentum, missing transverse energy and transverse mass, respectively) at consecutive stages of the W selection procedure. They clearly demonstrate the power of the QCD background rejection.

The second part of the selection aims at the selection of the central diffractive signal out of the non-diffractive and single diffractive background. For this, one needs the AFP detectors to tag the forward protons. In non-diffractive events such protons come most often from pile-up events. For single diffractive production one of them is from pile-up, the second one from the hard interaction. This does not always have to be the case, *e.g.* in a single diffractive event the proton from hard interaction can be outside the AFP acceptance, but be accompanied by two minimum bias interactions, both giving protons tagged in AFP.

In the generated single diffractive W production sample quite interesting events were observed. Even though they are of single diffractive nature, they have a double AFP tag. This is due to the proton remnant fragmenting into a proton, which in turn falls into the AFP acceptance. These events consist about 0.3% of the initial sample. However, this fraction increases due to the analysis selection, since the events pass the double tag and timing cuts in a natural way. On the other hand, the additional protons are not of diffractive origin. Therefore, their distributions of ξ and t are not as steep as for the diffractive ones. This can be deduced from the positions of these protons in the AFP detectors, presented in Figure 6.10. The protons originating from protons remnants populate more often the region of high x values and their vertical spread is larger.

Obviously, the above predictions of the MC generator are not very reliable. This is because the fragmentation effects in generators are based on phenomenological models fitted to data at relatively low centre-of-mass energies. Any extrapolations of the models into a new regime, for which no data are available, have large uncertainties. Therefore, it would be very interesting to measure this effect.

The AFP detectors are capable of not only the position measurement of the

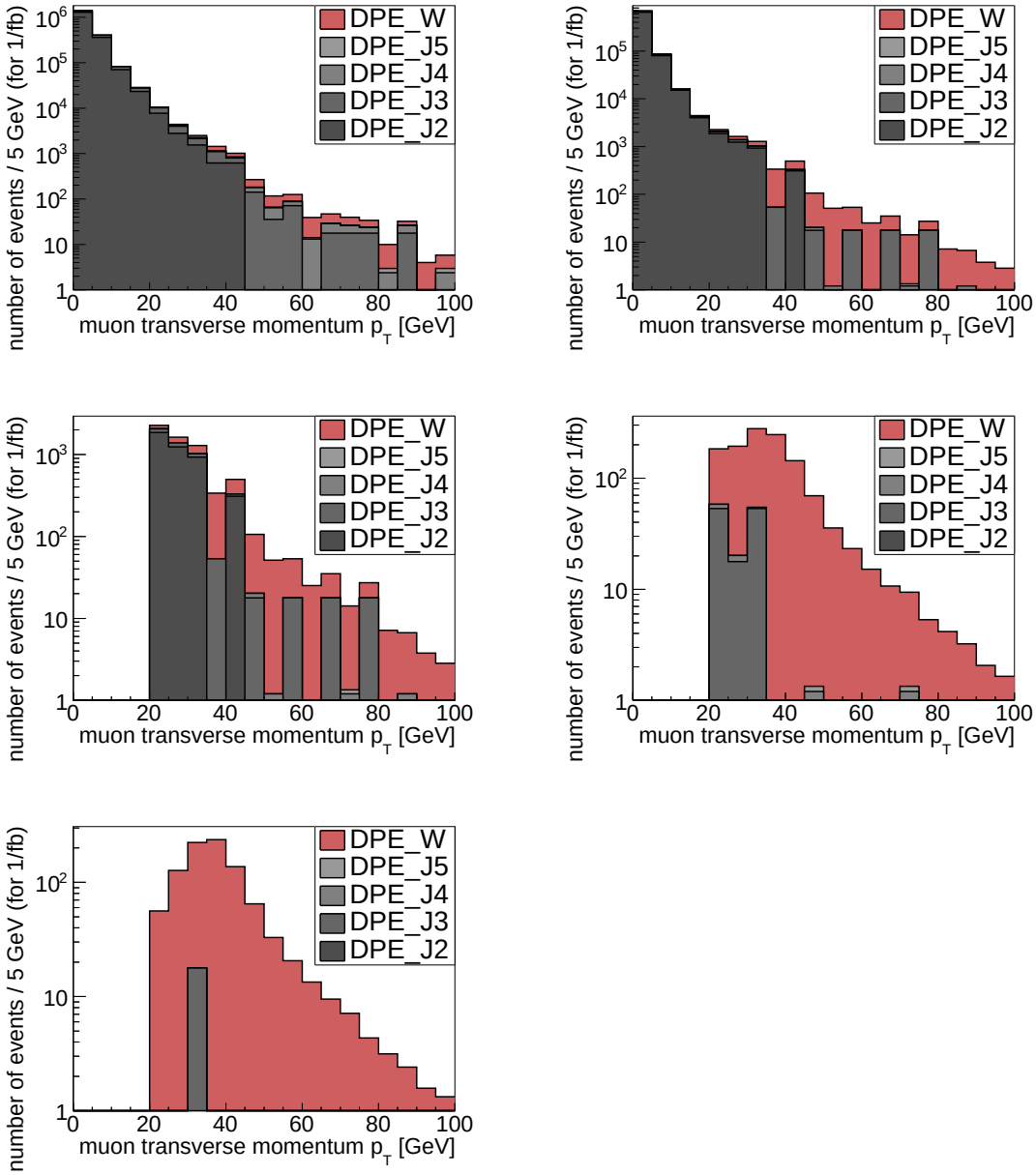

Figure 6.7: Distributions of the muon transverse momentum after the consecutive requirements of the W analysis: muon reconstruction and identification (1st plot), muon isolation (2nd plot), muon p_T (3rd plot), MET (4th plot) and transverse mass (5th plot).

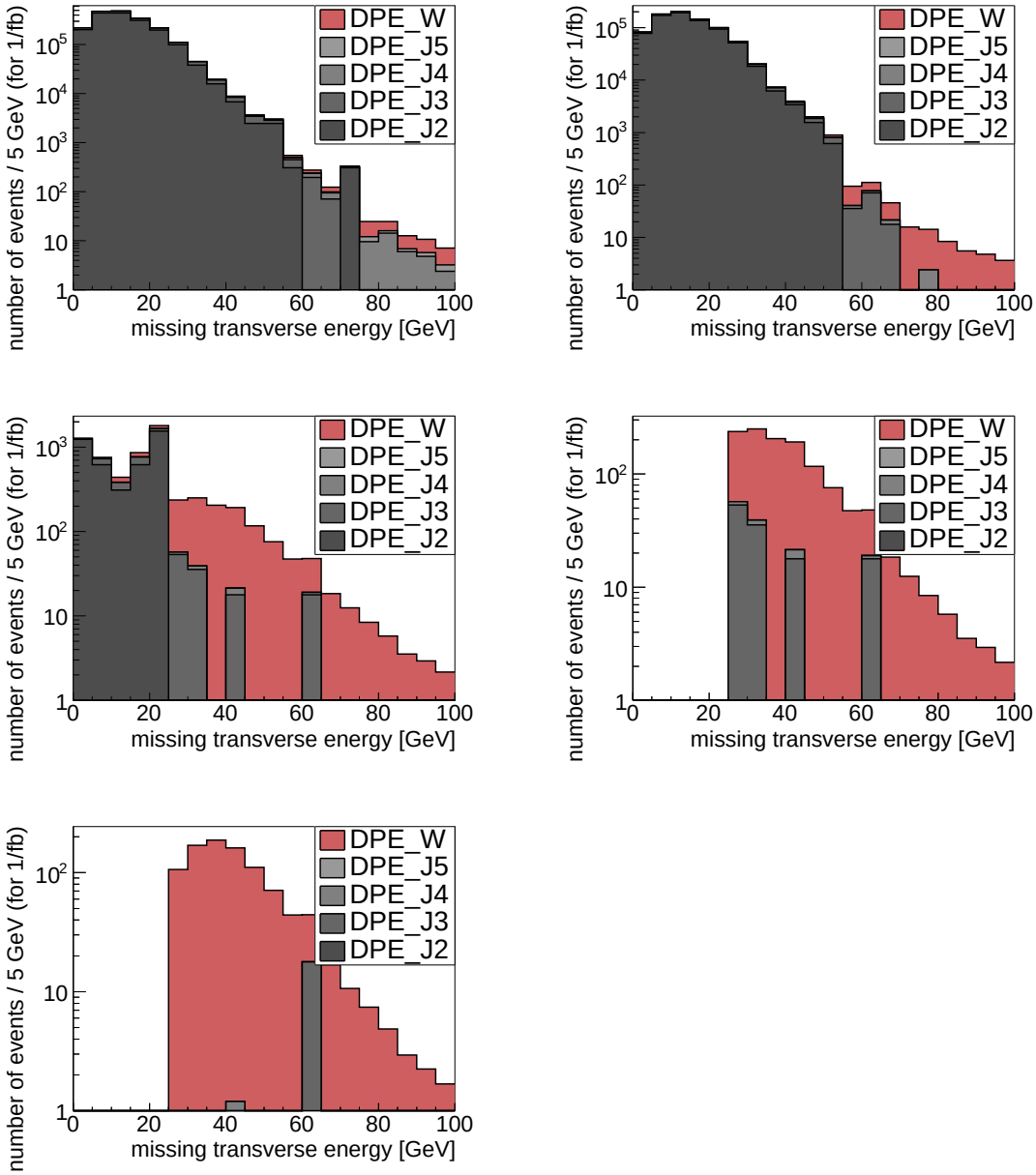

Figure 6.8: Distributions of the missing transverse energy after the consecutive requirements of the W analysis: muon reconstruction and identification (1st plot), muon isolation (2nd plot), muon p_T (3rd plot), MET (4th plot) and transverse mass (5th plot).

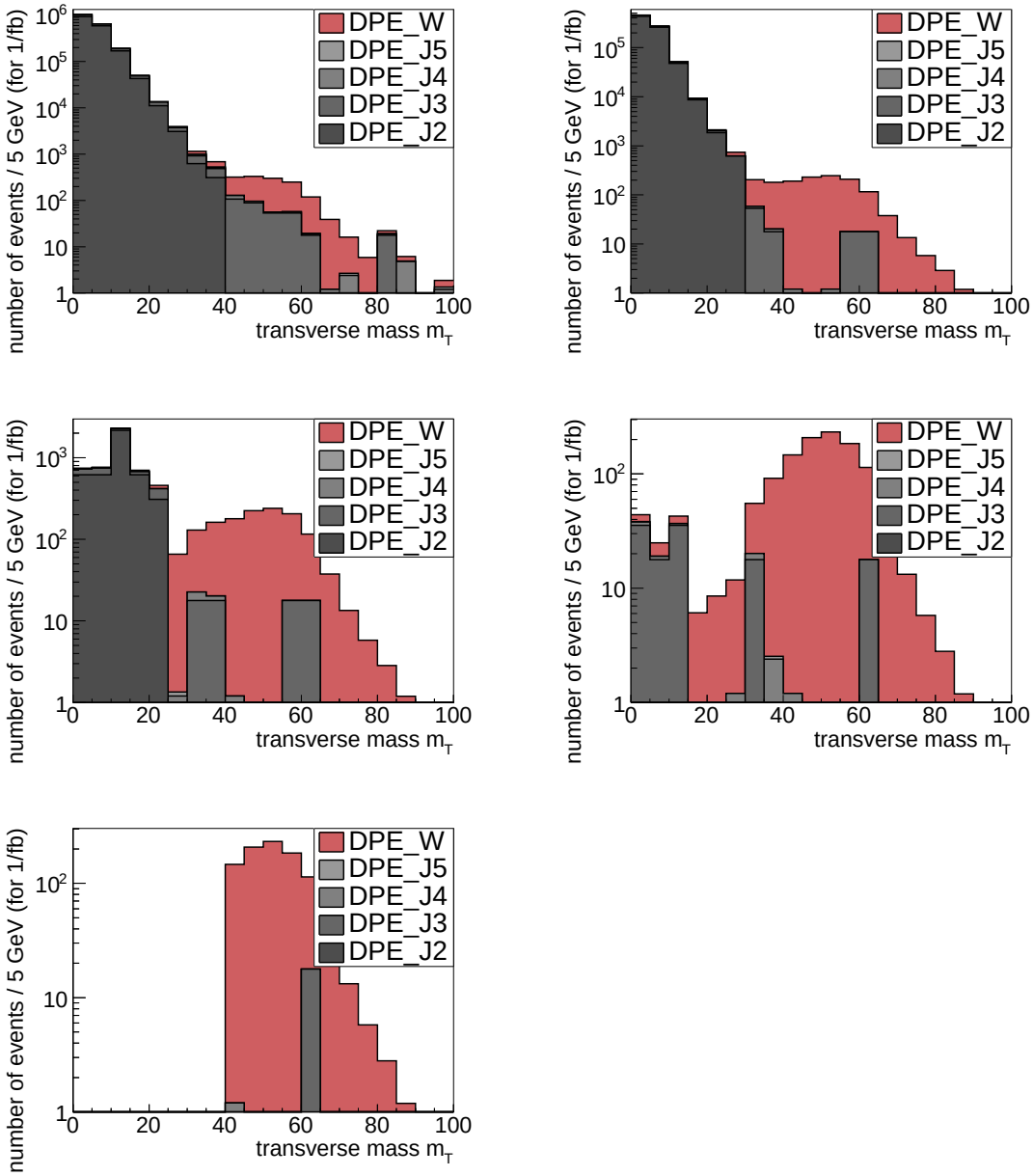

Figure 6.9: Distributions of transverse mass after the consecutive requirements of the W analysis: muon reconstruction and identification (1st plot), muon isolation (2nd plot), muon p_T (3rd plot), MET (4th plot) and transverse mass (5th plot).

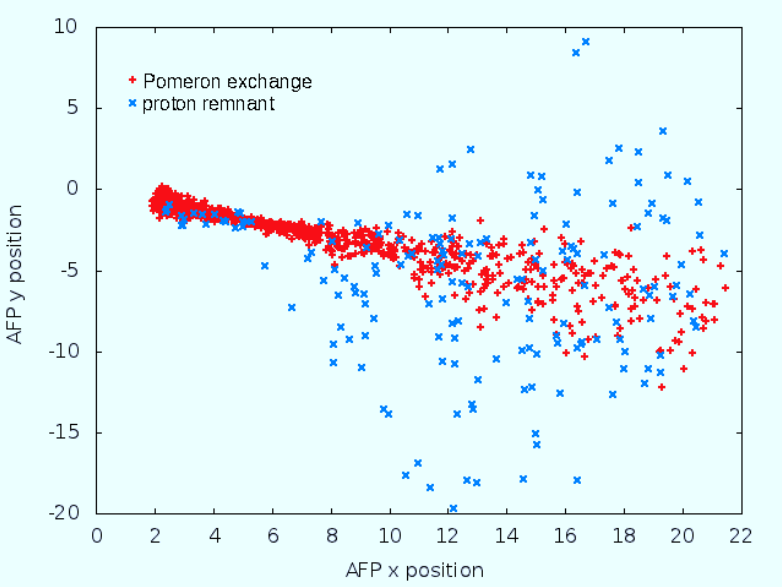

Figure 6.10: Positions of protons originated from Pomeron exchange (red) and hadronisation of the proton remnants (blue) in the AFP detectors.

incoming protons, but also of their arrival time. Using this information one can compare the longitudinal position of the hard interaction measured in the ATLAS tracker, z_0, with the one obtained from the arrival time measurements:

$$z_0^{AFP} = \frac{1}{2}c(t_1 - t_2),$$

where t_1 and t_2 are the arrival time values measured by the AFP detectors on either side of the IP and c is the speed of light. It should be pointed out that in this measurement only the time difference, $t_1 - t_2$ is meaningful. The bunch-crossing, *i.e.* the penetrating of one bunch by another, lasts a finite time of the order of 200 ps, which is much more than the resolution of the measurement. Therefore, one cannot say at which time the interaction occurred and the absolute time value is meaningless. If two protons come from the same interaction, its position can be calculated with the given formula. This leads to a very good background rejection, as shown in Figure 6.11, where $\Delta z = z_0 - z_0^{AFP}$ is plotted. For signal the distribution peaks at zero, whereas for background it is much wider.

The very small long tails of the distribution for the signal (merely visible in the plot) come from events that have the hard interaction outside the AFP acceptance, on one or both sides, and the hits originate from pile-up collisions. On the other hand the tails are so small because the events have been preselected in the generation by requiring a proton with $0.01 < \xi < 0.2$ on each side. This ξ range was chosen such that it is close to the AFP acceptance to allow efficient generation of events, but big enough to enable studies of the edge effects, like the influence of the detector distance to the beam centre or the detector shape.

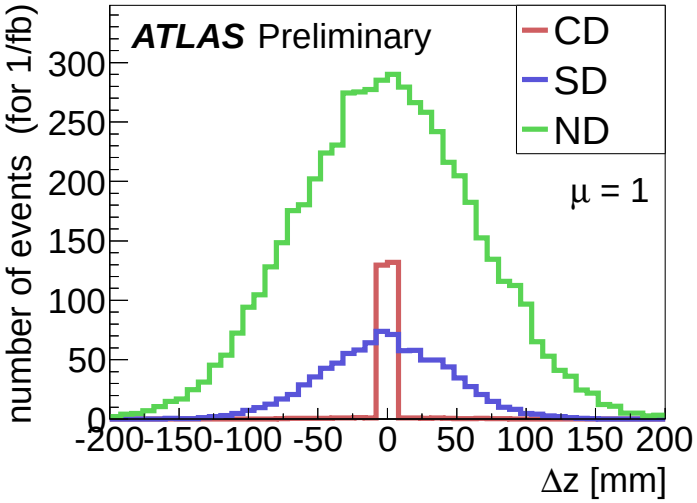

Figure 6.11: Distributions of the difference between the value of the longitudinal vertex coordinate reconstructed in the central detector and from the time measurement in the AFP detectors. Central diffractive production is drawn in red, single diffractive in blue and non-diffractive in green.

After requesting the AFP double tag and timing compatibility, the signal is still dominated by background. Naturally, operating at even smaller values of μ would help, but since the cross section for central diffractive production of the W boson is quite small, this would require a very long data collection, which is rather unrealistic. On the other hand, one could look for variables that discriminate the signal against the background. The most powerful one that has been found is the number of tracks reconstructed in the ATLAS Inner Detector and associated to the same vertex as the muon (the Primary Vertex, PV). The distributions are presented in Figure 6.12. It is clear that for the non-diffractive production mechanism the track multiplicity tends to be higher than for single and central diffraction. The reason behind this is simple. Diffractive scattering can be thought of as a proton-Pomeron (in the case of SD) and Pomeron-Pomeron (in CD) collision. Such interactions have a smaller centre-of-mass energy than the non-diffractive proton-proton collision. This means that the phase-space for particle emission is smaller in the diffractive case. This argument would suggest that the multiplicity in the central diffraction is smaller than in single diffraction. However, this is not observed in the plot. This observation can be explained by the fact that the CD events are usually central, whereas the SD ones are boosted. The boost would make some of the charged particles escape the tracker acceptance, decreasing the observed charged multiplicity.

Several additional variables have different distributions for signal and for background. Unfortunately, none of them can improve the final results using a cut-based selection. This is because the improvement on the signal over background ratio is smaller than the simultaneous loss of the signal statistics. However, these variables

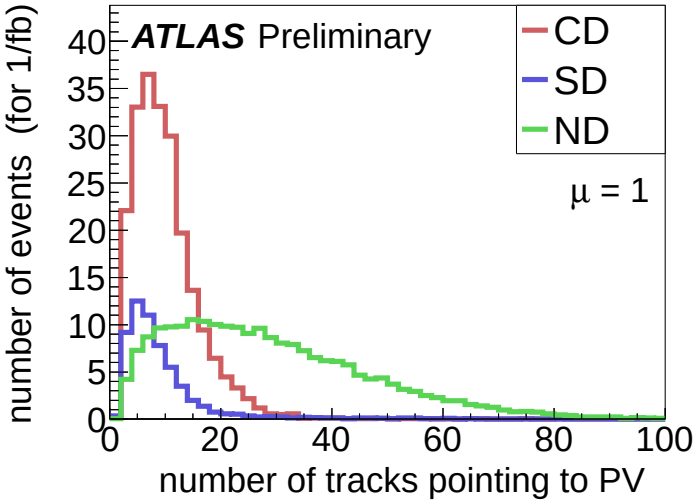

Figure 6.12: Distribution of the number of reconstructed tracks pointing to the reconstructed primary vertex. Central diffractive production is drawn in red, single diffractive in blue and non-diffractive in green.

can be used in a multidimensional analysis of data, where they can lead to an improvement of the final results. It should be stressed that the aim of this analysis was to show that the measurement is feasible and to sketch up the basic strategy. A precise definition of the signal selection should be done when data are available and a good agreement between them and Monte Carlo simulation is obtained.

One of the variables that have different distribution for signal and background is the minimal of the absolute pseudorapidity value of the tracks with the highest and lowest pseudorapidities:

$$\eta_{MIN} = \min(|\max \eta_i|, |\min \eta_i|), \tag{6.18}$$

where i numbers the reconstructed tracks. In other words, the pseudorapidity regions devoid of tracks starting from the edge of the Inner Detector is taken on both sides of the detector and the larger one is chosen. The variable is the pseudorapidity of the edge of this region, *i.e.* $\eta_{MIN} = 2.5 - \eta_{gap}$, where η_{gap} is the size of the gap, as described before, and 2.5 is the effective edge of the tracker. One should point out that even though a kind-of-a-gap is seen, it cannot be a Rapidity Gap as in its usual meaning. This is because a proton tagged in AFP detectors must have ξ between 0.02 and 0.14, which implies much smaller gaps than those that could be possibly observed in the tracker. The fact that such a difference is observed is just another manifestation of smaller radiation in a diffractive event due to smaller effective centre-of-mass energy. This is also the reason why the discriminating power of the variable is small.

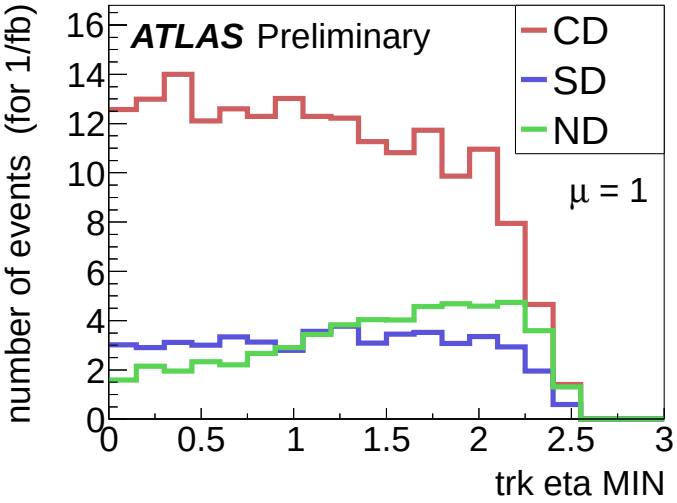

Figure 6.13: Distribution of the tracks η_{MIN} variable, as defined in the text, for central diffractive (CD), single diffractive (SD) and non-diffractive (ND) production of the W boson.

6.7 Results

The final signal selection requires:

1. **W** – W selection (medium muon identification, muon isolation > 0.01, muon transverse momentum > 30 GeV, missing transverse energy > 35 GeV, transverse mass > 40 GeV),
2. **AFP** – AFP double tag,
3. **time** – time compatibility ($\Delta z < 3$ mm),
4. **#tracks** – number of tracks associated to primary vertex < 15.

Table 6.3 presents the cross sections of the central diffractive signal and the single diffractive and non-diffractive backgrounds after each cut. The values for the W selection cut have been obtained with non-preselected samples, whereas all the rest used preselected ones (single tag preselection for SD and double tag preselection for ND). The consistency was checked at each step by comparing the results obtained from different samples.

The measurement of the W boson charge asymmetry in central diffractive processes is possible only in low pile-up environment. Otherwise, the signal would be completely dominated by non-diffractive background. Unfortunately, due to the small cross section of the process and the fact that the asymmetry measurement is quite prone to statistical fluctuations, a relatively large number of events is needed to make a statistically significant measurement. Therefore, a dedicated, long and low instantaneous luminosity data collecting period is needed. This can be possible towards the very end of the LHC operation, where the discovery search programme

Table 6.3: Number of events for 3 fb^{-1} for central diffractive (CD), single diffractive (SD) and non-diffractive (ND) W boson production after consecutive analysis requirements.

Cut name	CD	SD	ND
W sel.	$5.6 \cdot 10^3$	$3.8 \cdot 10^5$	$6.8 \cdot 10^7$
AFP	$1.7 \cdot 10^3$	$5.7 \cdot 10^3$	$3.4 \cdot 10^4$
time	$1.3 \cdot 10^3$	$3.5 \cdot 10^2$	$1.3 \cdot 10^3$
#tracks	$1.1 \cdot 10^3$	$3.3 \cdot 10^2$	$3.3 \cdot 10^2$

should be finished and such special runs could be accepted by the LHC experiments. It should be mentioned that there are also other measurements, especially the precision measurements in the electroweak sector, that would very much benefit from such dedicated conditions.

The results shown in the following assume an integrated luminosity of 3 fb^{-1} with an average pile-up multiplicity $\mu = 1$. For a comparison, a scenario of $\mu = 3$ with the same luminosity is also considered. The results were also obtained using full ATLAS detector simulation.

In real measurements not only the muon, but also the electron channel of the W decays can be used. This would result approximately[3] in doubling the collected statistics, which was taken into account in the following results.

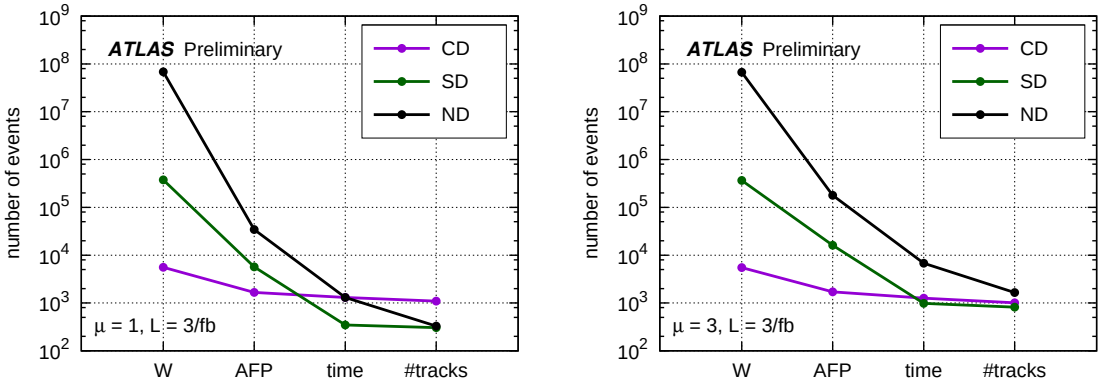

Figure 6.14: Number of W events produced for 3 fb$^{-}1$ in central diffractive (violet), single diffractive (green) and non-diffractive (black) mode that pass through consecutive cuts explained in the main text. Left: for $\mu = 1$ environment, right: $\mu = 3$.

The number of events in each studied W production process after the consecutive cuts is presented in Figure 6.14. After selecting the W events the signal is dominated by non-diffractive production by more that four orders of magnitude. The number of single diffractive events is, in the logarithmic scale, in the middle between the central diffractive and non-diffractive processes. The requirement of the AFP double tag is

[3]The efficiency of the W selection in the electron decay channel is slightly smaller than in the muon channel.

the most powerful one in this analysis. It decreases the non-diffractive contribution by more than three orders of magnitude and the single diffractive production by almost two. Of course, the background reduction for $\mu = 3$ is not that effective, since having additional protons from pile-up is more likely in this case.

The timing cut works similarly well for both $\mu = 1$ and $\mu = 3$, reducing both backgrounds by a factor of about twenty. At this point for $\mu = 1$ the numbers of signal and background events are comparable and the background is dominated by non-diffractive production. For $\mu = 3$ the single diffractive W production is comparable to the central diffractive one, but the non-diffractive contribution is almost an order of magnitude higher.

The cut on the number of tracks reduces the number of non-diffractive events. It slightly diminishes also the number of signal and single diffractive background events. After all analysis requirement, for $\mu = 1$ the combined sample is dominated by signal. Single and non-diffractive contributions are comparable and the purity is about 60%. For $\mu = 3$ the sample is still dominated by the non-diffractive background, the number of single and central diffractive is comparable and the purity is about 30%.

The data sample selected as described above will consist mostly of the signal events. This will allow measurements of various distributions. Figure 6.15 shows the distributions of the reduced energy loss of protons in beam 1 and 2. It is interesting to notice that there are very small differences between both sides. This is caused by a small difference in the setups of the magnets in beam 1 and beam 2 [124]. Other interesting distributions are presented in Figure 6.16, where the mass (M_X) and boost (y_X) of the centrally produced system (W boson + remnants of the Pomerons) are depicted. These variables are calculated from the reconstructed kinematic variables of protons registered in the AFP detectors using the following formulae:

$$M_X = \sqrt{s\xi_1\xi_2}, \qquad y_X = \frac{1}{2}\ln\frac{\xi_1}{\xi_2}. \tag{6.19}$$

One can also directly measure the properties of the centrally produced state. One example is the pseudorapidity of the produced muon, which is shown in Figure 6.17. An interesting feature is a clear asymmetry of the distribution. It comes from the differences between the two LHC beams, which affect the central system by requiring protons to be tagged. Naturally, this does not induce any asymmetry in the non-diffractive sample, in which the protons are produced in different interactions than the W boson.

The main goal of the present analysis was to check whether the measurement of the charge asymmetry in the central diffractive W production is feasible. However, one can see that even for $\mu = 1$ the purity of the final sample would not be perfect. Actually, the purity of the sample can be greatly increased by an additional requirement that in the event there is only one reconstructed vertex. This will remove a large part of single diffractive background, for which at least two interactions must

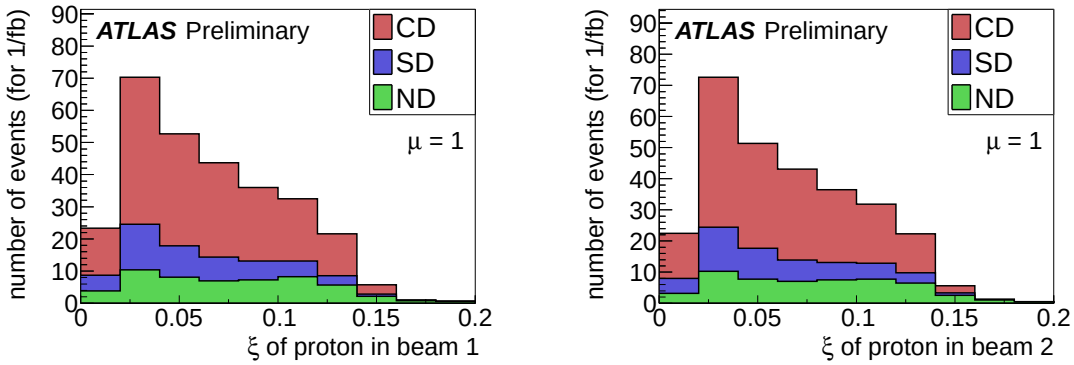

Figure 6.15: Distributions of protons reduced energy loss, ξ, for protons in beam 1 (left) and 2 (right), for the combined sample after all analysis cuts. Red colour shows the contribution from central diffractive, blue from single diffractive and green from non-diffractive production. The distributions are plotted cumulatively, *i.e.* on top of each other.

be present in the event. An even larger part of the non-diffractive events would be rejected by this request, because, in this case, at least three interactions are necessary. However, this would reduce the statistics, since also in the signal events there can be pile-up interactions. The overall effect would be an increase of the purity to about 85% with a simultaneous loss of half of the signal events. It has been checked that adding this requirement worsens the final results of the asymmetry measurement significance. Nevertheless, it can be very useful for measurements of the cross section and different distributions, as well as for various cross checks.

Since one wants to study the diffraction mechanisms by measuring the asymmetry for central diffractive events, one should take into account that single diffractive events can be governed by different mechanisms. Moreover, it does not necessarily have to be same as for central diffraction. In this analysis two production mechanisms are considered: the Pomeron exchange (POM) and Soft Colour Interactions (SCI). For non-diffractive production the asymmetry value of 0.142 is taken. This value was obtained from the non-diffractive full simulation sample after W selection. For central diffraction in the Pomeron model the asymmetry is zero and the single diffractive sample has the asymmetry of 0.06 (obtained like in the ND case). For the SCI model, in both single and central diffractive cases the asymmetry is assumed to be identical as in the non-diffractive production, as argued in [125].

The asymmetry for the sample consisting of N_{ND} non-diffractive, N_{SD} single diffractive and N_{CD} central diffractive events (obtained as described above) is calculated with the following formula:

$$A = \frac{A_{ND}N_{ND} + A_{SD}N_{SD} + A_{CD}N_{CD}}{N_{ND} + N_{SD} + N_{CD}}, \tag{6.20}$$

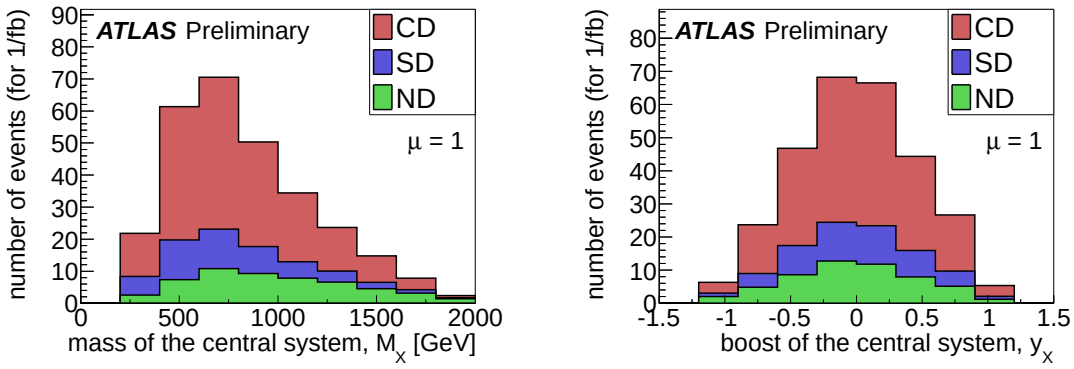

Figure 6.16: Distributions of the mass (left) and boost (right) of the central system (W boson + remnants of the Pomerons) for the combined sample after all analysis cuts. Red colour shows the contribution from central diffractive, blue from single diffractive and green from non-diffractive production. Both variables have been calculated from the reconstructed kinematics of the protons. The distributions are plotted cumulatively, *i.e.* on top of each other.

where A_{ND}, A_{SD} and A_{CD} are the asymmetry values assumed for each of the production process, see table 6.4.

As discussed above, four combinations could occur:

- both central and single diffraction are governed by Pomeron exchange – CD-POM + SD-POM,
- both central and single diffraction are governed by Soft Colour Interactions – CD-SCI + SD-SCI,
- central diffraction is governed by the Pomeron exchange, but single diffraction by Soft Colour Interactions – CD-POM + SD-SCI,
- central diffraction is governed by Soft Colour Interactions, but single diffraction by the Pomeron exchange – CD-SCI + SD-POM.

Figure 6.18 shows the asymmetry of the combined sample for the cases mentioned above, after each cut used in the analysis. The results are presented for $\mu = 1$ and $\mu = 3$. The green line presents the case, where both diffractive processes are ruled by the SCI mechanism and their asymmetry is the same as in the non-diffractive case. Therefore, any change in the composition of the combined sample does not change

Table 6.4: Asymmetry assumed for the of the non-diffractive (ND), single diffractive (SD) and central diffractive (CD) samples of the W boson production for two diffractive mechanisms: double Pomeron exchange (DPE) and Soft Colour Interactions (SCI).

	A_{ND}	A_{SD}	A_{CD}
DPE	0.14	0.06	0.00
SCI	0.14	0.14	0.14

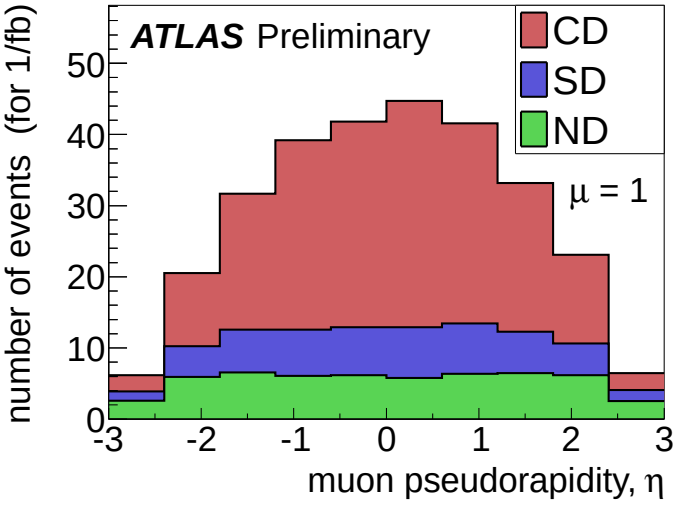

Figure 6.17: Distributions of muon pseudorapidity for the combined sample after all analysis cuts. Red colour shows the contribution from central diffractive, blue from single diffractive and green from non-diffractive production. The distributions are plotted cumulatively, *i.e.* on top of each other.

the asymmetry. On the other hand, if any of the diffractive contributions is governed by the Pomeron exchange, for which the asymmetry is smaller, the asymmetry of the whole sample decreases with increasing fraction of diffractive events. One can see that in case of $\mu = 1$ the asymmetry of the final sample, after all requirements, is much more sensitive to the mechanism of the central diffraction than to that of single diffraction. This is not the case for $\mu = 3$, where the effects of central and single diffraction are not that different. The reason is that for $\mu = 1$ the number of single diffractive events is smaller than the central diffractive ones, whereas for $\mu = 3$ these numbers are very close. In addition, since the number of non-diffractive events is smaller for $\mu = 1$ than for $\mu = 3$, the final asymmetry, for the case when the central diffraction mechanism is the Pomeron exchange, is smaller for lower pile-up scenario.

To study the possible statistical significance of rejecting one mechanism of diffractive production against the other, the uncertainty of the asymmetry measurement needs to be estimated. It is assumed that the systematic uncertainty is negligible compared to the statistical one. The reason for this is that while calculating the asymmetry, all uncertainties that are insensitive to the W charge cancel. On the other hand the statistical uncertainty of the measurement, given by the formula:

$$\sigma(A) = \sqrt{\frac{1 - A^2}{N}} \approx 1/\sqrt{N}, \tag{6.21}$$

can be quite large. Figure 6.19 shows the uncertainty as a function of the number of events.

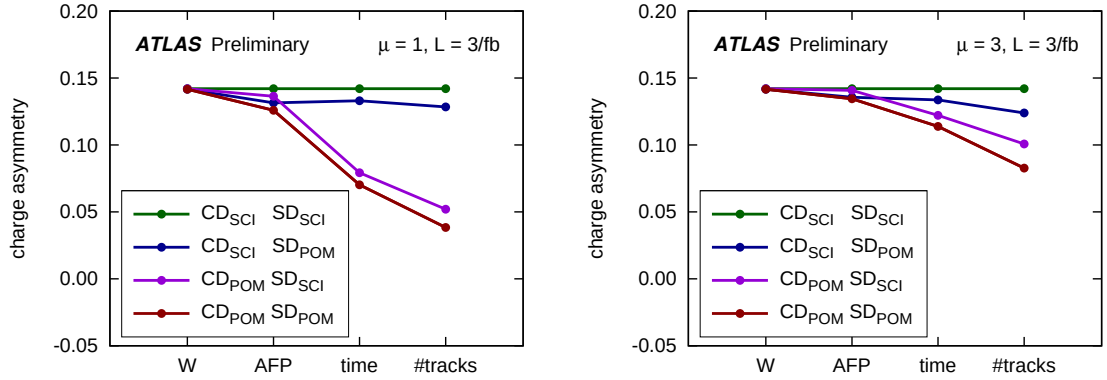

Figure 6.18: The charge asymmetry of the W sample collected with 3 fb^{-}1 consisting of central diffractive, single diffractive and non-diffractive production, that pass through consecutive cuts explained in the text. Different colours represent different assumptions on the models (asymmetry) of diffractive (central and single) production, green: central diffraction and single diffraction governed by Soft Colour Interactions, blue: CD by SCI and SD by Pomeron exchange, violet: CD by Pomeron exchange and SD by SCI, red: both CD and SD by Pomeron exchange. Left plot presents results for $\mu = 1$, right plot for $\mu = 3$.

The details of the single diffractive production mechanism play an important role in the discrimination between different models of central diffractive processes. The strongest discrimination can be obtained in the case where single diffraction mechanism is the same as the central diffractive one, *i.e.* the discrimination between CD-SCI + SD-SCI and CD-POM + SD-POM. This is illustrated in Figure 6.20, where the measurement uncertainty obtained with 3 fb^{-1} is plotted. On the other hand, the worst discrimination occurs when single diffraction is ruled by a different mechanism than central diffraction, namely the discrimination between CD-SCI + SD-POM and CD-POM + SD-SCI, which is presented in Figure 6.21. The uncertainties of the measurement are the same as before, because the numbers of events are the same, but the asymmetry values predicted by two hypotheses are now closer. For $\mu = 1$ the measurement is still significant, but for $\mu = 3$ this is not longer the case – after all the cuts the separation barely exceeds one standard deviation.

It is important to point out that for $\mu = 3$ the uncertainty is actually smaller than for $\mu = 1$. The reason for this is a larger number of events in the combined sample. However, additional events are mainly of non-diffractive nature. A smaller purity of the combined sample for $\mu = 3$ results in a smaller sensitivity to the mechanism of central diffractive production. That is why the statistical significance is larger for $\mu = 1$, even though the uncertainty is larger for $\mu = 3$.

Since the main source of the uncertainties are the random fluctuations in the sample, the measurement becomes more and more significant with increasing statistics. Figure 6.22 shows the statistical significance as a function of collected luminosity. The red line corresponds to $\mu = 1$ and the green one to $\mu = 3$. The plot on the left

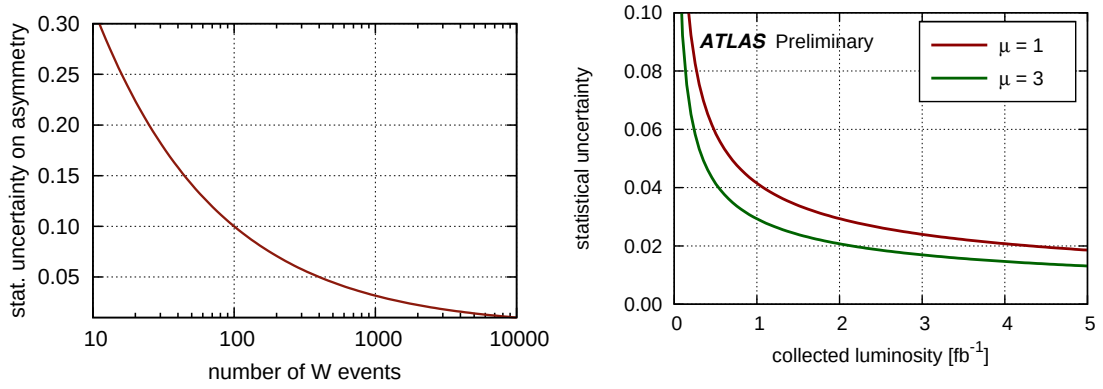

Figure 6.19: Statistical uncertainty of the asymmetry measurement as a function of number of events (left) and the collected luminosity (right) for

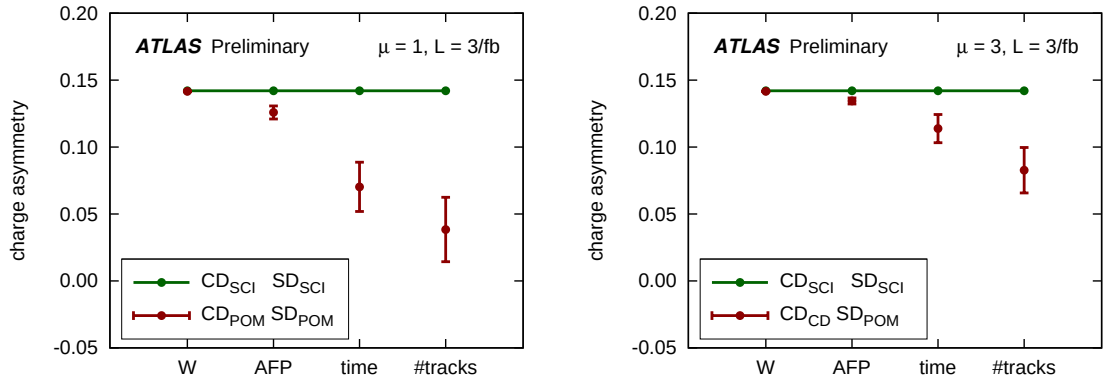

Figure 6.20: Charge asymmetry of the W sample collected with 3 fb^{-1} consisting of central diffractive, single diffractive and non-diffractive production, that pass consecutive cuts explained in the text. Green points represent case where diffractive production, both CD and SD, are governed by Soft Colour Interactions, red points represent the Pomeron exchange. For the red points the statistical uncertainty of the red points are plotted. Left plot presents results for $\mu = 1$, right plot for $\mu = 3$.

shows the significance in the most favourable case, while the right figure corresponds to the most unfavourable scenario. It is clear that the measurement with $\mu = 1$ is much cleaner, provided the same amount of collected luminosity. In the best case, 1.5 fb^{-1} is enough for a 3σ measurement, while 4 fb^{-1} can give 5σ. In the worst case 4σ can be obtained with 2.5 fb^{-1} and almost the same is needed for the best case with $\mu = 3$.

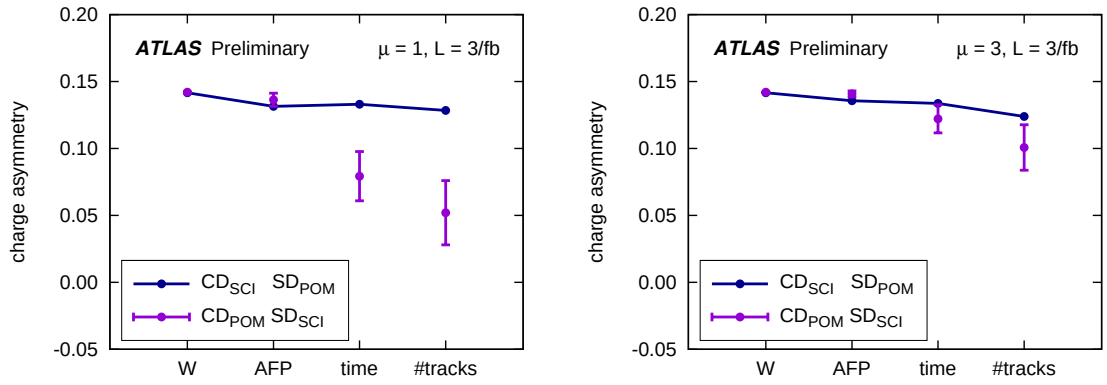

Figure 6.21: Charge asymmetry of the W sample collected with 3 fb^{-1} consisting of central diffractive, single diffractive and non-diffractive production, that pass the consecutive cuts explained in the text. Green points represent case where central diffraction is governed by Soft Colour Interactions, while the red points represent the Pomeron exchange. For the red points the statistical uncertainty is plotted. The left plot presents the results for $\mu = 1$, right plot for $\mu = 3$.

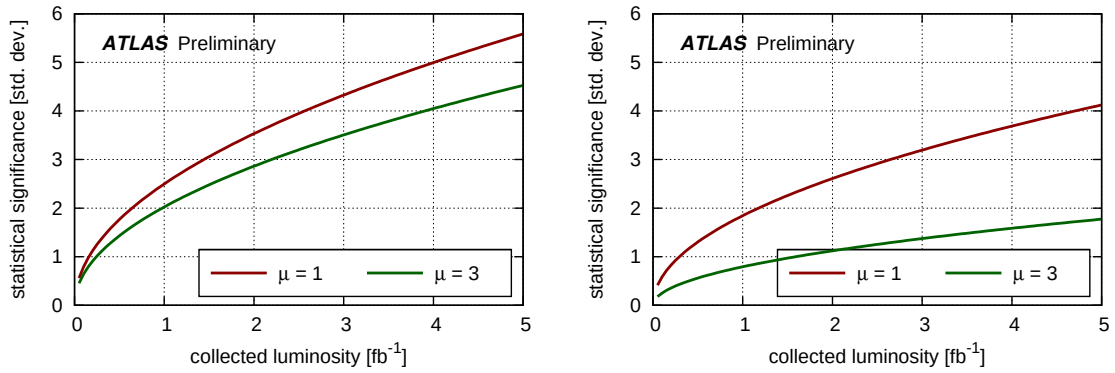

Figure 6.22: Statistical significance of the central diffraction mechanism determination (Pomeron exchange vs Soft Colour Interactions) based on charge asymmetry measurement, as a function of collected luminosity. Red line shows the results for $\mu = 1$, green line for $\mu = 3$. Left plot shows the significance for the case where single diffraction is governed by the same mechanism as the central diffraction (CD-SCI + SD-SCI vs CD-POM + SD-POM), right plot assumes the mechanisms to be opposite (CD-SCI + SD-POM vs CD-POM + SD-SCI)

Summary and Conclusions

The presented thesis has been devoted to studies of diffractive processes with the ATLAS detector at the LHC. The first discussed topic was the exclusive jet production measurement at the LHC and its role in constraining the theoretical models. This is particularly important for exclusive production of the Higgs boson. Taking into account the recent results of the ATLAS and CMS Collaborations [54, 55], reporting the discovery of a particle consistent with the Higgs boson, it is very important to study the properties of the discovered particle. It must be stressed that exclusive production offers a unique possibility of determining whether the particle has 0^{++} quantum numbers. This is much more difficult with standard methods. Exclusive measurements of Higgs production requires installation of additional detectors (AFP420), but large uncertainties of the theoretical descriptions and cross section predictions question the possibility of its observation. The AFP420 detectors can be accepted by the ATLAS Collaboration and installed in the LHC tunnel, provided it is proven that measuring exclusive Higgs production is feasible. An earlier measurement of exclusive jets would be an essential ingredient.

Next, it has been demonstrated that the ALFA@ATLAS physics programme can be extended to the measurement of exclusive, non-resonant production of unlike charge pion pairs. Such measurement can be done by tagging the forward protons in the ALFA detectors and measuring the pions in the ATLAS central detector (in the tracker or the calorimeter). It has been shown that the visible cross section is high enough that the measurement is possible in dedicated, low luminosity runs, in which the ALFA detectors can operate. The presented analysis motivated a common data-taking of the ALFA and ATLAS detectors in 2011 and the collected data are presently being analysed.

A large part of the thesis has been devoted to studies of possible measurements using the ATLAS detector upgraded with the AFP stations at 210 metres. Studies of

proton transport and development of the procedure for energy unfolding from AFP measurements were an important contribution of the author to the AFP detectors proposal. A very good resolution of the ξ reconstruction allows comparison of the centrally produced system to the measured forward protons. Together with the timing compatibility requirement, due to QUARTIC measurements, this provides remarkable background rejection that is unique for the AFP detectors. A variety of physics processes can be studied with the AFP detectors. They range from $\gamma\gamma$ interactions, through the exclusive production up to hard diffraction and are interesting from both SM and BSM points of view.

The feasibility study of central diffractive W production measurement has been presented in the thesis in detail. The Monte Carlo analysis was based on full simulation of the ATLAS detector and took into account pile-up, which is a crucial effect for AFP measurements and constitutes to the main backgrounds. It has been argued that a charge asymmetry measurement in central diffractive W production can contribute to the understanding of diffractive mechanism. It has been shown that such measurement is possible and 1.5 fb^{-1} of integrated luminosity collected in low pile-up environment (the average interaction multiplicity equal 1) is needed in order to distinguish between the predictions of the Pomeron model and the Soft Colour Interactions approach at 3σ confidence level.

Finally, it should be pointed out that diffraction at the LHC is not any more only a sub-topic among various QCD measurements. Now, the methods developed for diffractive measurements (mainly the forward proton tagging, but the rapidity gap method is also considered) can be used to investigate *new physics*, which is one of the most important goals of the LHC physics programme. One example is the exclusive Higgs production, which provides an opportunity to determine the Higgs quantum numbers. Studies of anomalous quartic couplings in two-photon processes are another example, since they can be used for probing various beyond Standard Model scenarios. The sensitivity in this case is much larger (orders of magnitude) than for the conventional methods.

Recently, new ideas have been discussed within the AFP group. In case of the Higgs boson existence, additional anomalous couplings are possible and they can also provide insight into new physics. Another interesting field of research is possible production of magnetic monopoles in $\gamma\gamma$ interactions. It is possible that a highly ionising monopole, if it exists, is fully stopped in the ATLAS beam pipe or in the first layers of the pixel detector. Then, it would not be possible to detect it with standard methods. On the other hand, with a help of AFP detectors an event with large missing mass could be observed. This can provide a unique measurement possibility.

Already now one can observe a growing interest in the AFP detectors and their physics programme. When they are fully accepted and built it is likely that new ideas will show up, making the LHC diffractive programme even more exciting.

Bibliography

[1] S. Donnachie, H. G. Dosch, O. Nachtmann and P. Landshoff, *Pomeron physics and QCD*, Camb. Monogr. Part. Phys. Nucl. Phys. Cosmol. **19** (2002) 1.

[2] M. L. Good and W. D. Walker, *Diffraction disssociation of beam particles*, Phys. Rev. **120**, 1857 (1960).

[3] S. Chekanov *et al.* [ZEUS Collaboration], *Deep inelastic scattering with leading protons or large rapidity gaps at HERA*, Nucl. Phys. B **816** (2009) 1 [arXiv:0812.2003 [hep-ex]].

[4] S. Bethke, α_s *2002*, Nucl. Phys. Proc. Suppl. **121** (2003) 74 [hep-ex/0211012].

[5] G. Antchev *et al.* [TOTEM Collaboration], *Elastic Scattering and Total Cross-Section in* $p+p$ *reactions measured by the LHC Experiment TOTEM at* $\sqrt{s} = 7$ *TeV*, arXiv:1204.5689 [hep-ex].

[6] G. Aad *et al.* [ATLAS Collaboration], *Rapidity gap cross sections measured with the ATLAS detector in pp collisions at sqrt(s) = 7 TeV*, Eur. Phys. J. C **72** (2012) 1926 [arXiv:1201.2808 [hep-ex]].

[7] G. Watt, *MSTW PDFs and impact of PDFs on cross sections at Tevatron and LHC*, arXiv:1201.1295 [hep-ph].

[8] H.-L. Lai, M. Guzzi, J. Huston, Z. Li, P. M. Nadolsky, J. Pumplin and C.-P. Yuan, *New parton distributions for collider physics*, Phys. Rev. D **82** (2010) 074024 [arXiv:1007.2241 [hep-ph]].

[9] P. Jimenez-Delgado and E. Reya, *Dynamical NNLO parton distributions*, Phys. Rev. D **79**, 074023 (2009) [arXiv:0810.4274 [hep-ph]].

[10] G. Ingelman and P. E. Schlein, *Jet Structure in High Mass Diffractive Scattering*, Phys. Lett. B **152**, 256 (1985).

[11] R. Bonino *et al.* [UA8 Collaboration], *Evidence for Transverse Jets in High Mass Diffraction*, Phys. Lett. B **211** (1988) 239.

[12] A. Brandt *et al.* [UA8 Collaboration], *Cross-section measurements of hard diffraction at the SPS collider*, Phys. Lett. B **421**, 395 (1998) [hep-ex/9709015].

[13] A. Aktas *et al.* [H1 Collaboration], *Measurement and QCD analysis of the diffractive deep-inelastic scattering cross-section at HERA*, Eur. Phys. J. C **48** (2006) 715 [hep-ex/0606004].

[14] A. Aktas *et al.* [H1 Collaboration], *Dijet Cross Sections and Parton Densities in Diffractive DIS at HERA*, JHEP **0710** (2007) 042 [arXiv:0708.3217 [hep-ex]].

[15] T. Aaltonen *et al.* [CDF Collaboration], *Diffractive W and Z Production at the Fermilab Tevatron*, Phys. Rev. D **82** (2010) 112004 [arXiv:1007.5048 [hep-ex]].

[16] V. A. Khoze, A. D. Martin and M. G. Ryskin, *Can the Higgs be seen in rapidity gap events at the Tevatron or the LHC?*, Eur. Phys. J. C **14** (2000) 525 [arXiv:hep-ph/0002072], Eur. Phys. J. C **19** (2001) 477.

[17] B. E. Cox, F. K. Loebinger and A. D. Pilkington, *Detecting Higgs bosons in the $b\bar{b}$ decay channel using forward proton tagging at the LHC*, JHEP **0710** (2007) 090 [arXiv:0709.3035 [hep-ph]].

[18] T. Aaltonen *et al.* [CDF Collaboration], *Observation of Exclusive Dijet Production at the Fermilab Tevatron $p\bar{p}$ Collider*, Phys. Rev. D **77**, 052004 (2008) [arXiv:0712.0604 [hep-ex]].

[19] V. M. Abazov *et al.* [D0 Collaboration], *High mass exclusive diffractive dijet production in $\mathbf{p\bar{p}}$ collisions at $\sqrt{\mathbf{s}}$ = 1.96 TeV*, Phys. Lett. B **705** (2011) 193 [arXiv:1009.2444 [hep-ex]].

[20] P. Lebiedowicz and A. Szczurek, *Exclusive $pp \to pp\pi^+\pi^-$ reaction: From the threshold to LHC*, Phys. Rev. D **81** (2010) 036003 [arXiv:0912.0190 [hep-ph]].

[21] J. Breitweg *et al.* [ZEUS Collaboration], *Measurement of diffractive photoproduction of vector mesons at large momentum transfer at HERA*, Eur. Phys. J. C **14** (2000) 213 [hep-ex/9910038].

[22] A. Cisek, W. Schafer and A. Szczurek, *Production of Z0 bosons with rapidity gaps: Exclusive photoproduction in gamma p and pp collisions and inclusive double diffractive Z0's*, Phys. Rev. D **80** (2009) 074013 [arXiv:0906.1739 [hep-ph]].

[23] A. Dechambre, O. Kepka, C. Royon and R. Staszewski, *Uncertainties on exclusive diffractive Higgs and jets production at the LHC*, Phys. Rev. D **83**, 054013 (2011) [arXiv:1101.1439 [hep-ph]].

[24] T. Aaltonen *et al.* [CDF Collaboration], *Observation of Exclusive Gamma Gamma Production in $p\bar{p}$ Collisions at $\sqrt{s} = 1.96$ TeV*, Phys. Rev. Lett. **108** (2012) 081801 [arXiv:1112.0858 [hep-ex]].

[25] G. Corcella, I.G. Knowles, G. Marchesini, S. Moretti, K. Odagiri, P. Richardson, M.H. Seymour and B.R. Webber, *HERWIG 6.5*, JHEP 0101 (2001) 010 [hep-ph/0011363]; hep-ph/0210213.

[26] T. Sjostrand, S. Mrenna and P. Z. Skands, *PYTHIA 6.4 Physics and Manual*, JHEP **0605** (2006) 026 [hep-ph/0603175].

[27] M. Boonekamp, A. Dechambre, V. Juranek, O. Kepka, M. Rangel, C. Royon, R. Staszewski, *FPMC: A Generator for forward physics*, arXiv:1102.2531 [hep-ph].

[28] A. Białas and P. V. Landshoff, *Higgs production in pp collisions by double pomeron exchange*, Phys. Lett. B **256** (1991) 540.

[29] A. Schafer, O. Nachtmann and R. Schopf, *Production of Higgs particles in diffractive hadron hadron collisions*, Phys. Lett. B **249** (1990) 331.

[30] A. Bzdak, *Production of gluon jets in pp collisions by double pomeron exchange in the Landshoff-Nachtmann model*, Acta Phys. Polon. **B35** (2004) 1733-1746. [hep-ph/0404153].

[31] A. Bzdak, *Central inclusive dijets production by double pomeron exchange. Comparison with the CDF results*, Phys. Lett. **B608** (2005) 64-68. [hep-ph/0407193].

[32] V. A. Khoze, A. D. Martin and M. G. Ryskin, *Prospects for new physics observations in diffractive processes at the LHC and Tevatron*, Eur. Phys. J. C **23**, 311 (2002) [arXiv:hep-ph/0111078].

[33] A. D. Martin and M. G. Ryskin, *Unintegrated generalised parton distributions*, Phys. Rev. D **64** (2001) 094017 [arXiv:hep-ph/0107149].

[34] J. R. Cudell and O. F. Hernandez, *Particle Production in a Hadron Collider Rapidity Gap: The Higgs Case*, Nucl. Phys. B **471** (1996) 471 [arXiv:hep-ph/9511252].

[35] I. P. Ivanov, N. N. Nikolaev and A. A. Savin, *Diffractive vector meson production at HERA: From soft to hard QCD*, Phys. Part. Nucl. **37** (2006) 1 [arXiv:hep-ph/0501034].

[36] Y. L. Dokshitzer, D. Diakonov and S. I. Troian, *Hard Processes In Quantum Chromodynamics*, Phys. Rept. **58**, 269 (1980).

[37] V. A. Khoze, A. D. Martin and M. G. Ryskin, *Higgs or dijet production in double rapidity gap events*, arXiv:hep-ph/0006005.

[38] T. D. Coughlin and J. R. Forshaw, *Central Exclusive Production in QCD*, JHEP **1001** (2010) 121, [arXiv:hep-ph/0912.3280].

[39] L. A. Harland-Lang, V. A. Khoze, M. G. Ryskin and W. J. Stirling, *Standard candle central exclusive processes at the Tevatron and LHC*, Eur. Phys. J. C **69** (2010) 179 [arXiv:1005.0695 [hep-ph]].

[40] J. R. Cudell, A. Dechambre, O. F. Hernandez and I. P. Ivanov, *Central exclusive production of dijets at hadronic colliders*, Eur. Phys. J. C **61** (2009) 369 [arXiv:0807.0600 [hep-ph]].

[41] J. R. Cudell, A. Dechambre and O. F. Hernandez, *Higgs Central Exclusive Production*, Phys. Lett. B **706** (2012) 333 [arXiv:1011.3653 [hep-ph]].

[42] A. Dechambre, *pricate communication*.

[43] M. Gluck, E. Reya and A. Vogt, *Dynamical parton distributions revisited*, Eur. Phys. J. C **5**, 461 (1998) [arXiv:hep-ph/9806404].

[44] A. D. Martin, R. G. Roberts, W. J. Stirling and R. S. Thorne, *Scheme dependence, leading order and higher twist studies of MRST partons*, Phys. Lett. B **443**, 301 (1998) [arXiv:hep-ph/9808371].

[45] H. L. Lai and W. K. Tung, *Charm production and parton distributions*, Z. Phys. C **74**, 463 (1997) [arXiv:hep-ph/9701256].

[46] I. P. Ivanov and N. N. Nikolaev, *Anatomy of the differential gluon structure function of the proton from the experimental data on F2(p)(x,Q**2)*, Phys. Rev. D **65** (2002) 054004 [arXiv:hep-ph/0004206].

[47] I. P. Ivanov, *Diffractive production of vector mesons in deep inelastic scattering within k(t)-factorization approach*, arXiv:hep-ph/0303053.

[48] J. Monk and A. Pilkington, *ExHuME: A Monte Carlo event generator for exclusive diffraction*, Comput. Phys. Commun. **175**, 232 (2006) [arXiv:hep-ph/0502077].

[49] O. Kepka and C. Royon, *Search for exclusive events using the dijet mass fraction at the Tevatron*, Phys. Rev. D **76** (2007) 034012 [arXiv:0704.1956 [hep-ph]].

[50] V. A. Khoze, A. D. Martin and M. G. Ryskin, *Soft diffraction and the elastic slope at Tevatron and LHC energies: A MultiPomeron approach*, Eur. Phys. J. C **18**, 167 (2000) [arXiv:hep-ph/0007359].

[51] A. Dechambre, *Quasi-Elastic Production at Hadronic Colliders*, PhD thesis, Les Editions de l'Université de Liège, 2010.

[52] L. Evans, (ed.) and P. Bryant, (ed.), *LHC Machine*, JINST **3** (2008) S08001.

[53] ATLAS Collaboration, *An update to the combined search for the Standard Model Higgs boson with the ATLAS detector at the LHC using up to 4.9 fb^{-1} of pp collision data at $\sqrt{s} = 7$ TeV*, ATLAS-CONF-2012-019.

[54] F. Gianotti [representing the ATLAS Collaboration], *Status of the Standard Model Higgs Searches in ATLAS*, 4$^{\text{th}}$ July 2012.

[55] J. Incandela, [on behalf of the CMS Collaboration], *Status of the CMS SM Higgs Search*, 4$^{\text{th}}$ July 2012.

[56] S. P. Martin, *A Supersymmetry primer*, In *Kane, G.L. (ed.): Perspectives on supersymmetry II* 1-153 [hep-ph/9709356].

[57] J. D. Lykken, *Introduction to supersymmetry*, hep-th/9612114.

[58] M. Drees, *An Introduction to supersymmetry*, hep-ph/9611409.

[59] A. Bilal, *Introduction to supersymmetry*, hep-th/0101055.

[60] G. Aad *et al.* [ATLAS Collaboration], *The ATLAS Experiment at the CERN Large Hadron Collider*, JINST **3** (2008) S08003.

[61] S. Chatrchyan *et al.* [CMS Collaboration], *The CMS experiment at the CERN LHC*, JINST **3** (2008) S08004.

[62] K. Aamodt *et al.* [ALICE Collaboration], *The ALICE experiment at the CERN LHC*, JINST **3** (2008) S08002.

[63] A. A. Alves, Jr. *et al.* [LHCb Collaboration], *The LHCb Detector at the LHC*, JINST **3** (2008) S08005.

[64] G. Anelli *et al.* [TOTEM Collaboration], *The TOTEM experiment at the CERN Large Hadron Collider*, JINST **3** (2008) S08007.

[65] O. Adriani *et al.* [LHCf Collaboration], *The LHCf detector at the CERN Large Hadron Collider*, JINST **3** (2008) S08006.

[66] S. Cecchini *et al.* [MoEDAL Collaboration], *Technical Design Report of the MoEDAL Experiment*, MoEDAL-TDR-1.1, CERN-LHC-2009-006.

[67] C. Eck *et al.*, *LHC computing Grid : Technical Design Report*, LCG-TDR-001, CERN-LHCC-2005-024.

[68] ATLAS Collaboration, *ATLAS Inner detector: technical design report. 1*, CERN-LHCC-97-016.

[69] ATLAS Collaboration, *ATLAS Inner detector: technical design report. 2*, CERN-LHCC-97-017.

[70] ATLAS Collaboration, *ATLAS pixel detector: technical design report*, CERN-LHCC-98-013.

[71] ATLAS Collaboration, *Liquid argon calorimeter technical design report*, CERN-LHCC-96-041.

[72] ATLAS Collaboration, *Tile calorimeter technical design report*, CERN-LHCC-96-042.

[73] ATLAS Collaboration, *Muon spectrometer technical design report*, CERN-LHCC-97-022.

[74] P. Jenni, and M. Nordberg, M. Nessi and K. Jon-And, "ATLAS Forward Detectors for Measurement of Elastic Scattering and Luminosity", ATLAS-TDR-018, CERN-LHCC-2008-004.

[75] ATLAS Collaboration, *First-level trigger technical design report*, CERN-LHCC-98-014.

[76] ATLAS Collaboration, *ATLAS high-level trigger, data acquisition and controls technical design report*, CERN-LHCC-2003-022.

[77] ATLAS Collaboration, *Atlas Computing: technical design report*, CERN-LHCC-2005-022.

[78] M. Cacciari, G. P. Salam and G. Soyez, *The Anti-k(t) jet clustering algorithm*, JHEP **0804** (2008) 063 [arXiv:0802.1189 [hep-ph]].

[79] A. Breakstone *et al.* (ABCDHW Collaboration), Z. Phys. **C42** (1989) 387.

[80] A. Breakstone *et al.* (ABCDHW Collaboration), Z. Phys. **C48** (1990) 569.

[81] T. Akkeson *et al.* (AFS Collaboration), Nucl. Phys. **B264** (1986) 154.

[82] R. Staszewski, P. Lebiedowicz, M. Trzebiński, J. Chwastowski and A. Szczurek, *Exclusive $\pi^+\pi^-$ Production at the LHC with Forward Proton Tagging*, Acta Phys. Polon. B **42**, 1861 (2011) [arXiv:1104.3568 [hep-ex]].

[83] P. Lebiedowicz, R. Pasechnik and A. Szczurek, *Measurement of exclusive production of scalar χ_{c0} meson in proton-(anti)proton collisions via $\chi_{c0} \to \pi^+\pi^-$ decay*, Phys. Lett. B **701** (2011) 434 [arXiv:1103.5642 [hep-ph]].

[84] A. Donnachie and P. V. Landshoff, *Total cross-sections*, Phys. Lett. B **296**, 227 (1992) [hep-ph/9209205].

[85] M. Ferro-Luzzi, *Experiments' expectations*, Chamonix 2011 LHC Performance Workshop.

[86] Pawel Bruckman de Renstrom, *private communication.*

[87] The ATLAS Collaboration, *Charged-particle multiplicities in pp interactions measured with the ATLAS detector at the LHC*, arXiv:1012.5104(hep-ex).

[88] D. Gillberg (on behalf of the ATLAS Liquid Argon Calorimeter Group), 14th International Conference On Calorimetry In High Energy Physics, `http://cdsweb.cern.ch/record/1284260/`

[89] *Letter of Intent for the Phase-I Upgrade of the ATLAS Experiment*, CERN-LHCC-2011-012, LHCC-I-020.

[90] R. S. Gupta, *Probing Quartic Neutral Gauge Boson Couplings using diffractive photon fusion at the LHC,* Phys. Rev. D **85** (2012) 014006 [arXiv:1111.3354 [hep-ph]].

[91] E. Chapon, C. Royon and O. Kepka, *Anomalous quartic $WW\gamma\gamma$, $ZZ\gamma\gamma$, and trilinear $WW\gamma$ couplings in two-photon processes at high luminosity at the LHC*, Phys. Rev. D **81** (2010) 074003 [arXiv:0912.5161 [hep-ph]].

[92] O. Kepka, C. Royon, L. Schoeffel, R. Staszewski, M. Trzebinski, R. Zlebcik, *Physics Cases within the AFP project.* ATL-COM-PHYS-2012-775 (ATLAS internal note, under review).

[93] IBL Collaboration, CERN-LHCC-2010-013, ATLAS-TRD-019.

[94] G. Abbiendi *et al.* [OPAL Collaboration], *Constraints on anomalous quartic gauge boson couplings from $\nu\bar{\nu}\gamma\gamma$ and $q\bar{q}\gamma\gamma$ events at LEP-2*, Phys. Rev. D **70** (2004) 032005 [hep-ex/0402021].

[95] O. J. P. Eboli, M. C. Gonzalez-Garcia, S. M. Lietti and S. F. Novaes, *Anomalous quartic gauge boson couplings at hadron colliders*, Phys. Rev. D **63** (2001) 075008 [hep-ph/0009262].

[96] P. J. Bell, *Quartic Gauge Couplings and the Radiation Zero in $pp \to l^{\pm}\nu\gamma\gamma$ events at the LHC*, Eur. Phys. J. C **64** (2009) 25 [arXiv:0907.5299 [hep-ph]].

[97] A. Brandt et al., *The QUARTIC Detector*, in preparation.

[98] *Electronics, medical and particle physics applications. Proceedings, Workshop on Timing Detectors, Cracow, Poland, November 29-December 1, 2010*, Acta Phys. Pol. B4 Proc. Suppl. (2011) 1-114.

[99] `madx.web.cern.ch/madx/madx.old/.`

[100] P. Bussey, *private communication.*

[101] `svnweb.cern.ch/trac/atlasoff/browser/ForwardDetectors/FPTracker`

[102] J. de Favereau, X. Rouby and K. Piotrzkowski, *Hector: A Fast simulator for the transport of particles in beamlines*, JINST **2** (2007) P09005 [arXiv:0707.1198 [physics.acc-ph]].

[103] R. Staszewski and J. Chwastowski, *Transport Simulation and Diffractive Event Reconstruction at the LHC*, Nucl. Instrum. Meth. A **609**, 136 (2009) [arXiv:0906.2868 [physics.ins-det]].

[104] R. Staszewski, Master Thesis, 2008, unpublished.

[105] `en.wikipedia.org/wiki/Bisection_method`

[106] N. Ohuchi et al., Proc. of EPAC 2002, Paris, France, 2002, p. 2418,
E. Todesca, Proc. of LHC Project Workshop – Chamonix XIII, Chamonix, France, 2004, p. 138,
O. Brüning et al., Proc. of LHC Project Workshop – Chamonix XIII, Chamonix, France, 2004, p. 178,
N. Sammut et al., Proc. of EPAC 2008, Genoa, Italy, 2008, p. 2479,
N. Sammut et al., Proc. of EPAC 2008, Genoa, Italy, 2008, p. 2482.

[107] CDF, F. Abe *et al.*, Phys. Rev. Lett. **74**, 850 (1995), [hep-ex/9501008].

[108] D0, V. M. Abazov *et al.*, Phys. Rev. Lett. **101**, 211801 (2008), [0807.3367].

[109] CDF, T. Aaltonen *et al.*, Phys. Rev. Lett. **102**, 181801 (2009), [0901.2169].

[110] G. Aad *et al.* [ATLAS Collaboration], *Measurement of the Muon Charge Asymmetry from W Bosons Produced in pp Collisions at* $\sqrt{s} = 7$ *TeV with the ATLAS detector*, Phys. Lett. B **701** (2011) 31 [arXiv:1103.2929 [hep-ex]].

[111] S. Chatrchyan *et al.* [CMS Collaboration], *Measurement of the lepton charge asymmetry in inclusive W production in pp collisions at* $\sqrt{s} = 7$ *TeV*, JHEP **1104** (2011) 050. [arXiv:1103.3470 [hep-ex]].

[112] J. C. Collins, *Proof of factorization for diffractive hard scattering*, Phys. Rev. D **57** (1998) 3051 [Erratum-ibid. D **61** (2000) 019902];

[113] G. Ingelman and P. E. Schlein, *Jet Structure In High Mass Diffractive Scattering*, Phys. Lett. B **152** (1985) 256.

[114] A. Edin, G. Ingelman, J. Rathsman, Phys. Lett. **B366** (1996) 371.

[115] K. Golec-Biernat, A. Luszczak, *Diffractive production of electroweak vector bosons at the LHC*, Phys. Rev. **D81** (2010) 014009. [arXiv:0911.2789 [hep-ph]].

[116] M. Boonekamp, F. Chevallier, C. Royon, L. Schoeffel. Feb 2009. 92 pp. Published in Acta Phys.Polon. B40 (2009) 2239-2321

[117] R. K. Ellis, W. J. Stirling and W. B. R., QCD and Collider Physics, *Cambridge University Press* (1996).

[118] R. S. Thorne, A. D. Martin, W. J. Stirling and G. Watt, *Status of MRST/MSTW PDF sets*, arXiv:0907.2387 [hep-ph].

[119] SCI MC, `http://www3.tsl.uu.se/thep/MC/scigal/`.

[120] R. Pasechnik, D. Werder, *private communication*.

[121] A. Aktas *et al.* [H1 Collaboration], Eur. Phys. J. C **48** (2006) 715; S. Chekanov [ZEUS Collaboration], Nucl. Phys. B **800** (2008) 1.

[122] C. Royon, L. Schoeffel, S. Sapeta, R. B. Peschanski and E. Sauvan, Nucl. Phys. B **781** (2007) 1.

[123] G. Aad *et al.* [Atlas Collaboration], *Measurement of the $W \to l\nu$ and $Z/\gamma^* \to ll$ production cross sections in proton-proton collisions at $\sqrt{s} = 7$ TeV with the ATLAS detector*, JHEP **1012**, 060 (2010) [arXiv:1010.2130 [hep-ex]].

[124] `cern.ch/lhcoptics`.

[125] K. Golec-Biernat, C. Royon, L. Schoeffel and R. Staszewski, *Electroweak vector boson production at the LHC as a probe of mechanisms of diffraction*, Phys. Rev. D **84** (2011) 114006 [arXiv:1110.1825 [hep-ph]].

List of Figures

List of Tables